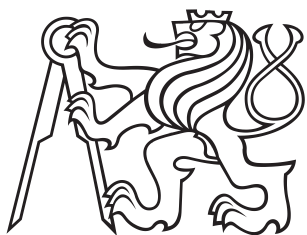


Dissertation



Czech
Technical
University
in Prague

F4

Faculty of Nuclear Sciences and Physical Engineering
Department of Physical Electronics

Generation of X-Rays by Laser Accelerated Electron Beam

Ing. Vojtěch Horný

Supervisor: Doc. Ing. Ondřej Klimo, Ph.D.

Supervisor–specialist: Ing. Jaroslav Nejd, Ph.D.

Field of study: Physical Engineering

Subfield: Physical Electronics

June 2018

| Bibliografický záznam | |
|------------------------------|--|
| Autor | Ing. Vojtěch Horný České vysoké učení technické v Praze Fakulta jaderná a fyzikálně inženýrská Katedra fyzikální elektroniky |
| Název práce | Generace rentgenového záření pomocí laserem urychleného elektronového svazku |
| Studijní program | Aplikace přírodních věd |
| Studijní obor | Fyzikální inženýrství |
| Školitel | Doc. Ing. Ondřej Klimo, Ph.D. České vysoké učení technické v Praze Fakulta jaderná a fyzikálně inženýrská Katedra fyzikální elektroniky |
| Školitel specialista | Ing. Jaroslav Nejd, Ph.D. Akademie věd České republiky Ústav fyziky plazmatu |
| Akademický rok | 2017/2018 |
| Počet stran | 149 |
| Klíčová slova | urychlování elektronů brázdovou vlnou, betatronové záření, rentgenové záření, laserové plazma |

| Bibliographic Entry | |
|----------------------------|---|
| Author | Ing. Vojtěch Horný Czech Technical University in Prague Faculty of Nuclear Sciences and Physical Engineering Department of Physical Electronics |
| Title of Dissertation | Generation of X-Rays by Electron Beam accelerated by Laser |
| Degree Programme | Application of Natural Sciences |
| Field of Study | Physical Engineering |
| Supervisor | Doc. Ing. Ondřej Klimo, Ph.D. Czech Technical University in Prague Faculty of Nuclear Sciences and Physical Engineering Department of Physical Electronics |
| Supervisor specialist | Ing. Jaroslav Nejd, Ph.D. Academy of Sciences of the Czech Republic Institute of Plasma Physics |
| Academic Year | 2017/2018 |
| Number of Pages | 149 |
| Keywords | laser wakefield acceleration, betatron radiation, x-rays, laser plasma |

Acknowledgements

This thesis and all of my doctoral studies could not be succeeded without the help and support of my advisor, colleagues, family, and fiancée. Taking this opportunity, I would like to acknowledge all of them.

Above all, I would like to express the sincerest appreciations and gratitude to my supervisor, Doc. Ing. Ondřej Klimo, Ph.D., for his watchful guidance, all the knowledge he shared with me, and all the skills he taught me during all these years since 2011. Moreover, I am grateful to his enthusiastic approach to the science which influenced me a lot. The consultations with him often sowed the seeds of future ideas in the topics I would not have anticipated in advance.

I would like to thank my supervisor specialist, Ing. Jaroslav Nejdle, Ph.D., for a plenty of enriching consultations, and for allowing me to participate in the experimental campaigns in the beginning of my study.

Special thanks belong to Ing. Miroslav Krůs, Ph.D. who directed me to the topic of electron injection into a wake-field accelerator and who supported my research from the position of the head of Laser department at the Institute of Plasma Physics, Czech Academy of Sciences, where I have been employed since 2014.

Many thanks also go to my colleagues Václav Petržílka, Michaela Kozlová, and Karel Boháček. I thank Prof. Jiří

Limpouch for introducing me the laser plasma research.

I would like to express my deep gratitude towards my parents and my brother for the encouragement that helped me in the completion of this work. Finally, I would like to thank my fiancée Karolina for her love, endless support, and all the joy she has brought to my life.

Access to computing and storage facilities owned by parties and projects contributing to the National Grid Infrastructure MetaCentrum provided under the programme *Projects of Large Research, Development, and Innovations Infrastructures* (CESNET LM2015042), and to ECLIPSE cluster owned by ELI Beamlines is greatly appreciated.

I acknowledge financial support from Czech Science Foundation (GA CR) project 15-03118S, Czech Technical University (CTU) project SGS16/248/OHK4/3T/14, and Ministry of Education, Youth and Sports of the Czech Republic project LM2015083.

Declaration

I declare that I wrote this dissertation independently with the use of cited bibliography. This dissertation is the result of my own work, except where explicit reference is made to the work of others, and has not been submitted for another qualification to this or any other university.

Prague, 12th June 2018

Abstract

X-ray radiation represents a powerful tool to investigate the properties of matter. Currently, promising concepts of the X-rays generation from laser plasmas are arising. These sources are mainly based on laser wakefield acceleration of electrons related with the interaction of ultrashort and ultraintense laser pulses with gaseous targets. The fundamental idea is to wiggle trajectories of relativistic electrons in the beam and to induce directional emission of high-frequency electromagnetic radiation thereby. Transverse oscillations either occur naturally during the acceleration process in case of betatron radiation, or they are forced by counter-propagating laser pulse in the case of Thomson backscattering.

The features of generated X-ray pulses are determined by the properties of accelerated electron bunches. The plasma electron injection into a nonlinear plasma wave accelerating phase is of a decisive influence. Therefore, two novel optical injection schemes are designed and analyzed. Both provide a high charge and short duration electron bunches, what is beneficial for generation of short and relatively intense X-ray pulses. The first scheme involves a low intensity perpendicular injection pulse while the second one uses a preceding injection pulse. The second scheme is inspired by a geometrical motive and induced wave breaking on a short vacuum plasma transition.

A new method to calculate the betatron

radiation features is developed too. It is based on the Liénard-Wiechert potentials and it takes advantage of the characteristic shape of the signal emitted during the electron betatron oscillations. It is shown that a significant part of electron trajectory, where the radiation emission is negligible can be omitted and not taken into account in the calculation. This decreases the computational memory demands substantially. Additionally, the method is also used for the construction of the emitted radiation spectrogram. This method suggests that the actual duration of betatron radiation pulses is rather shorter than it can be estimated from the electron bunch length. Moreover, it is demonstrated that X-ray pulses shorter than 3 fs can be generated applying one of proposed optical injection schemes.

This method represents useful tool to investigate or even to tailor the betatron X-ray pulse temporal profiles and it can be used to design sources for future applications such as probing of ultrafast fundamental physical processes such as chemical reactions, phase transitions, lattice vibrations, or spin dynamics.

Abstrakt

Rentgenové záření představuje mocný nástroj ke studiu vlastností hmoty. V současnosti se rozvíjejí slibné koncepty generace rentgenového záření z laserového plazmatu. Tyto zdroje jsou založeny na urychlování elektronů brázdovou vlnou vznikající za ultrakrátkým ultraintenzivním laserovým impulzem v plynném terči. Základní princip těchto zdrojů spočívá v zakřivení trajektorií elektronů v relativistickém elektronovém svazku, což vede k emisi úzkého paprsku elektromagnetického záření s vysokou frekvencí. K příčným oscilacím dochází buď přirozeně v průběhu procesu urychlování v případě betatronového záření, nebo jsou vynuceny protiběžným laserovým impulzem v případě zpětného Thomsonova rozptylu.

Vlastnosti generovaných impulzů rentgenového záření jsou určeny vlastnostmi urychlených elektronových svazků. Rozhodující vliv má injekce plazmových elektronů do urychlující fáze nelineární plazmové vlny. Z tohoto důvodu byla navržena a studována dvě nová schémata. Obě poskytují krátké elektronové svazky s vysokým nábojem, což je výhodné pro generaci krátkých a relativně intenzivních impulzů rentgenového záření. První schéma využívá kolmo se šířící injekční impuls o malé intenzitě zatímco druhé schéma využívá k injekci impuls předcházející. Druhé injekční schéma je inspirováno geometrickým motivem a vynuceným lámáním vln na krátkém rozhraní vakua a plazmatu.

Ke studiu vlastností betatronového záření generovaného elektronovými svazky byla vyvinuta nová výpočetní metoda. Je založena na Liénardových-Wiechertových potenciálech a využívá charakteristického tvaru signálu vyzářeného během betatronových oscilací elektronů. Je ukázáno, že významnou část trajektorie elektronů, kde je emise záření zanedbatelná, lze při výpočtu vynechat, aniž by to mělo vliv na výsledné spektrum. Toto razantně snižuje nároky na počítačovou paměť. Metoda je navíc použita i ke konstrukci spektrogramů vyzářeného záření. S použitím této metody je možné ukázat, že délka impulzů betatronového záření je kratší, než bylo odhadováno na základě délky elektronového svazku. Za použití jednoho z navržených schémat optické injekce je navíc možné generovat rentgenové impulzy kratší než 3 fs.

Tato metoda představuje užitečný nástroj pro studium a dokonce i tvarování časového průběhu rentgenových impulzů betatronového záření a může být použita pro návrh zdrojů pro budoucí aplikace, kterými jsou například snímkování velmi rychlých procesů jako chemické reakce, fázové přechody, vibrace mřížky nebo spinová dynamika.

Contents

| | | | |
|--|-----------|--|------------|
| 1 Introduction | 1 | 3.6 Ionization injection | 67 |
| 1.1 Dissertation objectives | 3 | 3.6.1 Experiment at PALS | 69 |
| 1.2 Dissertation layout | 4 | 3.7 State-of-the-art of laser wakefield accelerators | 72 |
| 1.3 Role of author | 4 | 4 X-Rays from Laser Plasmas | 75 |
| 2 Laser Wakefield Acceleration | 7 | 4.1 Radiation by a moving charge . . | 75 |
| 2.1 Ultrashort laser pulses | 8 | 4.2 Betatron radiation | 82 |
| 2.2 Ionization of atoms in intense field | 12 | 4.2.1 Method to calculate the radiation properties | 84 |
| 2.3 Interaction of single electron with intense laser field | 14 | 4.2.2 Test of the method | 85 |
| 2.4 Ponderomotive force | 17 | 4.2.3 Simplification of the method for the wiggler case | 87 |
| 2.5 Plasma waves | 18 | 4.2.4 Spectrogram: temporal evolution of radiation profile | 90 |
| 2.6 Bubble regime | 22 | 4.2.5 Betatron radiation pulse length | 90 |
| 2.7 Other physical effects connected to LWFA | 24 | 4.2.6 Discussion | 97 |
| 3 Electron injection into acceleration phase | 27 | 4.3 Thomson scattering | 97 |
| 3.1 1D Hamiltonian theory of electron trapping | 28 | 4.3.1 Nonlinear Thomson scattering | 98 |
| 3.2 Self-injection | 32 | 4.3.2 Thomson backscattering . . . | 101 |
| 3.3 Density down-ramp injection . . . | 39 | 4.4 Synchrotron radiation | 105 |
| 3.4 Optical injection | 40 | 4.5 Other radiation sources | 106 |
| 3.4.1 Ponderomotive injection | 40 | 4.5.1 K- α radiation | 106 |
| 3.4.2 Injection by counter-propagating pulse | 41 | 4.5.2 High order harmonics radiation | 107 |
| 3.4.3 Injection by orthogonally crossed pulse | 43 | 4.5.3 Free electron laser from laser plasmas | 108 |
| 3.4.4 Orthogonally crossed pulses with perpendicular polarizations . | 44 | 5 Conclusion | 111 |
| 3.5 Injection by collinear pulses . . . | 59 | Bibliography | 113 |
| 3.5.1 Optically induced ionization injection | 59 | List of author's publications | 131 |
| 3.5.2 Injection by collinear pulse with different focusing | 59 | Publications in impacted journals and author's contribution | 131 |
| 3.5.3 Collinear multi-pulse scheme | 60 | Publications in conference proceedings | 132 |
| 3.5.4 Optical injection by preceding pulse | 60 | | |



Chapter 1

Introduction

X-ray radiation is generally defined as the part of the electromagnetic spectrum with energies higher than 250 eV, or equivalently with the corresponding wavelength shorter than 5 nm. This broad region can be divided into two parts, soft X-rays with the energy up to few keV, and more energetic hard X-rays [Attwood, 2007]. In this thesis we will mostly operate on and above this very uncertain border.

X-rays since its discovery by Wilhelm Conrad Röntgen in 1895 have been used as a mighty tool to investigate the properties of matter. On that account, Röntgen was actually awarded the first Nobel prize in physics. X-rays are being extensively exploited in various applications, including the fundamental and applied scientific research, the medical and industrial applications, or the public security.

Nowadays, incoherent X-ray radiation for standard applications is typically delivered by radioactive sources, X-ray tubes, and devices based on classical electron accelerators such as synchrotron.

There are various ways how to generate X-rays from accelerated electron bunch [Attwood and Sakdinawat, 2017]. The simplest one is bending of the electron trajectory in the synchrotron to generate so called synchrotron radiation. Rather more sophisticated mechanism is to use the periodical magnetic structures to force the accelerated electrons to undergo the transverse oscillations during their straight propagation and to radiate the X-rays thereby. These devices are called undulators or wigglers; the main difference between them is in the amplitude of deviation from the straight line path of the electrons.

Recently, X-ray free electron lasers opened a new path in a generation of intense X-ray light. These huge devices comprise of standard linear electron accelerator and a long undulator where the electron are clumped into microbunches separated by one wavelength of the generated light. Thus, the radiation emitted by the bunched electrons is in phase and the radiated intensity is increased rapidly. For example, all three planned beamlines of the European XFEL in Hamburg [Tschentscher and Feidenhans'l, 2017]

yet compete in parameters like the stability and reproducibility of the accelerated bunches and their parameters as a relative energy spread and normalized emittance of accelerated bunches. Nevertheless, there is a great effort to overcome these issues within the community of laser plasma researchers.

This dissertation also partially contributes the topic of laser-plasma based accelerated electron sources. A great attention is paid to optimizing of the electron injection into the accelerating phase of an accelerator, because it presumably influences the quality of the electron bunch and also thereby the features of a secondary X-ray radiation. Two novel schemes of an optical injection by an additional laser pulse are designed and investigated.

In principle, there are two main feasible mechanisms how to generate hard X-rays from electrons accelerated in laser wakefields. The first one is a betatron radiation emitted during acceleration phase. The transverse *betatron* oscillations are inherent and inseparable companion of acceleration. The second one is based on Thomson scattering of high energy electrons on an intense laser pulse. In this dissertation, it was confirmed that, under certain circumstances, the duration of generated hard X-ray pulses can be as short as few femtoseconds, what actually surpasses X-ray sources based on conventional electron acceleration schemes.

1.1 Dissertation objectives

The main aim of this dissertation is to investigate the generation of hard X-rays based on electron laser wakefield acceleration with currently achievable experimental devices. Therefore, a principal attention will be paid to the optimizing of the fundamental accelerated electron bunch parameters. In particular, new concepts of electron injection into the accelerating phase of a nonlinear plasma wave by an additional weaker laser pulse will be elaborated in a great detail, as this injection is the key factor which determines the electron bunch and thereby X-ray pulse quality.

These new injection schemes are beneficial for X-rays emission, because they provide relatively high charge (hundreds of pC) electron bunches with relatively low energy spread (10 %) and a short bunch length. The physics of these processes will be analyzed theoretically and by employing extensive numerical simulations. It is intended to test these schemes experimentally by author's colleagues later this year.

The features of a betatron radiation emitted during the acceleration process will be studied by a novel method based on the Fourier transform of the electric field emitted by accelerated electrons. This method will even enable investigate the length and temporal profile of betatron radiation. Other sources of hard X-rays from laser plasmas, in

The author developed a novel method to calculate the betatron radiation spectrum and even its temporal profile based on the knowledge of the trajectory of the accelerated electrons². He implemented, tested, and demonstrated this method. Also, a standard method of a radiation calculation based on the Fourier transform of the radiated field was coded and used for the testing purposes and for calculations of Thomson scattering spectra. All graphically presented results of radiation features were calculated by the author.

The author also implemented additional minor computational codes, namely a single particle solver of the relativistic motion equations in the field of the laser pulse with given temporal and spatial profile or few scripts for the analysis and post-processing of experimental data.

■ Theoretical results

The author crucially contributed to the design, theoretical analysis, and formulation of both novel optical injection schemes³.

²Design and development of this method were consulted with Jaroslav Nejd and Ondřej Klimo.

³Other co-authors are Václav Petržílka, Miroslav Krús, and Ondřej Klimo.

Chapter 2

Laser Wakefield Acceleration

Laser wakefield acceleration (LWFA) is a method to accelerate electrons in laser plasma. The idea was originally proposed by Tajima and Dawson [Tajima and Dawson, 1979]. This concept may appear as counter-intuitive since the principle Lawson–Woodward theorem [Lawson et al., 1979, Mulser and Bauer, 2010] states that the net energy gain of a relativistic electron interacting with a continuous electromagnetic field is zero. The theorem assumes that

- the laser field is in vacuum with no walls or boundaries present,
- no static electric or magnetic fields are present,
- the region of interaction is infinite,
- ponderomotive effects (nonlinear forces) are neglected.

Nevertheless, more of these assumption can be easily violated. Mainly, the presence of boundaries implies the longitudinal polarization of the electromagnetic wave. Also, it is not intended to accelerate electrons by the laser beam itself, but rather by a plasma wake wave dragged by the laser beam propagating through the underdense plasma⁴.

⁴A laser beam with a wavelength λ_L can propagate in unmagnetized plasma if the plasma density is smaller than the critical electron plasma density n_c given by

$$n_c = \frac{4\pi^2 \varepsilon_0 m_e c^2}{e^2 \lambda_L^2},$$

where ε_0 is vacuum permittivity, m_e is electron mass, c is the speed of light in vacuum, and e is an electron charge. It can be expressed in practical units as

$$n_c [\text{cm}^{-3}] = \frac{1.1 \times 10^{21}}{\lambda_L [\mu\text{m}]^2}.$$

The critical density is such a density where frequency of electron oscillations in plasma ω_p is equal to the frequency of the laser, i.e.

$$\omega_p = \sqrt{\frac{n_e e^2}{m_e \varepsilon_0}} = \omega_L,$$

This structure can sustain large acceleration gradient of the order of hundreds GV/m for a sufficient time to accelerate electrons up to GeV energies in a several mm or cm thick plasma layer. The conventional radiofrequency accelerators generate acceleration gradient in the order of tens of MV/m; so the large facilities with the size of the order of tens of meters are needed to obtain the same results. On the other hand, the advantages of the conventional accelerator still surpass such drawback; they are more stable, tunable and generate the monoenergetic electron bunches.

Several mechanisms of the electron acceleration in laser plasmas appeared and the features of the produced bunches have been continuously improved. The state-of-the-art in 2009 is reviewed by Esarey [Esarey et al., 2009], more recent overview can be found in the book by Macchi [Macchi, 2013]. Recently, multi-GeV electrons have been generated using PW laser system [Wang et al., 2015, Leemans et al., 2014] by the LWFA mechanism. In this dissertation, the overview of published experimental or simulation achievements is provided in Section 3.7, particularly in Table 3.11.

Laser wakefield electron acceleration is in principle a very complex procedure. A number of fundamental physical processes must be introduced to satisfactorily describe it. The most important ones are an ionization of neutral atoms in the presence of intense laser field, an interaction of a single electron with a relativistic laser pulse, a propagation of such a pulse through the underdense plasma, ponderomotive force, and a generation of an electron plasma wave. All the aforementioned effects will be introduced in this first chapter. The issue of electron injection into a plasma wave acceleration phase will be discussed in the following special chapter because a significant amount of original research has been conducted on this topic.

2.1 Ultrashort laser pulses

Laser wakefield acceleration is practically realized by the interaction of ultrashort (tens of fs) intense laser ($I > 10^{18} \text{ W}\cdot\text{cm}^{-2}$) pulses with neutral gas streaming out of the supersonic nozzle or static gas cells. Such intense laser pulses are generated in Ti:sapphire crystal employing the technique of chirped-pulse amplification (CPA) [Maine et al., 1988, Mourou, 1997], or optical parametric chirped-pulse amplification (OPCPA) [Dubietis et al., 1992, Ross et al., 1997, Witte and Eikema, 2012]. Typically, ultrashort laser pulses can be approximated by Gaussian in temporal and spatial profiles. To our knowledge, the most accurate derivation of space-time profile of an ultrashort

where n_e is electron density. If a plasma density is higher than the critical density, a laser pulse is reflected from plasma.

pulsed Gaussian beam as a solution of paraxial scalar wave equation is provided in [Wang et al., 1997]. Within this work, we will present the description of Gaussian beam in simpler way though; our intention is only to introduce all the necessary quantities used in further sections of this dissertation. The electric field of laser pulse propagating in vacuum along x -axis can be written as

$$\mathbf{E}(r, x, t) = E_0 \frac{w_0}{w(x)} \exp \left[-\frac{r^2}{w^2(x)} \right] \exp \left[-2 \ln 2 \frac{(x - ct)^2}{c^2 \tau^2} \right] \times \Re \left\{ \exp \left[i\omega_L t - ik_L x - ik_L \frac{r^2}{2R(x)} + i\psi_G(x) \right] \right\} \mathbf{e}, \quad (2.1)$$

where E_0 is the electric field amplitude, w_0 is a waist size in the focal plane ($x = 0$), i.e. the radius at which the intensity drops to $1/e^2$ of its axial value at the focus position of the laser, $r^2 = y^2 + z^2$, τ is the full width half maximum (FWHM) of intensity (illumination) and it will be called pulse length within this work, $k_L = 2\pi/\lambda_L$ is the laser light wavenumber, ω_L is the laser light angular frequency, and \mathbf{e} is a vector of the laser polarization. Linear polarization in the y direction means that $\mathbf{e} = \mathbf{e}_y$; circular polarization would be $\mathbf{e} = (\mathbf{e}_y + i\mathbf{e}_z)/\sqrt{2}$.

Formula (2.1) includes three inner functions which depend only on the longitudinal coordinate x : beam waist radius $w(x)$, radius of wavefront curvature $R(x)$, and the Gouy phase $\psi_G(x)$. These functions are given as

$$w(x) = w_0 \sqrt{1 + \left(\frac{x}{x_R} \right)^2}, \quad (2.2)$$

$$R(x) = \begin{cases} x \left[1 + \left(\frac{x}{x_R} \right)^2 \right] & \text{if } x \neq 0, \\ +\infty & \text{if } x = 0, \end{cases} \quad (2.3)$$

$$\psi_G(x) = \arctan \frac{x}{x_R}, \quad (2.4)$$

where

$$x_R = \frac{\pi w_0^2}{\lambda_L} \quad (2.5)$$

is the Rayleigh length, i.e. the distance along the propagation direction of a beam from the focal plane to the place where the area of the cross section is doubled [Siegman, 1986]. Typical pulse used in this work has $w_0 \approx 9 \mu\text{m}$ and $\lambda_L = 0.8 \mu\text{m}$, its Rayleigh length is $318 \mu\text{m}$. Propagation distance through plasma is typically in the order of millimeters though, nonetheless, the diffraction is reduced thanks to the effect of self-focusing [Sun et al., 1987].

In practical cases when $w_0 \gg \lambda_L$ what is valid within this work, the associated magnetic field is everywhere directly proportional to the electric field and perpendicular to it. For

linear polarization of the electric field in the y -direction, magnetic field intensity \mathbf{H} is polarized in z -direction and it can be written

$$\mathbf{H}(r, x, t) = \mathbf{e}_z \frac{1}{\eta_0} E_y(r, x, t), \quad (2.6)$$

where $\eta_0 = 377 \Omega$ is the characteristic vacuum impedance. In a vacuum, magnetic field \mathbf{B} can be expressed as

$$\mathbf{B}(r, x, t) = \mu_0 \mathbf{H}(r, x, t), \quad (2.7)$$

where μ_0 is the vacuum permeability. Electric and magnetic field can be expressed in the form of the vector potential \mathbf{A} and the scalar potential Φ as

$$\mathbf{E} = -\nabla\Phi - \frac{\partial\mathbf{A}}{\partial t}, \quad (2.8)$$

$$\mathbf{B} = \nabla \times \mathbf{A}. \quad (2.9)$$

Assuming Coulomb gauge $\nabla \cdot \mathbf{A} = 0$, and the fact that in vacuum we have $\Phi = 0$, both fields can be covered only by the vector potential \mathbf{A} . The normalized vector potential

$$\mathbf{a} = \frac{e\mathbf{A}}{m_e c}. \quad (2.10)$$

will be also used within this work.

It is convenient to describe an energy flux through the focal plane. The intensity in the focus (for the case of the polarization in y -direction) is given by

$$I(r, x = 0, t) = I_{max} \exp\left(-\frac{2r^2}{w_0^2}\right) \exp\left(-4 \ln 2 \frac{t^2}{\tau^2}\right), \quad (2.11)$$

where

$$I_{max} = \frac{|E_0|^2}{2\eta_0}. \quad (2.12)$$

The factors oscillating with a high frequency are averaged over a their period. The total energy stored in the pulse is then

$$\begin{aligned} \mathcal{E} &= \int_{-\infty}^{+\infty} \int_{-\infty}^{+\infty} \int_{-\infty}^{+\infty} I(r, x = 0, t) dy dz dt \\ &= I_{max} \left[\int_{-\infty}^{+\infty} \exp\left(-\frac{2y^2}{w_0^2}\right) dy \right]^2 \int_{-\infty}^{+\infty} \exp\left(-4 \ln 2 \frac{t^2}{\tau^2}\right) dt \\ &= \frac{1}{4} \sqrt{\frac{\pi^3}{\ln 2}} I_{max} \tau w_0^2. \end{aligned} \quad (2.13)$$

Equation (2.13) provides a useful way to determine the maximum intensity in the focus from measurable quantities which are energy, pulse length, and spot size.

| \mathcal{E} [J] | τ [fs] | w_0 [μm] | I_{max} [10^{18} W $\cdot\text{cm}^{-2}$] | a_0 | citation |
|-------------------|-------------|-------------------------|---|-------|-------------------------|
| 1.0 | 30 | 7.8 | 34.2 | 4 | [Lehe et al., 2013] |
| 1.3 | 25 | 9.5 | 34.2 | 4 | [Horný et al., 2017b] |
| 1.8 | 45 | 22 | 4.94 | 1.5 | [Barber et al., 2017] |
| 2.1 | 30 | 20 | 12.46 | 2.6 | [Couperus et al., 2017] |

Table 2.1: Example parameters of laser pulses and its focusing used for LWFA with Ti:sapphire laser with $\lambda_L = 0.8 \mu\text{m}$.

The intensity of laser pulse may be expressed in the form of the normalized vector potential. Let us define the amplitude of this normalized vector potential \mathbf{a} as a laser strength parameter a_0 . In practical units, aa_0 is given as

$$a_0 = 0.855 \sqrt{I_{max} [10^{18} \text{ W/cm}^2]} \lambda_L [\mu\text{m}]. \quad (2.14)$$

for linearly polarized laser pulse. As an illustration, $a_0 = 1$ for $I_{max} = 2.1 \times 10^{18} \text{ W/cm}^2$ for standard Ti:sapphire laser light with $\lambda_L = 0.8 \mu\text{m}$. Practically, the intensity and laser strength parameter can be expressed from measurable quantities from equations (2.13) and (2.14) as

$$I_{max} = 0.598 \frac{\mathcal{E}}{\tau w_0^2}, \quad (2.15)$$

$$a_0 = 209 \sqrt{\frac{\mathcal{E} [\text{J}]}{\tau [\text{fs}] w_0}}, \quad (2.16)$$

when Gaussian pulse in both spatial and temporal domain is assumed. List of several considered laser parameters used for LWFA experiments taken from literature is shown in Table 2.1.

Another quantity often used within the LWFA community is a laser power. It is important to determine it when discussing the feasibility of particular experimental design at particular laser system. Laser power is defined as

$$P = \frac{1}{2} \pi w_0^2 I_{max}. \quad (2.17)$$

Typically, few tens/hundred TW laser systems are used for LWFA experiments where the electrons are accelerated up to energies of hundreds of MeV [Esarey et al., 2009]. However, as a part of this work, the simulation supporting the experimental campaign with laser system as weak at 7 TW was performed [Boháček et al., 2018].

2.2 Ionization of atoms in intense field

Ionization of the target is a basic requirement for the plasma formation. The degree of ionization α can be defined as

$$\alpha = \frac{n_e}{n_i + n_0}, \quad (2.18)$$

where n_e , n_i , and n_0 are densities of electrons, ions, and neutrals, respectively. The threshold intensity of plasma production is around 10^{10} W/cm² [Raizer, 1977]. If the laser intensity overcomes the atomic intensity [Gibbon, 2004]

$$I_a \simeq 3.51 \times 10^{16} \text{ W/cm}^2, \quad (2.19)$$

ionization of any target material is guaranteed. Nevertheless, a considerable ionization occurs also with much lower intensities, it is caused by multiphoton or tunnel effects. Such processes typically take place even before the main pulse arrival. Generation of various pre-pulses is unfortunately inseparable part of femtosecond pulses generation technology. Moreover, ultrashort high-intensity laser pulses also contain long pre-pedestals which induce pre-ionization. Typical high intensity laser pulse contrast is 10^{-5} , and the pedestal length is several ps [Umstadter, 2003].

The electron can be expelled from the atom when it receives sufficient energy to be released out of the bound state to free continuum. It can be done as a photoelectric effect, it means by absorbing a photon which carries larger energy than ionization energy. However, pure photoelectric effect is not relevant here because the energy of absorbed photon has to be greater than the ionization energy of an electron E_{ion} . As an example, the ionization energy of hydrogen atom is 13.6 eV, photons of laser pulses from Ti:sapphire crystal have energy 1.6 eV.

For high energy flux (i.e. large photon density), single electron may even absorb several photons in order to abandon the bounded state. If it absorbs exact number of photons necessary for the ionization, the effect is called multiphoton ionization. Hydrogen atom has to absorb nine photons to be ionized. If the number of absorbed photons is even higher, their energy is carried away as a kinetic energy of released electron E_{kin} , the effect is called above threshold ionization. The extended formula formula of photoelectric effect covering both these cases reads

$$E_{kin} = (n + s)\hbar\omega_L - E_{ion}, \quad (2.20)$$

where n is number of photons necessary for multiphoton ionization and s is number of photons absorbed redundantly. The above threshold ionization occurs when $s \geq 1$. Both these ionization processes are shown in Figure 2.1.

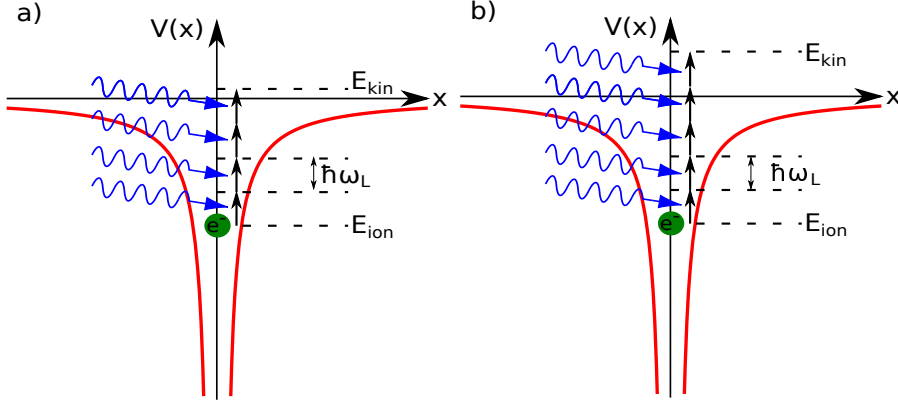


Figure 2.1: a) Standard multiphoton ionization. A bounded electron absorbs exact number of photons necessary for its release. b) Above threshold ionization. A bound electron absorbs even more electrons, redundant energy is transferred into its final kinetic energy.

When the intensity of the laser pulse increases up to the orders of 10^{14-15} W/cm², the atomic binding potential is disturbed by the laser field. In a simple classical picture of this effects [Bethe and Salpeter, 2012, Gibbon, 2004], the Coulomb potential is modified by stationary electric field

$$V(x) = -\frac{Ze^2}{x} - eEx. \quad (2.21)$$

Such approach is legitimate, because the time scale of multiphoton absorption and atomic processes are much shorter than the laser pulse length. Thus, as the Coulomb barrier in a certain direction is thereby suppressed, the probability of the tunneling through the barrier significantly increases.

If the barrier falls below E_{ion} , the electron is not bounded anymore and can freely escape from the atom. Such an effect is called barrier suppression ionization. For hydrogen atom, effective appearance intensity is [Gibbon, 2004]

$$I_{app} = \frac{I_a}{256} \simeq 1.4 \times 10^{14} \text{ W/cm}^2. \quad (2.22)$$

This value defines the border where the ionization energy is equal to the depth of the potential barrier. Tunneling and barrier suppression ionization are illustrated in Figure 2.2.

Keldysh parameter γ_K describes conditions in which multiphoton or tunneling ionizations dominates [Keldysh et al., 1965]. It is given as

$$\gamma_K = \sqrt{\frac{\varepsilon_0 m_e c E_{ion} \omega_L^2}{e^2 I_L}}, \quad (2.23)$$

where I_L is laser intensity. In general, the multiphoton ionization dominates for $\gamma_K > 1$, whereas tunneling appears for strong fields or long wavelengths, i.e. $\gamma_K < 1$.

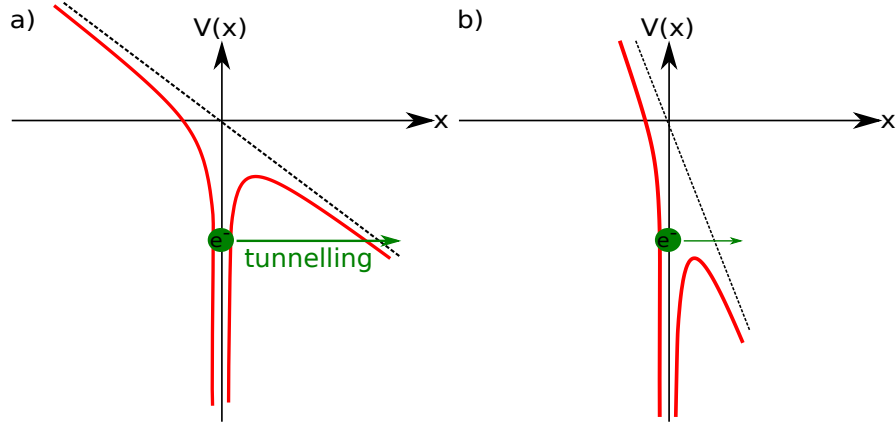


Figure 2.2: a) Tunneling ionization. Intense laser field modifies the shape of the potential barrier and thus increases the probability to tunnel through it. b) Barrier suppression ionization. The intense laser decreases the potential barrier height as much as the electron is not bounded anymore.

2.3 Interaction of single electron with intense laser field

As it was pointed out in the previous section, a significant ionization of the target occurs even before main pulse peak arrival. Thus, a high-intensity part of the laser pulse then interacts with electrons in the plasma. Firstly, let us describe the interaction of intense laser pulse with a single electron, i.e. without presence of plasma. The derived conclusions then help to understand the interaction of a laser pulse with plasmas, mainly the generation of electron plasma waves.

The relativistic motion equation of electron in the electric and magnetic fields \mathbf{E} and \mathbf{B} (Lorentz equation) reads

$$\frac{d\mathbf{p}}{dt} = -e(\mathbf{E} + \mathbf{v} \times \mathbf{B}), \quad (2.24)$$

where \mathbf{p} and \mathbf{v} are electron momentum and velocity vectors, respectively. These are interconnected via relativistic relation

$$\mathbf{p} = \gamma(\mathbf{v})m_e\mathbf{v}, \quad (2.25)$$

where $\gamma(\mathbf{v}) = 1/\sqrt{1 - \mathbf{v}^2/c^2} = \gamma(\mathbf{p}) = \sqrt{1 + \mathbf{p}^2/m_e^2c^2}$ is a relativistic Lorentz factor.

Firstly, let us assume that the laser light is an electromagnetic plane wave linearly polarized along y -axis which propagates in the x -direction. Neglecting the phase term, its electric field can be written as

$$\mathbf{E}(x, t) = E_0 \cos(k_L x - \omega_L t) \mathbf{e}_y. \quad (2.26)$$

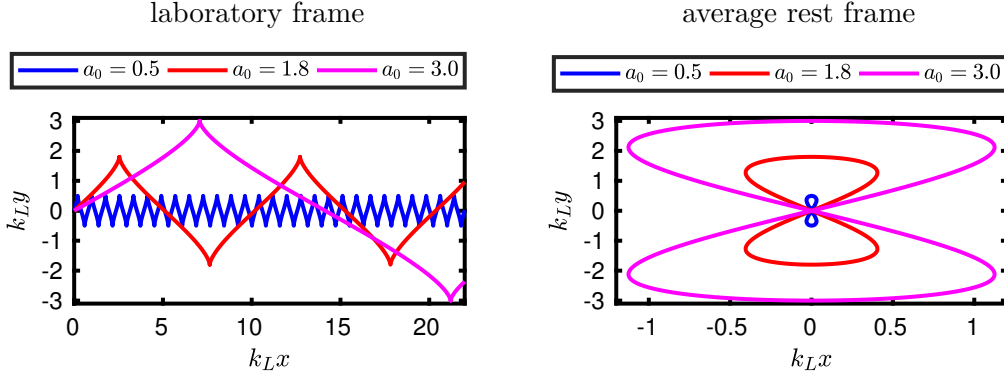


Figure 2.3: Electron orbits in linearly polarized electromagnetic plane wave with $\lambda_L = 0.8 \mu\text{m}$. Orbits in both frames correspond to each other.

Formula (2.26) can be rewritten as a relation for the vector potential. Integrating this equation, we obtain

$$\mathbf{A}(x, t) = A_0 \sin(k_L x - \omega_L t) \mathbf{e}_y, \quad (2.27)$$

where $A_0 = E_0/\omega_L$. The trajectory and momentum of electron obtained from equation (2.24) is demonstrated in [Gibbon, 2004] even for arbitrary laser pulse polarization. Let us illustrate an example solution with the electron which is at rest before electromagnetic wave arrives; it means that at $t = 0$, $p_{x,y} = 0$, $x = 0$, and $y = 0$. For the selected polarization, electron motion can be written as

$$\begin{aligned} p_x &= m_e c \frac{a_0^2}{2} \sin^2(k_L \xi) \\ p_y &= m_e c a_0 \sin(k_L \xi) \\ x &= \frac{a_0^2}{8k_L} [2k_L \xi - \sin(2k_L \xi)] \\ y &= -\frac{a_0}{k_L} \cos(k_L \xi), \end{aligned} \quad (2.28)$$

where $\xi = x - ct$ is a coordinate co-moving with the laser pulse. It can be seen even from equation (2.24) that electron remains in xy -plane for selected polarizations and initial conditions.

Electron orbits for three different laser light intensities are depicted in Figure 2.3. It is worth noting that for low intensities, the solution to equation (2.24) is an electron motion described by an oscillation at the laser frequency along a straight line parallel to the polarization vector. A higher laser intensity leads to an average drift in the direction of laser propagation. The threshold between two regimes is $a_0 = 1$, since the longitudinal drift motion is proportional to a_0^2 , whereas transverse motion scales as a_0 [Umstadter, 2003].

Electron drifts in laboratory frame in a presence of the plane electromagnetic wave. The electron orbit in its average rest frame can be derived from equations (2.28) by

neglecting first drift term in the formula for x -coordinate. Eliminating the argument $k_L \xi$, the implicit formula for the famous figure-eight motion can be obtained. It is

$$16\xi^2 = y^2(a_0^2 - k_L^2 y^2). \quad (2.29)$$

Corresponding trajectories in average rest frame are also shown in Figure 2.3.

A finite time length of the laser pulse can be included in the integration of Lorentz equation (2.24) too. In a first adiabatic approximation, temporal envelope function $f(t)$ is introduced in formula for normalized vector potential of the laser pulse (2.27). Function $f(t)$ is only slowly varying on the time scale of the laser pulse period, i.e. $df/dt \ll \omega_L f$. Vector potential of the laser pulse can be in this case written as

$$\mathbf{A}(x, t) = A_0 f(t) \sin(k_L x - \omega_L t) \mathbf{e}_y. \quad (2.30)$$

The solution of the motion equation (2.24) is then similar to the case of the plane wave, only the term a_0 is replaced by term $a_0 f(t)$ in equations (2.28). Thus, the electron does not gain energy from the finite plane wave, as it can be seen from formulas of momenta in (2.28).

As it was already stated in Section 2.1, real pulses are often and sufficiently approximated by Gaussian functions in both space and time domains; the electric and magnetic field of such a pulse is described by equations (2.1) and (2.7). Unfortunately, the electron motion equation (2.24) cannot be analytically integrated in this case due to the fact that the Lorentz factor depends on both p_x and p_y . A numerical integration is still possible though. Figure 2.4 visualizes the solution relativistic motion equations of single electrons in the vacuum in presence of intense laser pulse with parameters typical for current LWFA experiments.

Contrary to the case with transversally uniform \mathbf{E} and \mathbf{B} fields of the plane wave, spatial shape of the pulse significantly affects the solution of Lorentz equation (2.24). Focusing on a small waist generates large radial intensity gradients which actually accelerate the electrons in the sense that they carry a non-zero momentum even after the laser pulse passed. The force responsible for such behavior is called a ponderomotive force and will be briefly discussed in Section 2.4. Its action can be already seen in Figure 2.4. The electrons initially located off-axis are steadily ejected out of high-intensity region. Energy and angular distributions of these electron groups are shown in the bottom panel of Figure 2.4.

It is worth noting, and it can be also seen in Figure 2.4, that electron initially located on axis remains on axis, and is carried away by the laser pulse. It can gain energy up to several MeV. This process is called direct laser acceleration [Gahn et al., 1999].

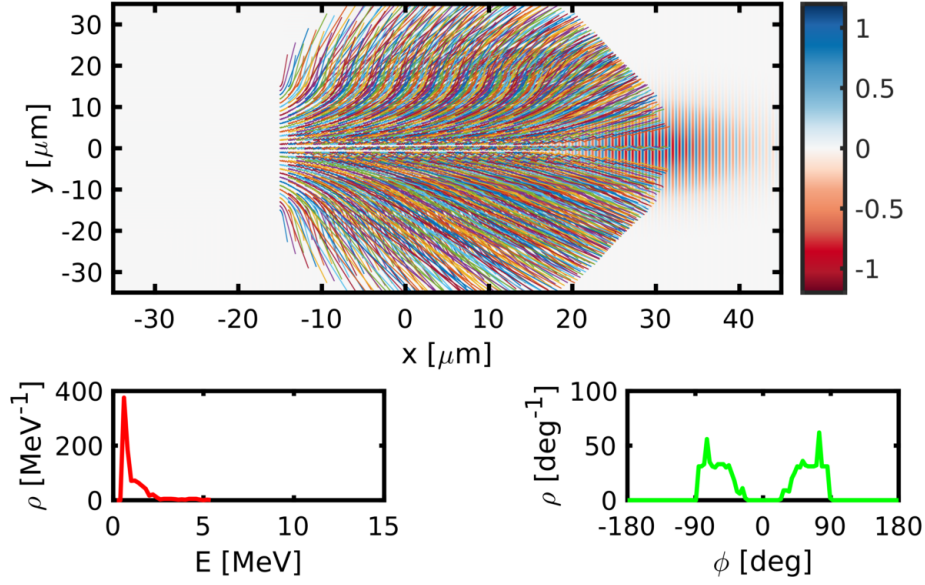


Figure 2.4: A set of solutions of the relativistic motion equation of single electrons in vacuum in the presence of laser pulse. The test particles are initially at rest and located on a grid in a square 30×30 microns. Red and blue colors represent the magnetic field in the z -direction normalized to the maximum magnetic field of the drive pulse. Snapshot at the time of $t = 97$ fs after the drive pulse crossed its focal point at $x = 0$ is displayed. Pulse parameters are: $\lambda_L = 0.8 \mu\text{m}$, $w_0 = 9.5 \mu\text{m}$, $\tau = 25$ fs, $a_0 = 4$. The graphs in the bottom frame represent energy and angular distribution of chosen sample of 961 electrons.

2.4 Ponderomotive force

The ponderomotive force is a non-linear force that all the charged particles experience in an non-uniform oscillating electric field, e.g. in the presence of the short intense laser pulse. It is rigorously derived in [Kruer, 1988], heuristic explanation arguments are given in [Gibbon, 2004]. Ponderomotive force can be expressed as

$$\mathbf{F}_p = -\frac{q^2}{4m\omega_L^2} \nabla(\mathbf{E}^2), \quad (2.31)$$

where q is the electrical charge of the particle, m is its mass, ω_L is the angular frequency of the field oscillations, and \mathbf{E} is the amplitude of the electric field. This force is associated with the laser pulse intensity gradients; it can be understood as a radiation pressure of laser intensity. It expels both ions and electrons out of high-intensity region. Due to the high inertia of the heavy ions, they are not significantly influenced by ponderomotive force during a very short interaction time, whereas the light electrons are dragged away.

The relation between the energy, which the electrons gain, and the direction in which

they are expelled, was derived in [Hartemann et al., 1995] and can be written as

$$\theta = \arctan \frac{\sqrt{2(\frac{\gamma}{\gamma_0} - 1)/(1 + \beta_0)}}{\gamma - \gamma_0(1 - \beta_0)}, \quad (2.32)$$

where $\beta_0 = v_0/c$ is initial normalized velocity of an electron and γ and $\gamma_0 = 1/\sqrt{1 - \beta_0^2}$ are electron final and initial Lorentz factors, respectively.

The fact that the electrons are expelled from a high-intensity region implies that a charge density perturbation is present in plasma. This perturbation induces the plasma oscillations; its characteristic frequency, the plasma frequency, is written as

$$\omega_p = \sqrt{\frac{n_e e^2}{m_e \epsilon_0}}, \quad (2.33)$$

where n_e is an electron plasma density, e is an electron charge, m_e is an electron mass, and ϵ_0 is a vacuum permittivity. Such plasma oscillations can be understood as a plasma wave or wakefield because they are traveling behind the laser pulse. Consequently, as the laser pulse propagates deeper in the plasma, the plasma wave is dragged in the wake of the laser pulse similarly as a wake wave behind the ship on the water surface. The phase velocity of the plasma wave is approximately equal to the laser pulse group velocity.

2.5 Plasma waves

In linear ($a_0 \ll 1$) 3D regime, the generation of the wake wave can be investigated by linearizing cold fluid equations [Esarey et al., 2009], and the solution is presented in [Ju, 2013]. The density perturbation and also longitudinal and transverse electric fields induced in plasma driven by Gaussian laser beam form periodical structure in the electron density which can be described by simple sine and cosine functions in coordinate co-moving with the drive pulse. Nevertheless, since the current trend in LWFA prefers non-linear plasma waves, the aforementioned linear theory will not be presented in this work.

Unfortunately, 3D model of nonlinear plasma wave ($a_0 \gtrsim 1$) has not been derived yet; therefore let us present the 1D theory in order to introduce the nonlinear plasma wave basic properties. Nonlinear 1D wake wave can be derived under the assumptions of zero electron temperature and ions at rest [Grassi et al., 2014, Bulanov et al., 2016]. Additionally, the laser is regarded as fixed on the fluid motion timescale; so we determine the wakefield quantities independently of the laser evolution. Then, the following set of

equations describes the wake:

$$\frac{\partial n_e}{\partial t} + \frac{\partial}{\partial x}(n_e v) = 0, \quad (2.34)$$

$$\frac{\partial p}{\partial t} + v \frac{\partial p}{\partial x} = -eE - \frac{m_e c^2}{2\gamma} \frac{\partial |\mathbf{a}|^2}{\partial x}, \quad (2.35)$$

$$\frac{\partial E}{\partial x} = \frac{m_e \omega_p^2}{e} \left(1 - \frac{n_e}{n_0}\right) \quad (2.36)$$

Here n_e is an electron density, n_0 is an ion density, v is x -component of electron velocity, $p = m_e \gamma v$ is x -component of electron momentum, E is a wake wave longitudinal field, and $\mathbf{a}(x, t)$ is normalized vector potential of transverse electromagnetic field of the pulse. In this 1D geometry, the transverse component of generalized electron momentum is a constant of motion, i.e. $\mathbf{p}_\perp / m_e c - \mathbf{a} = \text{const}$. Using the generalized transverse momentum conservation, Lorentz factor of an electron can be written as

$$\gamma = \sqrt{1 + |\mathbf{a}|^2 + \frac{p^2}{m_e^2 c^2}}. \quad (2.37)$$

Electrostatic field can be described as derivative of electrostatic potential

$$E = -\frac{\partial \Phi}{\partial x}. \quad (2.38)$$

Let us assume that the plasma wave is propagating with a constant phase velocity

$$v_p = c \sqrt{1 - \omega_p^2 / \omega_L^2}, \quad (2.39)$$

and that it is non-evolving, i.e. that it is a function only of the co-propagating coordinate

$$\xi = x - v_p t, \quad (2.40)$$

similarly as in [Esarey et al., 2009]. Continuity equation (2.34) can be then rewritten as

$$-v_p n_e' + (n_e v)' = 0, \quad (2.41)$$

where we used transformation according to equation (2.40) meaning that $\partial / \partial x = \partial / \partial \xi$, $\partial / \partial t = -v_p \partial / \partial \xi$ and the prime means differentiation with respect to ξ . It means that

$$n_e (v - v_p) = \text{const}$$

and this constant can be determined by requiring $n(\xi = +\infty, v = 0) = n_0$. Thus, the electron density can be expressed as a function of fluid velocity

$$\frac{n_e}{n_0} = \frac{v_p}{v_p - v}. \quad (2.42)$$

Similarly, let us rewrite motion equation (2.35):

$$-v_p p' - e\Phi' + m_e c^2 \gamma' = 0, \quad (2.43)$$

where we used relation resulting from formula (2.37)

$$\frac{\partial |\mathbf{a}|^2}{\partial \xi} = 2\gamma\gamma' - \frac{2pp'}{m_e^2 c^2}. \quad (2.44)$$

Thus, using also formula (2.38), another conservation relation was derived

$$-v_p \gamma m_e v - e\Phi + \gamma m_e c^2 - m_e c^2 = 0,$$

because $\Phi = v = 0$ and $\gamma = 1$ without presence of plasma. This integral of motion can be also seen as a consequence of Noether's theorem. It can be further rewritten in a convenient form introducing a normalized electrostatic potential

$$\phi = \frac{e\Phi}{m_e c^2}$$

and $\beta_p = v_p/c$, $\beta = v/c$ as

$$1 + \phi = \gamma(1 - \beta_p \beta). \quad (2.45)$$

Another useful relation can be obtained directly from expression of Lorentz factor (2.37)

and $p = \gamma m_e v$:

$$\gamma = \sqrt{\frac{1 + |a|^2}{1 - \beta^2}}. \quad (2.46)$$

The closed set of partial differential equations (2.34) – (2.36) can be expressed by a single ordinary differential equation (Poisson's equation)

$$\frac{d^2 \Phi}{d\xi^2} = \frac{m_e \omega_p^2}{e} \left(\frac{n_e}{n_0} - 1 \right) \quad (2.47)$$

and three simple algebraic expressions (2.42), (2.45), and (2.46). Using aforementioned formulas, let us derive the differential equation describing wakefield in a quasistatic approximation. In this case, all the fluid quantities can be expressed in terms of the pulse envelope a . Since such a derivation of a usable differential equation is not trivial, let us present the major steps in following paragraphs [Gibbon, 2004].

Square of the relation (2.45) can be written as⁵

$$\begin{aligned} (1 + \phi)^2 &= \gamma^2(1 - \beta_p \beta)^2 = \gamma^2(1 - 2\beta_p \beta + \beta_p^2 \beta^2 + 1 - 1) \\ &= \gamma^2[2(1 - \beta_p \beta) + \beta_p^2 \beta^2 - 1] = \gamma^2 \left[2\frac{1 + \phi}{\gamma} + \beta_p^2 - \frac{\beta_p^2(1 + a^2)}{\gamma^2} - 1 \right] \\ &= 2\gamma(1 + \phi) - \frac{\gamma^2}{\gamma_p^2} - \beta_p^2(1 + a^2). \end{aligned} \quad (2.48)$$

⁵Following expressions have been used during the derivation: $1 - \beta_p^2 = 1/\gamma_p^2$, $1 - \beta_p \beta = (1 + \phi)/\gamma$, $\beta^2 = 1 - (1 + a^2)/\gamma^2$, $1/\beta_p - \beta_p = 1/\gamma_p^2 \beta_p$.

After dividing by the factor of $\gamma_p^2(1+\phi)^2$, adding β_p^2 to both sides and further minor algebra, we can write

$$1 - \frac{2\gamma}{\gamma_p^2(1+\phi)} + \frac{\gamma^2}{\gamma_p^4(1+\phi)^2} = \beta_p^2 \left[1 - \frac{1+a^2}{\gamma_p^2(1+\phi)^2} \right], \quad (2.49)$$

$$\left[1 - \frac{\gamma}{\gamma_p^2(1+\phi)} \right]^2 = \beta_p^2 \left[1 - \frac{1+a^2}{\gamma_p^2(1+\phi)^2} \right], \quad (2.50)$$

and thus also eliminate γ as

$$\gamma = \gamma_p^2(1+\phi) \left[1 - \beta_p \underbrace{\sqrt{1 - \frac{1+a^2}{\gamma_p^2(1+\phi)^2}}}_\chi \right]. \quad (2.51)$$

From equations (2.45) and (2.51), β can be expressed in terms of a and ϕ (or χ) as

$$\beta = \frac{1}{\beta_p} \left(1 - \frac{1+\phi}{\gamma} \right) = \frac{1}{\beta_p} \left[1 - \frac{1}{\gamma_p^2(1-\beta_p\chi)} \right] = \frac{\beta_p - \chi}{1 - \beta_p\chi}. \quad (2.52)$$

Then, inserting this result into the equation (2.42) for electron density, we obtain

$$\frac{n_e}{n_0} = \frac{1 - \beta_p\chi}{\chi(1/\beta_p - \beta_p)} = \beta_p\gamma_p^2 \left(\frac{1}{\chi} - \beta_p \right), \quad (2.53)$$

and this can be already used in Poisson's equation (2.47). Hence,

$$\frac{d^2\phi}{d\xi^2} = \frac{\omega_p^2}{c^2} \gamma_p^2 \left(\frac{\beta_p}{\chi} - 1 \right),$$

and the final Poisson's equation describing the wakefield in a quasistatic approximation can be written as (cf. also [Esarey and Pilloff, 1995, Dodd et al., 2004, Bulanov et al., 2016, Faure, 2016])

$$\frac{1}{k_p^2} \frac{d^2\phi}{d\xi^2} = \gamma_p^2 \left\{ \beta_p \left[1 - \frac{1+a^2(\xi)}{\gamma_p^2(1+\phi(\xi))^2} \right]^{-1/2} - 1 \right\}, \quad (2.54)$$

where $k_p = \omega_p/c$. This equation is a non-linear differential equation of the second order and cannot be analytically integrated for given profile $a(\xi)$. Bulanov [Bulanov et al., 1989, Bulanov et al., 2016] integrated simplified equation

$$\frac{1}{k_p^2} \frac{d^2\phi}{d\xi^2} = \frac{1+a^2(\xi)}{2[1+\phi(\xi)]^2} - \frac{1}{2} \quad (2.55)$$

which corresponds to limit $\beta_p \rightarrow 1$ (low-density plasma) for $a(\xi) = \text{const}$ and obtained solution in the implicit form with the use of elliptic integral of the second kind. However, it is useful to integrate equation (2.54) numerically. Once obtaining the potential $\phi = \phi(\xi)$,

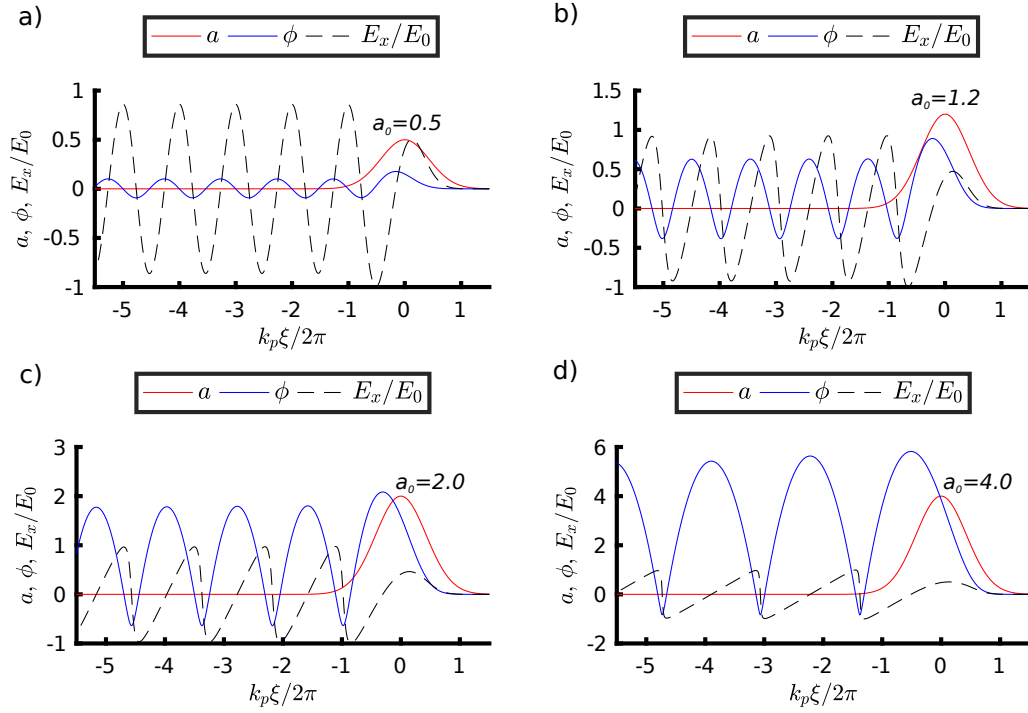


Figure 2.5: Electrostatic potential obtained by integration of equation (2.54) for various laser strength parameters ($\tau = 25$ fs, $n_e = 5 \times 10^{18}$ cm $^{-3}$).

the density, fluid velocity, and electric field can be calculated using equations (2.53), (2.52), and (2.38). Several solutions for ultrashort plasma wave drive pulses are shown in Figure 2.5.

The solution in the panel a) is a typical example of a linear wakefield. The longitudinal electric field has a sinusoidal shape which can be described also analytically in 3D geometry [Gorbunov and Kirsanov, 1987, Sprangle et al., 1988, Esarey et al., 1989]. Wakefield in the panel b) is moderately non-linear, and the ones in panels c,d) are fully non-linear. The shape of their longitudinal electric field is saw-like, therefore it can be approximated by linear function for every period of this plasma wave. Most of the result given in this work will be presented for laser and plasma parameters similar to the ones in panel d).

2.6 Bubble regime

The bubble regime [Pukhov and Meyer-ter Vehn, 2002] (also called cavitated wakefield regime, blow-out regime) is currently considered as the most effective mechanism to accelerate electrons in a plasma wave. The nonlinear plasma wave comprises a *spherical* ion cavity (bubble), which is the first period of the wakefield driven by the laser pulse. Ion cavity contains only ions as the light electron were expelled by ponderomotive force.

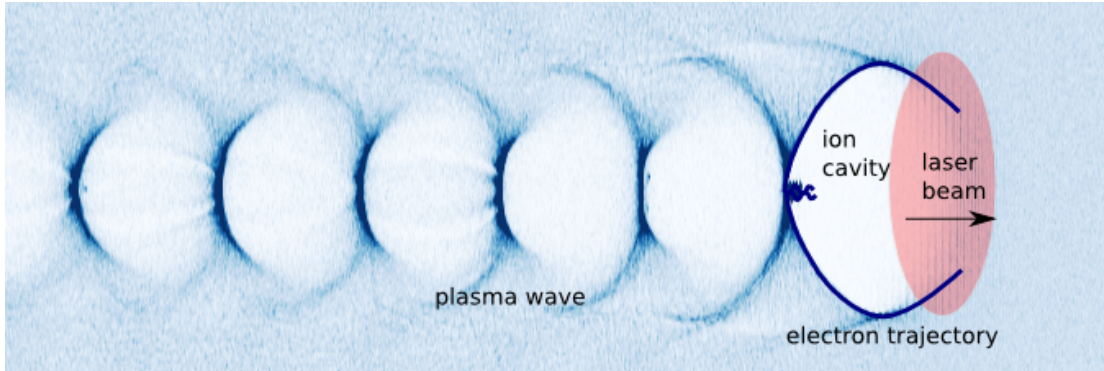


Figure 2.6: Scheme of the bubble regime of the laser wakefield acceleration. Background is obtained from 3D PIC simulation ($a_0 = 4$, $n_e = 5 \times 10^{18} \text{ cm}^{-3}$, $w_0 = 9.5 \text{ }\mu\text{m}$) and represents the electron density. The blue lines shows the trajectories of self-injected electrons.

Following periods of plasma wave carry lower longitudinal electric field, thus the electrons trapped there are accelerated less efficiently, i.e. to lower energies. Schematic drawing of the bubble regime is shown in Figure 2.6.

Bubble regime with the spherical bubble is achieved when the following three conditions are fulfilled:

1. the waist size w_0 of the incident laser pulse is coupled with the plasma density

$$\frac{\omega_p}{c} w_0 = 2\sqrt{a_0} \quad (2.56)$$

2. the pulse length τ is approximately the half of the plasma wavelength λ_p

$$c\tau \approx \frac{\lambda_p}{2} = \frac{\pi c}{\omega_p} \quad (2.57)$$

3. the laser intensity is sufficiently high

$$a_0 > 2. \quad (2.58)$$

A strong gradient of the electric field in the longitudinal direction with respect to the laser propagation direction is formed in this ion cavity. Electrons may be trapped in the rear part of the bubble by various injection processes and then accelerated significantly. During the acceleration process, the trapped electrons advance to the middle of the ion cavity, since they propagate almost with the speed of light, whereas the ion cavity propagates slower, with the phase velocity given by (2.39).

Once the electrons reach the middle of the bubble, they experience inverse polarity of the electric field; therefore they are decelerated. The energy gain is proportional to the

time spent in the rear part of the ion cavity. The distance traveled in the accelerating field is called the dephasing length.

The plasma frequency is proportional to the square root of the plasma density. It can be seen from the equation (2.39), that the ion cavity velocity drops with the increase of the electron density. It means that the electrons might be accelerated to the higher energies in the less dense plasma. On the other hand, in the high-density plasma, the self-focusing effect sustains the high intensity of the laser pulse which drags the plasma wave. The plasma density has to be chosen with respect to the laser parameters understanding both dephasing and self-focusing to efficiently accelerate the electrons in the bubble regime of the laser wakefield acceleration.

2.7 Other physical effects connected to LWFA

Self-focusing. A laser pulse undergoes diffraction in vacuum; its waist grows according to equation (2.2). This can be suppressed using some form of optical guiding. Moreover, the plasma itself reduces the diffraction of a laser beam with $a_0 > 1$. This effect is known as self-focusing and it may help to preserve the reasonably small laser beam spot size on a distance much higher than several Rayleigh lengths.

The threshold value for the relativistic self-focusing is relativistic critical power [Mourou et al., 2006]

$$P_{cr} = \frac{m_e^2 c^5 \omega_L^2}{e^2 \omega_p^2} \approx 17 \left(\frac{\omega}{\omega_p} \right)^2 \text{ GW.} \quad (2.59)$$

The ion cavity would fall apart if the self-focusing would not be present due to the diffraction of the laser light during its propagation in the plasma.

Electron dephasing. Highly relativistic electron outruns the plasma wave which limits the possible energy gain of an electron. Dephasing length or also effective acceleration length [Esarey et al., 2009] is defined as the length which the electron must travel before its phase slips by one-half of the period with respect to the plasma wave. In the nonlinear 3D bubble regime, it is given as [Esarey et al., 1996, Geddes et al., 2005, Lu et al., 2007]

$$L_d \simeq \frac{4}{3} \frac{\omega_L^2}{\omega_p^2} \frac{\sqrt{a_0}}{k_p}. \quad (2.60)$$

Non-linear dephasing length depends on both electron density and laser intensity.

Pump depletion. As the laser driver excites a plasma wave, it loses energy, i.e., it depletes. The depletion length is a distance before the laser pulse loses half of its energy.

In the nonlinear 3D bubble regime, it was estimated as [Lu et al., 2007]

$$L_{pd} \simeq \frac{\omega_L^2}{\omega_p^2} c\tau. \quad (2.61)$$

Chapter 3

Electron injection into acceleration phase

In the previous chapter, the processes leading to the generation of the plasma waves were described. These plasma waves are dragged by the drive pulse and propagate through the underdense plasma with phase velocity which is very close to the speed of light in vacuum. They carry very strong longitudinal electric field typically in the order of hundreds of GV/m.

Once an electron is located in this plasma wave, and its longitudinal velocity is already higher than the phase velocity of the plasma wave itself, it is carried away by this plasma wave. Such situation is also synonymously called electron trapping in injection into the wake wave. Moreover, if it is located in the accelerating phase of this plasma wave (the region where the sign of a longitudinal electric field is negative, assuming the plasma wave traveling in the increasing coordinate direction), the electron gains energy from this plasma wave similarly as a wake-surfer gains the energy from the wake wave driven by the high-speed boat at the water surface.

The remarkable difference between energy the surfer and the electron can gain from their respective driving wake waves is related to the special theory of relativity. The energy of a classical surfer scales with the square of his velocity and if his velocity would be much higher than the velocity of the wake wave behind the driver boat, he would soon abandon the accelerating phase of the wake wave (or crash into the driving boat). Thus, his energy gain is very limited. On the other hand, the velocity of the relativistic electron is only a little bit higher than the velocity of a wake wave driven by laser pulse since its velocity cannot be higher than c . However, the electron energy scales with the γ -factor which depends on the velocity as $\gamma = (1 - v^2/c^2)^{-1/2}$. In addition, thanks to the fact that the accelerated electron is still not much faster than the accelerating plasma wave; it can be sustained in an accelerating phase for a relatively long time.

Hence, even though the relative change of the electron velocity is very small, its energy gain can be very high, from initial trapping energy in order of hundreds of keV or a

few MeV it can be accelerated up to the energy in order of hundreds of MeV in the accelerating distance of a few mm or to GeV energies in cm scale capillary discharge waveguides.

The critical issue determining the properties of accelerated electron bunches, and thus subsequently the features of secondary X-ray radiation, is the way how the electrons are injected into the accelerating phase of a wakefield. There are various injection mechanisms. The simplest one is so-called self-injection. It can be understood as a consequence of the complex laser pulse evolution during the propagation through plasma leading to plasma wave-breaking. However, the nature of self-injection is very unstable; thus, reproducibility of electron bunch parameters is very low, which limits possible applications.

For this reason, a great attention is paid to the research and development of alternative injection schemes. The external injection of electrons preaccelerated in the standard radiofrequency accelerator was considered in early stages of LWFA development [Amiranoff et al., 1998] and is once again now being considered to be employed in the EuPRAXIA project focusing on superior beam quality. The simple layout of LWFA experiment becomes much more complex in this case, and it is difficult to operate electron sources and laser facilities together.

Within this work, other injection schemes which do not include such a great paradigm shift will be presented. These schemes are based on certain manipulation with the laser plasma interaction conditions. For instance, it can be done by tailoring the plasma density profile, change of a gaseous target composition, or by adding another injection pulse. A considerable contribution to this topic was done by the author during last few years because the properties of the accelerated electron bunches essentially determine the quality of X-rays from laser plasma. Thus, a special chapter of this dissertation is devoted to the issue of injection. Firstly, a Hamiltonian analysis of the physics of injection will be introduced.

3.1 1D Hamiltonian theory of electron trapping

In the framework of classical electrodynamics, the motion of electron in 1D non-linear plasma wave is described by the Hamiltonian [Esarey and Pilloff, 1995]

$$H(\xi, u_x) = \sqrt{1 + a^2(\xi) + u_x^2} - \phi(\xi) - \beta_p u_x, \quad (3.1)$$

where $u_x = p_x/m_e c$ is electron normalized longitudinal momentum. It can be calculated when the functions $a = a(\xi)$ and $\phi = \phi(\xi)$ are known; the potential can be obtained from equation (2.54) or (2.55).

The electron motion is determined by set of motion equations

$$\frac{\partial \xi}{\partial t} = \frac{\partial H}{\partial u_x} = \frac{u_x}{\sqrt{1 + a^2(\xi) + u_x^2}} - \beta_p, \quad (3.2)$$

$$\frac{\partial u_x}{\partial t} = -\frac{\partial H}{\partial \xi} = -\frac{2a \frac{da}{d\xi}}{\sqrt{1 + a^2(\xi) + u_x^2}} + \frac{d\phi}{d\xi}. \quad (3.3)$$

Because there is no explicit dependence on time in the Hamiltonian, $H(\xi, u_x) = H_0 = \text{const}$ for given electron orbit. Substituting into (3.1), we obtain quadratic equation

$$u_x^2 - 2\beta_p \gamma_p^2 (H_0 + \phi) u_x + \gamma_p^2 [1 + a^2 - (H_0 + \phi)^2] = 0. \quad (3.4)$$

Its solution $u_x = u_x(\xi)$ represents an orbit in phase space. It is given by

$$u_x(\xi) = \beta_p \gamma_p^2 (H_0 + \phi) \pm \gamma_p \sqrt{\gamma_p^2 (H_0 + \phi)^2 - (1 + a^2)}. \quad (3.5)$$

Isolines of the right hand side of (3.1) for given value of $H = H_0$ can be also understood as the electron trajectories in the phase space. Several of those trajectories are plotted in middle and bottom panels of Figures 3.1 and 3.2, respectively. The conditions corresponding to bubble regime for $a_0 = 4$ are chosen in the second example; the first one differs only with the drive pulse strength $a_0 = 0.8$. For clarity, the drive pulse envelopes, the potentials and associated electric fields evaluated numerically according to equation (2.54) are shown always in top panels of both figures.

Green solid lines in both figures are fluid orbits. They describe the electron which is initially at rest ($u_x = 0$) before the laser pulse arrival. At that moment, no plasma wave was present, thus $\phi = 0$. Its Hamiltonian is therefore, substituting into (3.1), $H_0 = 1$ and the fluid orbit is written as

$$u_x^{fluid}(\xi) = \beta_p \gamma_p^2 (1 + \phi) \pm \gamma_p \sqrt{\gamma_p^2 (1 + \phi)^2 - (1 + a^2)}. \quad (3.6)$$

The set of orbits represented by blue dashed lines corresponds to different initial values of H_0 . The closed ones represent the trapped electrons; electrons that are not trapped. The solid magenta curve represents the separatrix; it separates both these regions. This separatrix is characterized by the Hamiltonian value

$$H_{sep} = \frac{\sqrt{1 + a^2(\xi_{min})}}{\gamma_p} - \phi_{min}, \quad (3.7)$$

where ξ_{min} is the position of the minimum of electrostatic potential with the value ϕ_{min} . For $H_0 > H_{sep}$, the isolines are open and it means that the initial electron velocity is either too low or too high for trapping of electrons into the wakefield.

3. Electron injection into acceleration phase

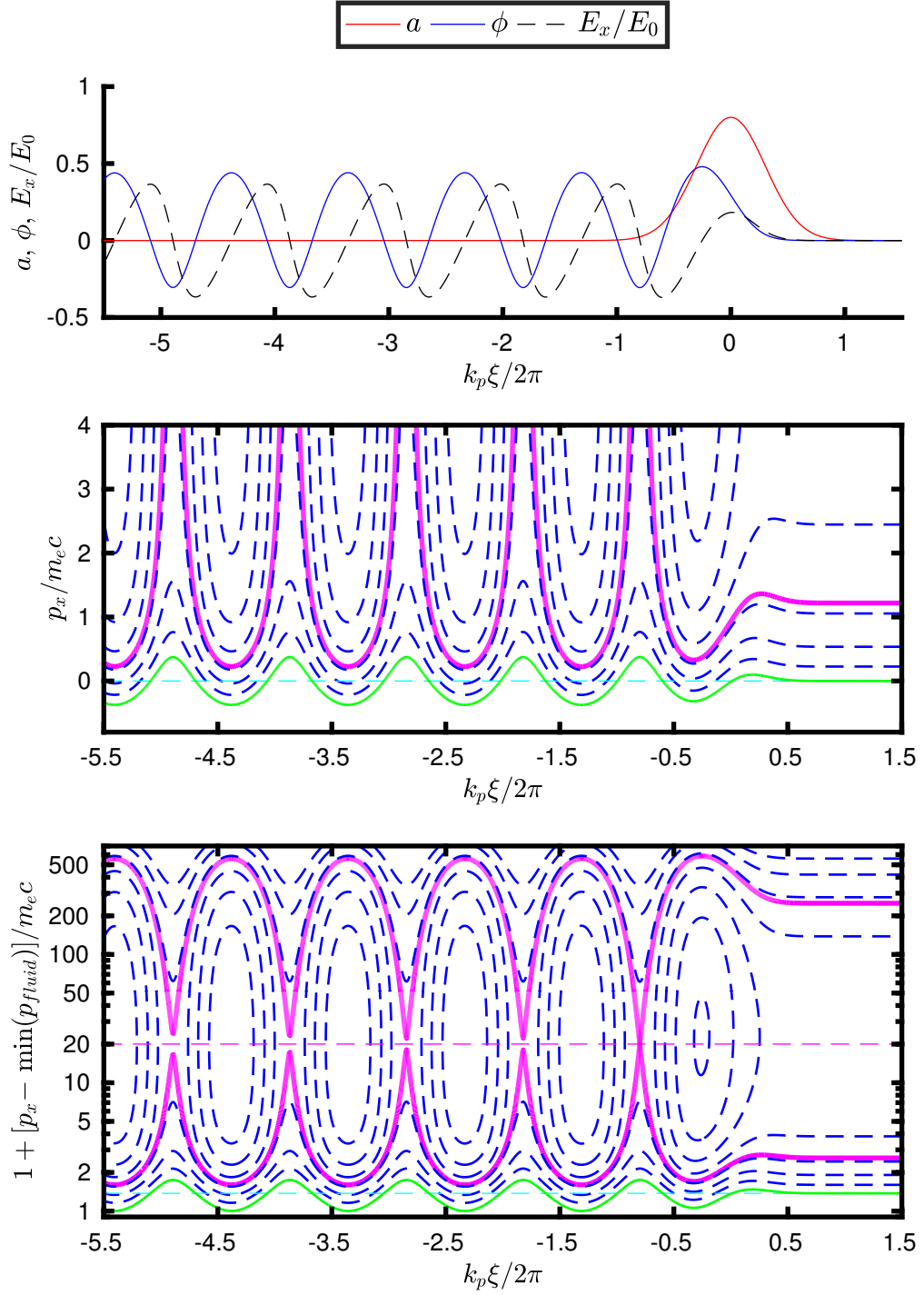


Figure 3.1: Top: the plasma potential, and associated electric field driven by Gaussian pulse with $a_0 = 0.8$, $\tau = 25$ fs for plasma density $n_e = 5 \times 10^{18} \text{ cm}^{-3}$. Middle and bottom: Electron trajectories in the phase space. Dashed magenta line represents the momentum corresponding to the phase velocity of a wake wave $u_x = \beta_p \gamma_p$, dashed cyan line is $u_x = 0$. Green line is the fluid trajectory.

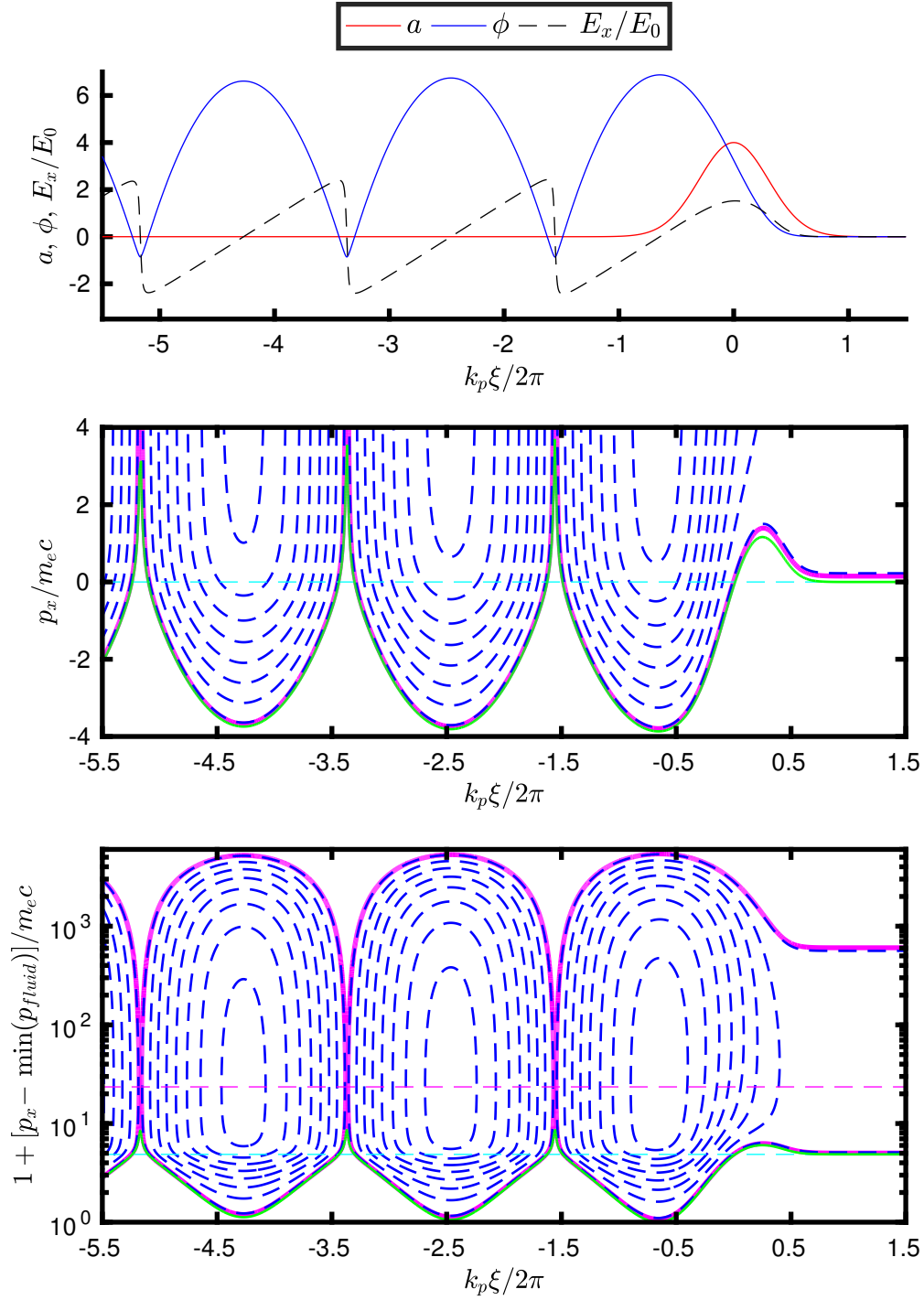


Figure 3.2: Top: the plasma potential, and associated electric field driven by Gaussian pulse with $a_0 = 4.0$, $\tau = 25$ fs for plasma density $n_e = 5 \times 10^{18} \text{ cm}^{-3}$. Middle and bottom: Electron trajectories in the phase space. Dashed magenta line represents $u_x = \beta_p \gamma_p$, dashed cyan line is $u_x = 0$. Green line is the fluid trajectory.

The separatrix has its singular point at the $(\xi_{min}, \beta_p \gamma_p)$; it is a point of crossing of the separatrix branches. The dashed magenta line represents $u_x = \beta_p \gamma_p$, the dashed cyan line represents electron at rest.

As it can be seen from Figure 3.2 for the nonlinear wakefield, the electron can be trapped even if its momentum is negative. This counter-intuitive effect will play an important role in Section 3.4.4 where a new optical injection scheme will be introduced. Once the electron is trapped in this way, it follows given trajectory (dashed blue line) in the phase space in the clockwise direction. The crossing of the magenta dashed line means that the electron velocity exceeds the plasma wave phase velocity. After that moment, the electron proceeds forward with respect to the plasma wave still acquiring the energy until the moment when it approaches the point where the potential reaches its maximum (or in other words, where the longitudinal electric field changes its sign). The acceleration process should be stopped here; otherwise, the electron enters the decelerating phase and steadily returns its energy to the plasma wave.

The electron trapping may be also understood as an overstepping of the separatrix. In particular, the distance in the phase space between fluid trajectory and the separatrix is very small in the nonlinear case. Thus, a small dephasing of the electron motion may move the electron over the separatrix.

It is necessary to note that several limiting assumptions was respected in the analysis provided above. These are the 1D theory of cold plasma and neglecting the evolution of plasma wave during its propagation in plasma. The multidimensional effects and the gradual changes in the shape (self-steepening) and intensity (self-focusing) of the driving laser pulse may lead to transverse self-injection.

3.2 Self-injection

The bubble regime introduced in Section 2.6 is currently the most promising concept of LWFA. The self-injection is still the most simple method to trap the electrons in the nonlinear wakefield. Electrons trapped by self-injection mechanism originate from background plasma, the process of trapping occurs naturally under certain conditions which are not yet well understood.

Shortly after the bubble regime was described [Pukhov and Meyer-ter Vehn, 2002]; it was demonstrated by three experimental groups and accelerated electrons achieved up to GeV energies employing the self-injection [Mangles et al., 2004, Geddes et al., 2004, Faure et al., 2004, Leemans et al., 2006]. The acceleration to GeV energies was achieved by external guiding of the plasma wave drive pulse, e.g. in capillary discharge.

| Reference | formula | comment |
|--------------------------|--|--|
| [Kostyukov et al., 2004] | $k_p R > \gamma_p$ | based on PIC simulations |
| [Lu et al., 2007] | $k_p R > 4$ | based on PIC simulations |
| [Kostyukov et al., 2009] | $k_p R > \sqrt{2}\gamma_p$ | analytical model of injection |
| [Kalmykov et al., 2009] | $\int \frac{d\xi}{v_p - v_x} \frac{\partial H}{\partial t} < -1$ | sufficient condition, phenomenological non-stationary Hamiltonian theory |
| [Froula et al., 2009] | $P/P_c > 4,$ $P_c [\text{GW}] \simeq 17\omega_L^2/\omega_p^2$ | experimental, supported with PIC simulations |
| [Thomas, 2010b] | $k_p R > 2\sqrt{\ln(2\gamma_p - 1)}$ | heuristic analytical model of injection, Lorentz boosted frame |
| [Corde et al., 2011] | $k_p R > 1.30\gamma_p$ | based on PIC simulations |
| [Thomas, 2011] | $k_p R > 2K\sqrt{\ln(2\gamma_p)},$ $K \approx 1$ | heuristic analytical model of injection, Lorentz boosted frame |
| [Mangles et al., 2012] | $\alpha\mathcal{E} > \frac{\pi\epsilon_0 m_e^2 c^5}{e^2} \times$ $[\ln(\frac{2n_c}{3n_e} - 1)]^3 \frac{n_c}{n_e} \tau(l)$ | experimental |
| [Benedetti et al., 2013] | $a_0 > 2.75\sqrt{1 + (\frac{\gamma_p}{22})^2}$ | numerical, non-evolving bubble |

Table 3.1: Overview of formulas for the self-injection threshold in bubble regime and respective references. Even though the great attention was paid to this issue, widely accepted conclusion has not yet been found [Mangles et al., 2012]. P is power of laser system, P_c is a critical power, α is a fraction of pulse energy in focal spot within FWHM of intensity. $\tau(l) \approx \tau_0 - (n_e l)/(2cn_c)$ is pulse length after propagation over the distance of l .

The properties of the self-injection process crucially influence the quality of accelerated electron beam. In the ultrahigh-intensity regime, the 1D theory based on Hamiltonian formalism introduced in previous Section 3.1 fails, because it does not include the radial force from the driver and from the plasma fields which strongly affects the electron motion. Thus, it cannot describe the physics of self-injection fully, as the dynamics of an electron and of the bubble as a whole are complex and multidimensional.

The theoretical findings stating the threshold condition for the self-injection are summarized in Table 3.1. The presented formulas were either derived from various assumptions theoretically, or empirically observed in experiments or numerical simulations. These formulas are in contradiction with one another.

Some of the formulas depend on the Lorentz factor connected with plasma wave velocity (2.39). This is often considered to be equal to laser pulse group velocity. However, it is essential to note that the phase velocity of the back of the bubble may greatly differ from this value which is closer to the velocity of a bubble front. Such an observation is very important for the physics of self-injection [Kostyukov et al., 2009, Corde et al., 2011, Benedetti et al., 2013]. Typically, this phenomenon is observed during

the bubble prolongation caused by the change of the drive pulse profile during its propagation through plasma. The velocity of the rear part of the bubble is then effectively decreased. An empirical relation for minimum bubble velocity in dependence on pulse and plasma parameters is given by [Benedetti et al., 2013]

$$\gamma_p^{(min)} \simeq 2.4 \sqrt{\frac{\omega_L}{\omega_p}}. \quad (3.8)$$

Despite all controversies, it can be concluded that the self-injection only requires that the wakefield is strong enough and that the wake phase velocity is low enough. If the bubble expands, the wake velocity at the rear of the bubble is decreased; this can trigger injection. In other words, bubble expansion is a sufficient condition for self-injection, not a necessary one. Benedetti showed [Benedetti et al., 2013] that the self-injection threshold exists even for a non-evolving bubble. In other words, for any given bubble phase velocity, the injection takes place if the laser intensity is high enough.

One author's 3D particle-in-cell (PIC) simulation of self-injection will be presented here to demonstrate the processes related to self-injection. This simulation was performed using the code EPOCH [Arber et al., 2015]. The chosen parameters are similar to the ones presented in [Kostyukov et al., 2009], they are the typical for self-injection experiments with a relatively weak laser system (~ 10 TW). The laser pulse is Gaussian, linearly polarized with initial $a_0 = 1.5$, $\tau = 30$ fs, $\lambda_L = 0.8$ μm , and $w_0 = 9.0$ μm . The uniform electron plasma density is 1.6×10^{19} cm^{-3} . It means that the laser group velocity (an estimate of plasma wave phase velocity according to equation (2.39)) is expected to be $0.9954c$, the corresponding Lorentz factor is $\gamma_p = 10.44$. The laser pulse energy is 196 mJ, peak laser power is 9.21 TW, which is $4.98P_c$. The quantity $k_p R \approx k_p w_0 = 6.81$. It means that the predictions about the injection occurrence presented in Table 3.1 are contradictory. For instance, the injection should occur according to the condition given in [Lu et al., 2007]. On the other hand, the condition given in [Kostyukov et al., 2009] is not fulfilled.

The simulation box size was $60 \times 28 \times 28$ μm^3 , the resolution was 30 and 8 cells per wavelength in longitudinal and transverse directions, respectively. Initially, 2 particles were placed into every cell.

The process of self-injection will be explained using the visualizations of the simulation results, which are depicted in Figure 3.3. The red transparent isosurfaces represent the plasma wave drive pulse propagating in the x -direction. It is clearly seen, that the shape of the pulse differs from original Gaussian function due to the processes related to its propagation in plasma. The visualization in the top panel captures the beginning of the injection; the front half of the pulse is already transformed due to

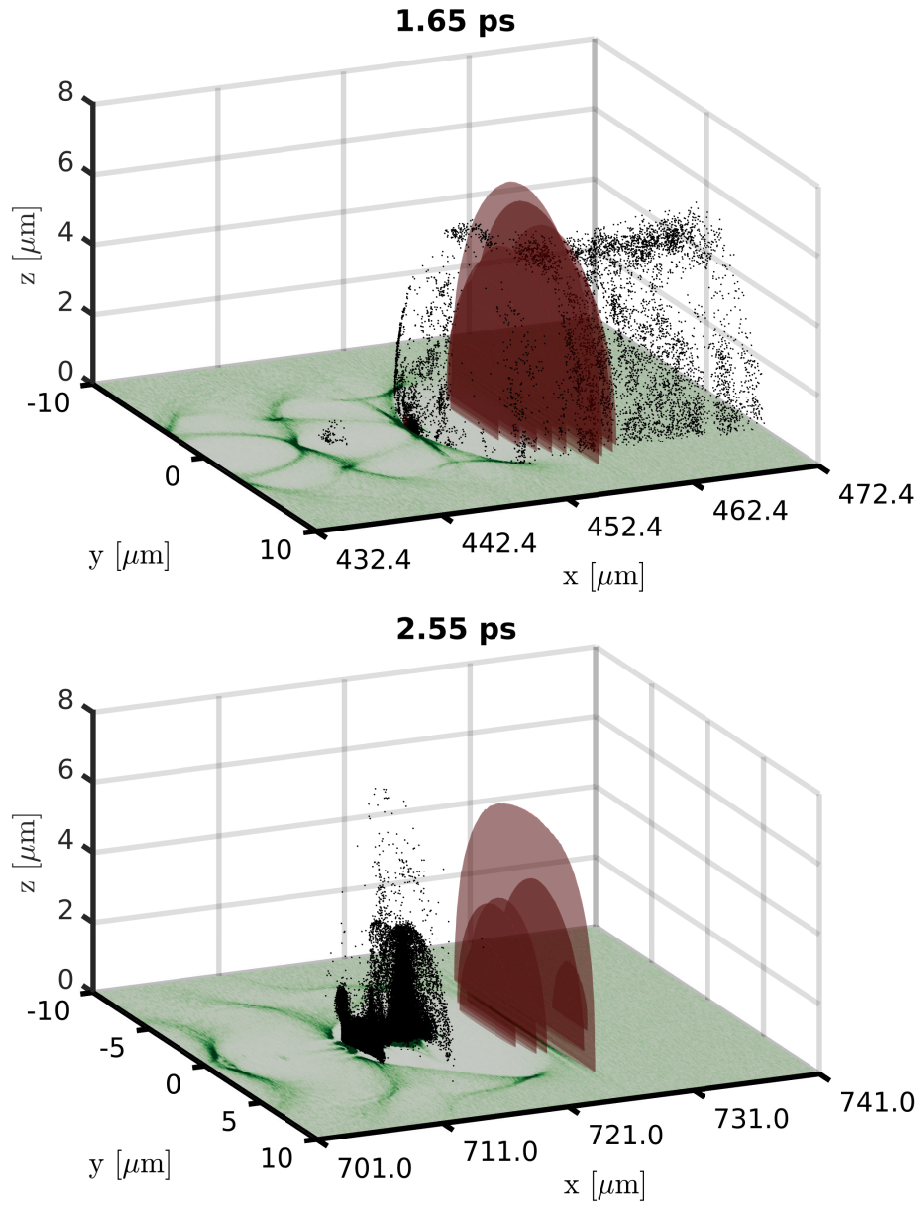


Figure 3.3: Visualization of a self-injection. Red transparent objects represent the isosurface of the electric field of the laser pulse with $E_y = 3 \times 10^{12}$ V/m. Black dots are electron macroparticles which are or will be trapped. The green colormap displays the electron density cut at $z = 0$.

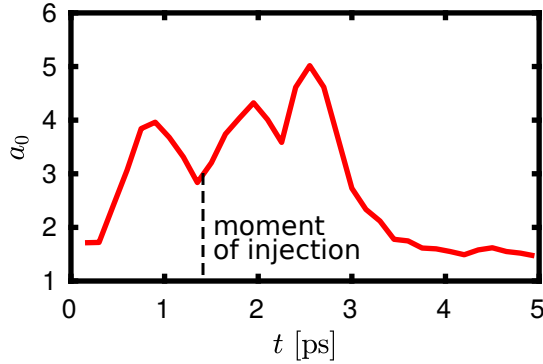


Figure 3.4: Evolution of laser strength during its propagation in target.

the process of self-steepening (the pulse front envelope is transformed into a convex shape [Esarey et al., 2009]). As a consequence, the intensity gradient is higher; thus the stronger ponderomotive force induces the bubble to expand which triggers injection in this case.

The green colormap of the bottom of the plot shows the electron density slice in the plane $z = 0$. First two periods of the plasma wave can be seen. The plasma electrons are expelled by the drive pulse ponderomotive force and they slide on the bubble edge to its rear part. The electron macroparticles which have already been trapped, are being or will be trapped, and which are located inside the selected box, are depicted as black dots. All the trapped electrons are initially located in the narrow ring around the laser axis. After the laser pulse arrived, they experience its strong ponderomotive force and are expelled out of the central high-intensity region. After that, they are affected by the plasma wave field (the azimuthal magnetic field B_θ and transverse electric field E_y), which bends their trajectories towards the axis. Such effects occur only in plasma, cf. with the case of a single electron in the vacuum, which was discussed in Figure 2.4.

Aforementioned electrons then form an electron sheath at the bubble border. As the bubble starts to expand, some electrons reach the most rear part of the bubble where they experience intense longitudinal electric field. The electrons which gain sufficient forward momentum remain in the plasma bubble and are accelerated. In this demonstration example, we can observe that the electrons are injected continuously which leads to a continuous shape of electron energy spectrum. This limits some possible applications.

Let us investigate this injection and further acceleration in more details. For instance, the graph in Figure 3.4 shows the evolution of the laser pulse maximum strength during its propagation through a plasma. Unlike the natural expectations, the pulse does not diffract; instead, the laser strength grows significantly up to $a_0 \sim 4$ in less than 1 ps due to the effect of self-focusing. The first injection phase begins at the time 1.4 ps, i.e. in

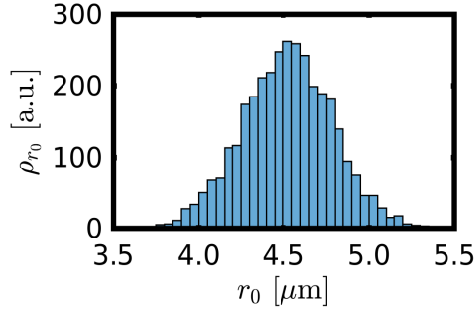


Figure 3.5: The distribution of initial radial position of electrons that will be trapped.

the time moment when the laser strength grows and the bubble expands. The maximum value of $a_0 = 5$ is reached at the time of 2.55 ps. After that, the diffraction dominates. Additionally, the laser pulse is disturbed by electrons which, as they are slightly faster than the laser pulse, already arrived in the region where the tail of the pulse is located (it occurred after 3.8 ps). Nevertheless, acceleration should be stopped at that point, since the electron beam front part is already located in the front part of the bubble where these electrons are decelerated.

As it was already stated, the electrons which are actually trapped originate from the relatively narrow ring. Its radius is $(4.5 \pm 0.3) \mu\text{m}$, the actual distribution of initial electron locations r_0 which will be trapped can be seen in Figure 3.5. This observation is in qualitative agreement with Benedetti's formula [Benedetti et al., 2013]

$$k_p r_0 = -2.0 + 1.4a_0 - 0.05a_0^2, \quad (3.9)$$

which was obtained for the case when the pulse length perfectly matches with plasma oscillations, i.e. $\omega_p \tau = 1$, which is not valid in presented case.

The graphs in Figure 3.6 describes the situation at the time of 3.0 ps. The front part of electrons begins to decelerate shortly after. The bubble and the accelerated electron bunch are shown in panel a); the phase space (x, p_x) is in panel c). The brown macroparticles correspond to black ones from Figure 3.3. The longitudinal momentum of the selected brown macroparticles is already higher than $10 m_e c$. Electrons trapped in the following buckets do not gain such a high momentum. The total charge of selected particles is 285 pC. The remaining panels show the total electron spectrum and the detail of the phase space with the selected electrons, where the finer structure can be seen.

Self-injection caused by the bubble expansion can be also intuitively explained using the separatrix introduced in Section 3.1. The bubble expansion prolongs the wakefield accelerating part. Thus, the location of the separatrix is shifted backward. The fluid electron crosses this separatrix and then stays in the first plasma wave period. Schematic

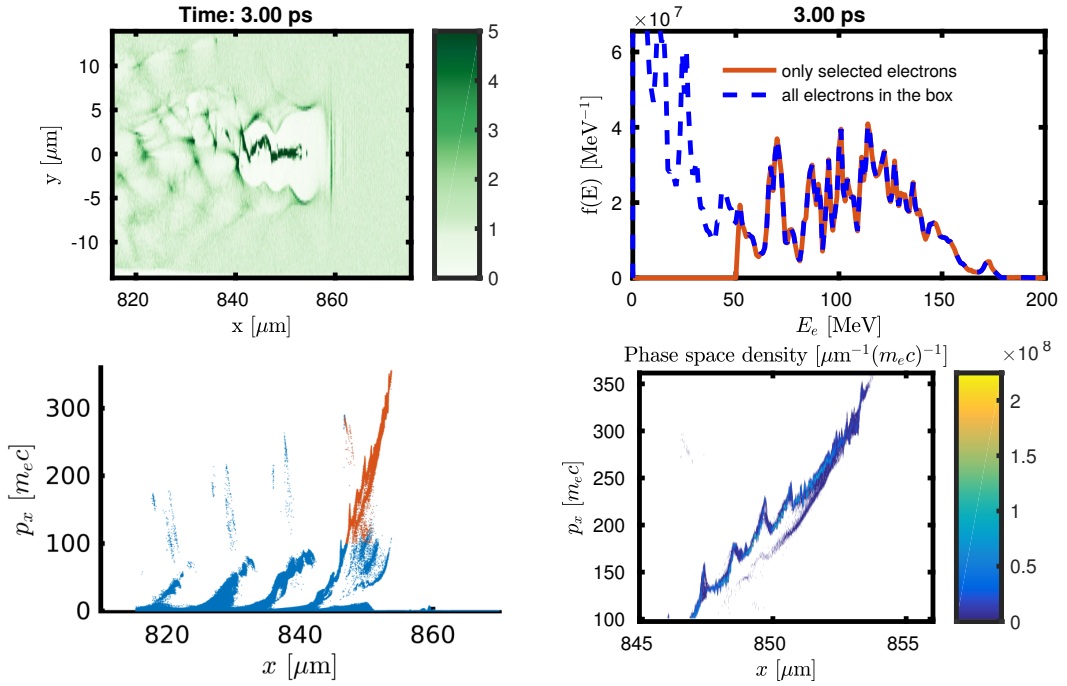


Figure 3.6: Time of 3 ps. a) Slice of electron density at $z = 0$. b) Electron energy spectrum. c) Phase space of all electrons in the simulation box. d) Phase space density of selected electrons.

illustration of this process is shown in Figure 3.7.

The presented illustrative simulation highlights also several drawbacks of the self-injection. In practice, the density is not perfectly homogeneous as assumed in the simulation and it also varies shot to shot. Thus, the processes leading to self-injection like self-focusing or self-steepening may occur differently, i.e. in a different time or with different dynamics. Even if these fluctuations can be reduced significantly by employing various intrinsic cut-offs, their influence on the properties of generated electron bunch is still essential. The greatest issue of self-injection is the low stability of measurable quantities such as total charge or energy distribution. The reproducibility of generated electron bunches is very low and it limits possible applications. This drawback can be overcome by employing alternative injection schemes, which will be introduced in following sections.

Chosen simulation parameters are very similar to those which were employed during the experimental campaign at the Ti:sapphire laser system at the PALS research center in 2015–2017. However, the self-injection did not occur. According to the author’s opinion, the relatively long laser pulse length (≈ 50 fs) is the most critical issue. In this experiment, approximately 360 mJ of energy was focused to the spot with diameter ~ 12 μm . Laser

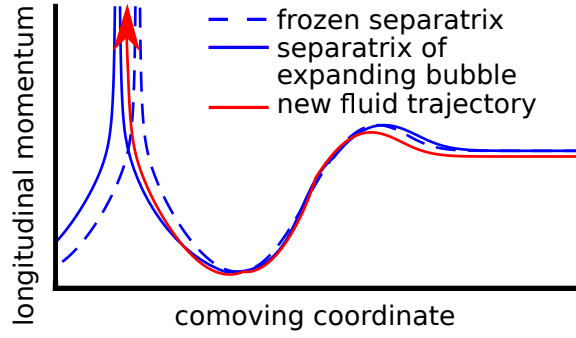


Figure 3.7: Schematic illustration of injection caused by the bubble expansion.

strength parameter $a_0 > 2$ in this case. The initial target density was varied in a large range without any success.

Let us compare this configuration with the simulation visualization from Figure 3.3. The smaller size of the laser focus generates a smaller bubble. On the other hand, longer pulse fills whole bubble volume. Thus, no electrons can remain in the bubble, because of the presence of the laser pulse which ejects them from there.

3.3 Density down-ramp injection

The prolongation of the bubble can be also achieved in a controlled manner by a density down-ramp transition [Bulanov et al., 1998, Suk et al., 2001, Brantov et al., 2008]. In practice, such conditions are achieved by adding an obstacle such as a razor blade into the gas jet [Schmid et al., 2010, He et al., 2013] or by using another laser pulse [Faure et al., 2010].

As the laser pulse dragging the bubble penetrates through the density transition, the bubble is expanding. It can be understood in a way that the phase velocity of the rear side of the bubble decreases and can drop so low that the condition for the self-injection will be fulfilled.

After the pulse and the bubble reaches the plateau region again, the length of the bubble is stabilized, and further potential injection is suppressed. Therefore, in principle, this injection is localized and it leads to the generation of the electron bunches with low energy spread. In an experiment [Barber et al., 2017], it was revealed that density down-ramp injection produces beams with normalized emittances a factor of 2 smaller than beams produced via ionization injection for modest laser system parameters ($\mathcal{E} = 1.8$ J, $\tau = 45$ fs, $w_0 = 22$ μm).

Recent numerical study [Massimo et al., 2018] accented the relatively strong dependence of the generated electron bunch properties on the ramp length. Namely, high

charge bunches are generated with short density ramps.

■ 3.4 Optical injection

The fundamental motivation for using alternative injection techniques is to separate the wakefield generation and the electron injection into this wakefield. Such an approach was designed with the intention to stabilize the produced electron beam properties. In optical injection configuration, the drive pulse is responsible for the formation of the wake wave, and an additional injection pulse injects electron bunch into an accelerating phase of this wakefield in a controlled manner.

This technology requires an accurate temporal and spatial synchronization of both plasma wave drive pulse and injection pulse. Such a synchronization is standard with current compact CPA technology [Zhang et al., 2003a]. The injection pulse influences the dynamics of a plasma wave or plasma electrons and it triggers the injection.

■ 3.4.1 Ponderomotive injection

Optical injection scheme was firstly proposed [Umstadter et al., 1996] and further elaborated [Dodd et al., 1997, Dodd et al., 2004] by Umstadter et al., both by analytical calculation and numerical simulation (PIC 1D3V). The first laser pulse drives the plasma wave via standard LWFA mechanism; the second injection pulse orthogonally intersects the wakefield at a certain distance behind the drive pulse. The polarization of the injection pulse is in the drive pulse propagation direction. Transverse ponderomotive force associated with injection pulse is large enough so that a part of plasma electrons gain the momentum kick which preaccelerates them sufficiently to cross the wakefield separatrix. As a consequence, they are trapped in the wakefield and further accelerated to high energies. Both pulses do not overlap in space and time; no beatwave pattern is generated. The schematic drawing of this configuration and the injection process is drawn in Figure 3.8.

The injection pulse was suggested to be even stronger than the pump pulse. For instance, the following example was presented. The intended laser strength parameter of the main pulse should have been $a_0 = 1.0$, while the threshold value for the injection beam laser strength parameter was $a_1 \gtrsim 1.6$. The natural drawback is that such a strong injection beam could potentially destroy the wakefield structure.

Additional numerical simulations pointed out that another injection mechanism may occur due to the influence of the wake dragged by the injection pulse [Hemker et al., 1998, Hemker, 2015].

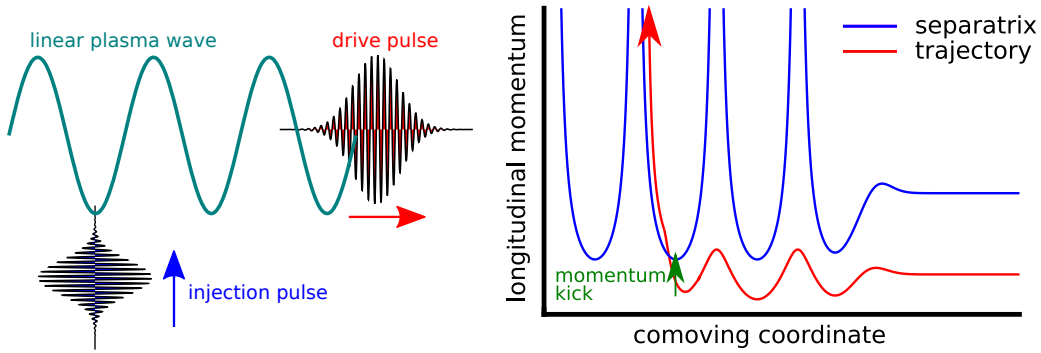


Figure 3.8: Original design of optical injection scheme suggested in [Umstadter et al., 1996]. Left: Configuration of both pulses. Right: Electron trajectory in the phase space illustrates the injection principle.

These pioneer works were performed in 1990's when the bubble regime has not been discovered yet [Pukhov and Meyer-ter Vehn, 2002] and only the linear regime of laser wakefield acceleration was considered. Another big concern was connected with the possible issues related to the proper synchronization of both femtosecond pulses. Such a synchronization was experimentally demonstrated later though [Zhang et al., 2003b].

Last modification of this scheme represents the head-on collision of two injection pulses which are propagating orthogonally to the drive pulse direction and overlap in the first plasma wave period behind the drive pulse with $a_0 \approx 1.5$ [Chen et al., 2012b]. Two identical injection pulses are linearly polarized with $a_{1,2} \approx 0.8$. Their electric field vector is oriented along the propagation direction of the driver pulse. A standing wave arises when both injection pulses overlap; the electrons located in this interaction region can gain sufficient momentum kick to be trapped within the first or the second plasma wave period. It was also noted that the injected charge can be increased by adding nitrogen to the standard helium gas, which may result in ionization injection.

3.4.2 Injection by counter-propagating pulse

Alternative optical injection technique differs significantly from ponderomotive injection introduced in the previous section. Injection by the colliding pulses [Esarey et al., 1997] is induced by the ponderomotive force associated with the beat wave pattern of two counter-propagation intersecting injection pulses. Three pulses are considered in the original proposal. A relatively intense pump (drive) pulse ($a_0 \simeq 1$) drives the linear plasma wave; one forward directed injection pulse follows the drive pulse with a certain delay; the last injection pulse is directed backward. The injection pulses are relatively weak ($a_{1,2} \simeq 0.2$) polarizations are orthogonal to the drive pulse polarization; it means

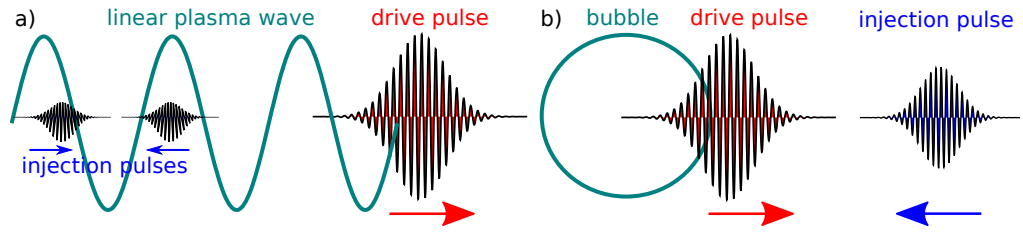


Figure 3.9: a) Original injection scheme by three pulses [Esarey et al., 1997] b) Injection by counter-propagating laser beam introduced in [Fubiani et al., 2004] and [Kotaki et al., 2004].

that injection pulses do not interfere with the drive pulse. The delay between drive pulse and forward-going injection pulse determines the position of the injected electron. The scheme of this injection mechanism is shown in Figure 3.9a).

The principle of this injection is based on the electron behavior in the beat wave pattern without the presence of the wakefield. These electrons oscillate in the beatwave and the direction of these oscillations is longitudinal. Their immediate forward momentum gain can be high enough to cross the separatrix. Thus, the schematic trajectory of the injected electron in the phase space would be similar as in previous ponderomotive injection case shown in Figure 3.8.

Fubiani [Fubiani et al., 2004] and Kotaki [Kotaki et al., 2004] independently suggested the simplification of this scheme. Only single counter-propagating injection pulse is considered; its polarization is the same as the one of the nonlinear plasma wave drive pulse; the schematic drawing is shown in Figure 3.9b). Such a method is also called the warm optical injection [Nakamura et al., 2004, Wang and Sheng, 2008]. The principle of this injection scheme is such that the injection pulse beats with the tail of the drive pulse. This leads to trapping of some plasma electrons into the bubble. The effects of the interaction angle and polarization were also explored [Fubiani et al., 2004], e.g., efficient trapping can occur for near-collinear geometries.

The advantage of this approach in comparison with the previous one is such that this scheme is easier to implement in an experiment. As the injection pulse is intended to be very weak in comparison with the pump pulse, it does not perturb the wakefield structure noticeably. On the other hand, the injection pulse has to propagate through long plasma region before the collision with the pump pulse and due to its low intensity, it is susceptible to defocusing.

This scheme was experimentally demonstrated as well [Faure et al., 2006], and the stable generation of collimated (5 mrad divergence), monoenergetic (with energy spread $\lesssim 10\%$), tunable (between 15 and 250 MeV) electron beams was reported. When

polarizations of the two pulses were orthogonal, no electron beam was produced.

Nevertheless, both theoretical and experimental studies [Rechatin et al., 2009c] of the effect of mutual polarizations in the interaction of two colliding laser pulses proved that the electron injection is also possible for different configurations. The injection mechanism was identified as stochastic heating occurring due to collision of two cross-polarized laser pulses; however, its injection threshold is higher than in the parallel polarization scheme.

Further theoretical study [Davoine et al., 2009] of counter-propagating circularly polarized laser pulses collision in low-density plasmas suggested the generation of electron bunches with even lower energy spread. This method known as the cold optical injection uses an injection pulse of a very low intensity. Unlike previous configurations of colliding pulses, electron heating is not the cause of injection. The collision between pulses creates a spatially periodic and time-independent beat force which blocks longitudinal electron motion, and thus, some electrons enter the wake wave at a position allowing their injection.

The most recent milestone achieved is the optical transverse injection [Lehe et al., 2013]. It leads to further improvement of electron bunch parameters, i.e., possibility to generate high-quality electron bunches having both a very low emittance⁶ and an energy spread while keeping a high charge and a short length. This particular regime is characterized by a different mechanism of the injection. The bubble as a whole is strongly affected during the pulse collision. This collision reduces the efficiency of the transverse ponderomotive force. Thus, the whole bubble becomes shorter. After the collision, the bubble recovers its original shape; such an expansion triggers injection. This effect is similar to the case of self-injection introduced in Section 3.2. However, the bubble prolongation is now controlled which leads to much higher stability of the scheme. The schematic illustration of the separatrix crossing would be similar to the one shown in Figure 3.7.

3.4.3 Injection by orthogonally crossed pulse

Wang *et al.* [Wang et al., 2008] returned the attention back to the perpendicular pulses. In this case, two pulses meet after a short distance of propagation while the acceleration distance of electron beams can still be long enough. A certain advantage of these schemes is the possibility to adjust the experimental configuration in a way that the injection pulse propagates through plasmas only on a short distance and therefore without its deformation.

⁶ Longitudinal and transverse emittance are a beam quality figure of merit. They are usually calculated according to formula [Floettmann, 2003b, Floettmann, 2003a] as $\varepsilon_x = \sqrt{\langle(x - \langle x \rangle)^2 \rangle \langle p_x^2 \rangle - \langle(x - \langle x \rangle)p_x \rangle^2} / m_e c$ and $\varepsilon_y = \sqrt{\langle y^2 \rangle \langle p_y^2 \rangle - \langle y p_y \rangle^2} / m_e c$, where x and y are space coordinates and $p_{x,y}$ are momenta of trapped particles. Definition of ε_z is analogical to ε_y .

In an experiment, strong enhancement of energetic electron number was observed when two crossed pulses with parallel polarizations collided [Zhang et al., 2003a]. Although this experiment was not aimed at the electron acceleration to multi-MeV energies, it proved the technical feasibility of the configuration with the two perpendicularly colliding laser pulses in a plasma.

The configuration with the same polarization perpendicular to the plane formed by propagation directions of both pulses was chosen. It was found that an injection occurs even if the injection pulse is much weaker than the drive pulse. It was claimed that the electron injection and acceleration processes are the same as the colliding pulse injection scheme [Fubiani et al., 2004, Kotaki et al., 2004] and consequently have better controllability and stability. In order to suppress a self-injection, an additional third pulse following the pump pulse and destroying the second and further periods of the wake wave can be introduced into this scheme.

The process is presented for the linear regime of laser wakefield acceleration with $a_0 \approx 1.5$. This scheme differs from ponderomotive injection [Umstadter et al., 1996] because the two pulses actually intersect and generate a beatwave pattern. Both of the schemes with the orthogonally directed pulses [Umstadter et al., 1996, Wang et al., 2008] operated in the linear regime, partly because of the availability of the state-of-the-art laser systems at that time, but mainly to avoid the self-injection of electrons in the case of the bubble regime.

■ 3.4.4 Orthogonally crossed pulses with perpendicular polarizations

As a part of this work, a certain redesign of an optical injection by orthogonally directed injection pulse concept is proposed. This redesign reacts on the progress of the laser technology and physical understanding. The proposed scheme can operate on a highly non-linear regime of LWFA ($a_0 > 2$ and even higher) and the injection pulse is supposed to be very weak in comparison with the pump pulse $a_1 \sim 0.1a_0$ to avoid its disturbing effect on the bubble dynamics. The main findings supported by 2D PIC simulations were published in journal paper [Horný et al., 2017b] and conference proceedings paper [Horný et al., 2017c]. The explanation of this injection principle and other related findings will be mainly the rephrasing of these original works.

The suggested optical injection scheme is depicted in Figure 3.10. As the large intensity of the pump pulse is assumed in this scheme, there is no requirement of high plasma density to induce self-focusing to sustain sufficient intensity and the wakefield structure. As the time when self-injection occurs increases with the decreasing plasma density, the acceleration of the optically injected bunch may take places well before self-injection

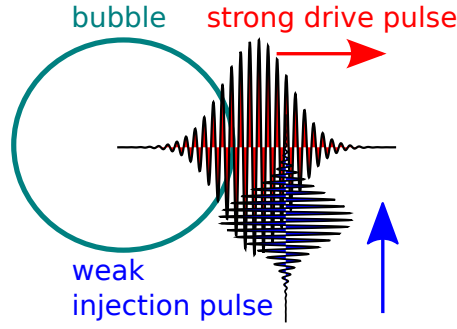


Figure 3.10: The strong laser pulse crosses with the weak injection pulse in the underdense plasma in order to induce trapping of electrons from the interaction region into its wakefield.

occurs. It means that the potential self-injection is not of great concern in the presented injection scheme. Mechanisms to filter the lower energy electrons with the magnetic field [Umstadter et al., 1996] or by using the slightly delayed laser pulse [Wang et al., 2008] may be still applied.

A typical bubble regime achievable with standard ~ 100 TW laser systems is chosen for demonstration of the injection mechanism for the configuration of crossed colliding laser beams. The following parameters are used: the plasma density $n_e = 5 \times 10^{18} \text{ cm}^{-3}$, drive laser pulse (DP) wavelength $\lambda = 0.8 \text{ }\mu\text{m}$, waist size (radius at $1/e^2$ of maximum intensity) $w_0 = 9.5 \text{ }\mu\text{m}$, pulse length (FWHM) $\tau = 25 \text{ fs}$, and intensity $a_0 = 4$ ($I_{DP} = 3.42 \times 10^{19} \text{ W/cm}^2$). The injection pulse has the same fundamental parameters, but intensity. Both pulses are linearly polarized with the polarization vectors lying in the same plane being mutually perpendicular, but the drive and injection pulses are crossing each other in the same focal spot at the same time in this case. This configuration of orientations and polarizations will be called the Orthogonally Crossing Pulses with Perpendicular Polarizations (OC3P).

■ Numerical PIC simulations

All the PIC simulations were carried out using the 2D version of the code EPOCH [Arber et al., 2015]. Simulations indicate that a larger number of injected electrons is at first expelled out of the high-intensity region of the collision of both pulses. Then they are trapped and further accelerated by the wake wave arising behind the driving pulse. A lower number of the injected electrons is firstly preaccelerated in the field of the driving pulse; then they are slowed down, expelled from the high-intensity region and after that trapped by the wake wave. The injection process is described in more details later.

The shape of the resulting electron energy spectrum depends on the injection beam intensity. Figure 3.11 shows the energy spectra of accelerated electrons at 8 ps of

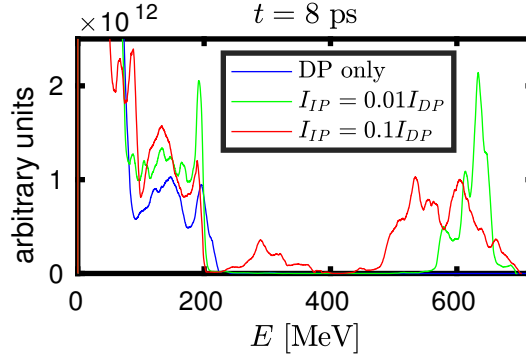


Figure 3.11: Energy spectra of accelerated electrons for the OC3P case with $a_0 = 4$ and varying injection pulse intensity at the time of 8 ps of simulation. As the spectrum is divided into two parts in cases with injection pulse present, the low energy part can be easily filtered and thus a narrow spectrum obtained. For $a_1 = 0.4$ we have: $\langle E_{el} \rangle = 634$ MeV, $\Delta E_{el} = 24$ MeV. Figure taken from [Horný et al., 2017b].

acceleration for the OC3P case. The peak value of the electron energy in the optically injected bunch is about 630 MeV at that time moment. The spectrum is quasimonenergetic in the case when the injection pulse intensity is only 1 % of the drive pulse intensity. The energy spread is lower than in the case of the parallel polarization or when the bunch is injected by a counter-propagating pulse for the same parameters of laser pulses. It is worth noting that the injection pulse being very weak in comparison with the drive pulse does not disturb the bubble dynamics and the self-injection (occurring at time $t \approx 5$ ps in all the cases in Figure 3.11).

The group of trapped electrons has a large mean energy with a low energy spread and is separated by a rather large energy interval from the lower energy electrons. Variations of the distribution function at the time of 2 ps as a function of the injection pulse intensity are plotted in Figure 3.12 to demonstrate the injection threshold. The light blue curve ($I_{IP} = 0.0016 I_{DP}$) is at the injection threshold, and a very low peak is formed. On the other hand, a narrow peak is formed on the red and magenta curves at $I_{IP} = 0.0036 - 0.0064 I_{DP}$. For higher injection beam intensities, black and green curves, $I_{IP} = 0.0144 - 0.0196 I_{DP}$, the peak of the accelerated electrons slightly grows, but it has a larger energy spread; there is also a larger amount of lower energy electrons nearby.

It can be seen that the case of $I_{IP} = 0.01 I_{DP}$ (blue curve) is a reasonable choice for getting a good quality accelerated bunch.

The energy of the electron beam seems to decrease when the energy of the injector laser pulse increases. However, the reason why e.g. the energy of the electron bunch

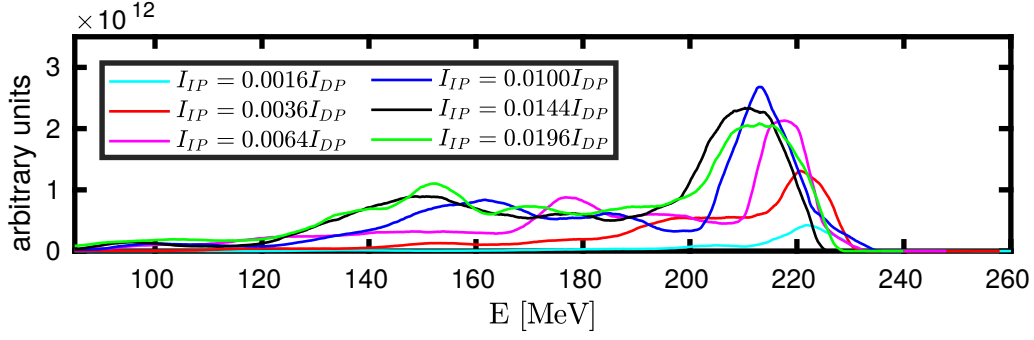


Figure 3.12: Energy distribution function of accelerated electrons (the OC3P case) as a function of the injection pulse intensity. The drive pulse strength is $a_0 = 4$. Injection threshold is around $a_1 = 0.16$, i.e. $I_{IP}/I_{DP} = 0.0016$. Figure taken from [Horný et al., 2017b].

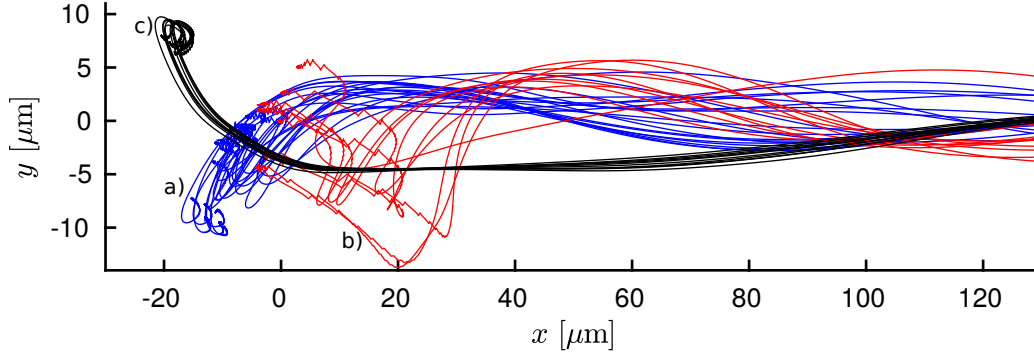


Figure 3.13: Trajectories of selected particles forming the accelerated bunch, PIC simulations. a) crossing beatwave injection, b) injection by laser field preacceleration, c) induced self-injection. Figure taken from [Horný et al., 2017b].

injected by the weaker injection pulse is higher is that lower charge is injected. This explanation is consistent with the experiment [Rechatin et al., 2009b] which was aimed at the controlling the phase-space volume of injected electrons for the counter-propagating pulses. Authors conclude [Rechatin et al., 2009a] that the cause of this phenomenon is related to the effect of beam loading [Katsouleas and Su, 1987].

Overview of injection mechanisms

A natural question is, how the optical injection arises. In the following Figures 3.14 and 3.13, the positions of injected particles are shown and their trajectories are shown in more details during their trapping and acceleration in the first bubble.

The OC3P injection consists of three different injection mechanisms. Electrons which can be trapped and injected into the wakefield lie in three different initial regions (see

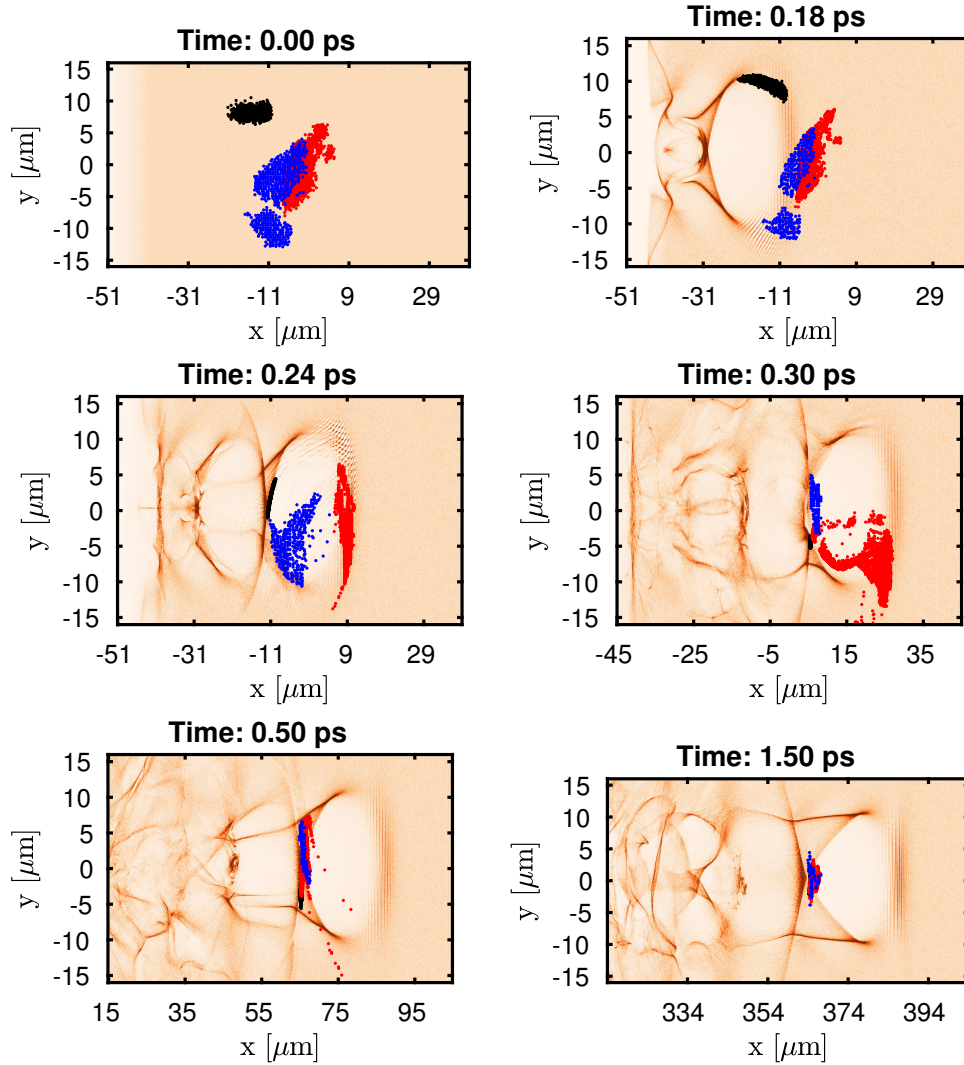


Figure 3.14: Time sequence of injected electron positions (blue – crossing beatwave injection, red – injection by laser field preacceleration, and black – induced self-injection) in OC3P case with $I_{IP} = 0.01I_{DP}$. Electron density is in the background to show the position of the bubble. Simulations of optical injection by perpendicularly crossing laser pulses. The drive pulse propagates from the left to the right, the injection pulse propagates from the bottom to the top. Their foci meet at $x=0$. Figure taken from [Horný et al., 2017b].

Figure 3.14) and follow different sorts of trajectories.

The *crossing beatwave injection* (blue in Figure 3.14 and 3.13) represents a dominant mechanism; approximately 70 % of trapped electrons are injected in this way. A large number of electrons is expelled out of the high-intensity region in the pulse crossing region due to the action of the field of both pulses. However, due to the presence of strong electrostatic fields ($E_x \approx -200$ GV/m, $E_y \approx -110$ GV/m) of the plasma wave driven by the drive pulse, they are accelerated in direction of the drive pulse propagation. Because of such a significant momentum gain in the plasma wave propagation direction ($\approx 10 m_e c$), these electrons stay in the accelerating field, i.e. they are trapped. As a consequence, the intensity of the injection pulse can be as small as $0.01 I_{DP}$, because the trapped electrons gain the momentum necessary for injection from the plasma wave and not directly from the injection pulse, as considered in [Umstadter et al., 1996, Dodd et al., 2004].

This process can be understood in a way that stochastic heating shifts electrons into the wake wave where they are trapped despite having a negative longitudinal momentum, similarly as in the case of cold optical injection [Davoine et al., 2009]. However, this process is different, because in the OC3P case the longitudinal electron motion is not frozen, and the cause of the injection is in the complex solution of its motion in the presence of the combined field of both pulses, as will be discussed further. Single electron trajectory in the phase space is shown in Figure 3.15.

Injection by laser field preacceleration (red in Figure 3.14 and 3.13): A lower number of electrons is dephased during the collision of both pulses, then trapped by the drive pulse, and (pre-)accelerated by the direct laser acceleration mechanism. Due to their non-zero transverse momentum, they are gradually being ejected from the high-intensity region. Afterward, they are trapped by the wake wave dragged by this pulse thanks to the sufficient forward momentum they gained. The presence of the injection pulse is therefore crucial for this injection mechanism.

The trajectory in the momentum space of an example trapped electron is depicted in Figure 3.15. Approximately 20 % of trapped electrons are injected by this mechanism.

Induced self-injection (black in Figure 3.14 and 3.13): A relatively low number of electrons is trapped due to the mechanism similar to standard transverse self-injection. They are initially located in the self-injection collection volume [Benedetti et al., 2013]; after the passage of the drive pulse, they slide on the ion cavity edge. They reach the rear part of the ion cavity at the same time as electrons injected by the crossing beatwave injection mechanism. Those electrons influence local electrostatic fields; thus they trigger the self-injection. Approximately 10 % of trapped electrons are injected by this induced mechanism.

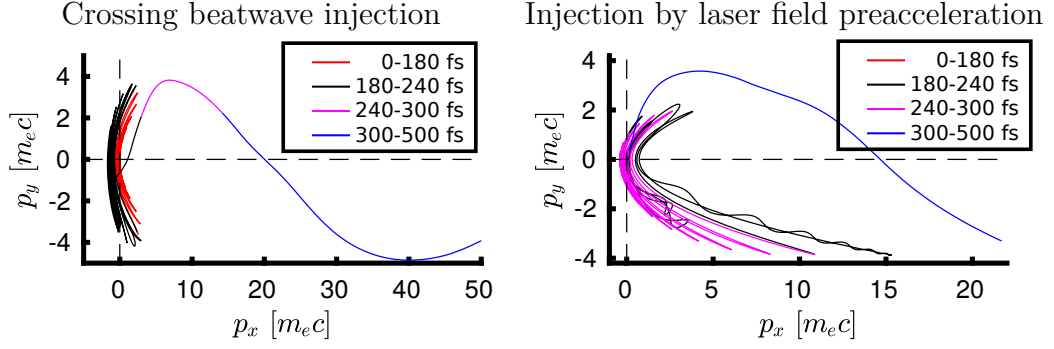


Figure 3.15: Left: Momentum space evolution of the test electron trapped by the crossing beatwave injection. This electron gains longitudinal momentum also in the time interval 180–240 fs, i.e. in the time interval when the injection pulse already crosses the drive pulse (cf. interference pattern in density in respective panels of Figure 3.14). Right: Momentum space evolution of test electron trapped by the laser field preacceleration injection. The electron is at first carried by the drive pulse, afterward ejected out of the high-intensity region to the ion cavity. It is being shifted to the rear part of the bubble where it is trapped by its strong longitudinal electrostatic field. Figure taken from [Horný et al., 2017b].

Theoretical model of injection

The electron motion in the presence of a superposed field of both pulses will be studied theoretically in this section. Even though derived equations cannot be integrated analytically, their analysis will illustrate the basic physical phenomena responsible for the injection.

The normalized vector potentials of both laser pulses can be written as

$$\mathbf{a}_0 = a_0 \mathbf{e}_0 \cos(\omega_0 t - k_0 x) \exp \left[-\frac{(x - ct)^2}{\tau_0^2} \right] \exp \left(-\frac{y^2}{w_0^2} \right), \quad (3.10)$$

$$\mathbf{a}_1 = a_1 \mathbf{e}_1 \cos(\omega_1 t - k_1 y) \exp \left[-\frac{(y - ct)^2}{\tau_1^2} \right] \exp \left(-\frac{x^2}{w_1^2} \right), \quad (3.11)$$

where $\mathbf{e}_{0,1}$, $\omega_{0,1}$, $k_{0,1}$, $\tau_{0,1}$ and $w_{0,1}$ are unit polarization vector, frequency, wavenumber, duration and waist size of drive and injection pulses, respectively. Unit polarization vectors are $\mathbf{e}_0 = (0, 1, 0)^T$ and $\mathbf{e}_1 = (1, 0, 0)^T$ for OC3P scheme, and $\mathbf{e}_0 = \mathbf{e}_1 = (0, 0, 1)^T$ for the scheme suggested in [Wang et al., 2008].

Using this expression, time-averaged electron equations of motion in the presence of

these pulses can be constructed:

$$\frac{dp_x}{dt} = -\frac{m_e c}{2\gamma} \frac{\partial \mathbf{a}^2}{\partial x}, \quad (3.12)$$

$$\frac{dp_y}{dt} = -\frac{m_e c}{2\gamma} \frac{\partial \mathbf{a}^2}{\partial y}, \quad (3.13)$$

$$\frac{dx}{dt} = \frac{p_x}{m_e \gamma}, \quad (3.14)$$

$$\frac{dy}{dt} = \frac{p_y}{m_e \gamma}, \quad (3.15)$$

where $\mathbf{a} = \mathbf{a}_0 + \mathbf{a}_1$.

In the crossing region, where $|x - ct| < \tau_0$, $|y - ct| < \tau_1$, $|y| < w_0$ and $|x| < w_1$, following relations are valid for all possible configurations of polarization vectors of both laser pulses:

$$\left| \frac{\partial \mathbf{a}_1^2}{\partial x} \right| \ll \left| \frac{\partial \mathbf{a}_0^2}{\partial x} \right| \approx 0, \quad (3.16)$$

$$\left| \frac{\partial \mathbf{a}_1^2}{\partial y} \right| \ll \left| \frac{\partial \mathbf{a}_0^2}{\partial y} \right| \approx 0. \quad (3.17)$$

Contrary to the parallel polarization case [Wang et al., 2008], where the injection is caused by the beatwave ponderomotive force, i.e.

$$\frac{\partial \mathbf{a}_0 \cdot \mathbf{a}_1}{\partial x} \approx -a_0 a_1 k_0 \sin(\omega_0 t - k_0 x) \cos(\omega_1 t - k_1 y) \quad (3.18)$$

$$\frac{\partial \mathbf{a}_0 \cdot \mathbf{a}_1}{\partial y} \approx -a_0 a_1 k_1 \cos(\omega_0 t - k_0 x) \sin(\omega_1 t - k_1 y), \quad (3.19)$$

the above mentioned terms are zero in the OC3P case. Moreover for both schemes (OC3P and the one from [Wang et al., 2008]), the time-average of equations (3.18) and (3.19) is also zero. Nevertheless, the injection in the OC3P case is still present, it is caused by motion of electrons in crossing beatwave pattern. Such electrons can be later trapped and accelerated [Davoine et al., 2008, Mendonca, 1983, Sheng et al., 2002, Bellan, 2008].

The dominant injection mechanism of the crossing beatwave injection can be further analyzed numerically. For this purpose, the injection process is divided into two stages, when the interaction of the electrons with the combined field of both pulses dominates over forces connected with plasma and vice versa. Such methodology allows recognizing fundamental phenomena leading to injection.

The first stage is studied with the model of an electron in vacuum experiencing the field of the single laser pulse, and of two colliding pulses. Its relativistic equations of motion were integrated numerically. The fields of the pulses were modeled as Gaussian beams [Wang et al., 1997]. Simulation results for the case with a single pulse have been already

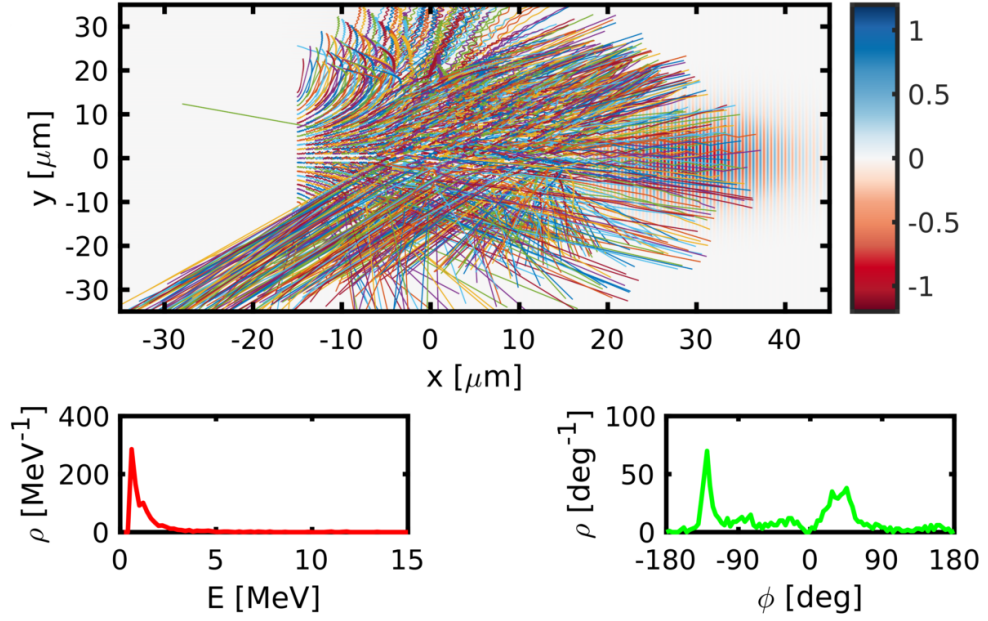


Figure 3.16: Trajectories of individual electrons obtained from the solution of the relativistic motion equation of individual electrons in vacuum in case when both laser pulses are present. The test particles are initially at rest and located on a grid in a square 30×30 microns. Red and blue colors represent the magnetic field in the z -direction in the units of the drive pulse peak magnetic field. Snapshots at the time of $t = 97$ fs after the drive pulse crossed its focal point at $x = 0$ are displayed. Main pulse parameters are: $\lambda_L = 0.8 \mu\text{m}$, $w_0 = 9.5 \mu\text{m}$, $\tau = 25$ fs, $a_0 = 4$. Injection pulse is the same, but $a_1 = 0.4$. Both pulses meet at the point $[0,0]$ at the time of $t = 0$. The strong electron expulsion in the direction bottom-left is clearly seen both in the trajectories and as a strong peak at -135° in the angular distribution. Graphs in the bottom frame show the energy and the angular distributions of given sample of electrons. Compare with Figure 2.4. Figure inspired by [Horný et al., 2017b].

depicted in Figure 2.4. This case with no injection pulse can be compared with the OC3P case with the injection pulse with $100\times$ lower intensity shown in Figure 3.16. A clear difference in behaviour is apparent despite such a small difference in initial conditions. In the OC3P case, there is a significant group of electrons which were expelled from their initial positions in the direction bottom-left by the combined action of the field of both pulses. Their energy gain is up to 2.5 MeV, similarly as in PIC simulations presented earlier. In the plasma, they would be trapped by the plasma wave, as it will be shown further in the text when analyzing the second stage.

The same effect was observed also for even weaker injection pulse down to $a_1 = 0.08$ keeping $a_0 = 4$. The effect vanishes for lower a_1 . Such an observation is in the good agreement with the PIC simulations, cf. Figure 3.12. In addition, the broadening of the

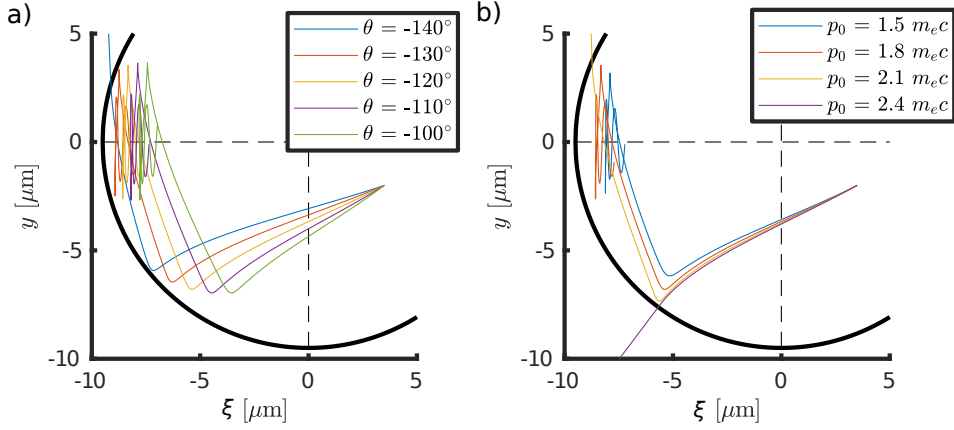


Figure 3.17: Trajectories of test electrons moving in the electric and magnetic fields of the ion cavity, which were initially located at point $[3.5 \mu\text{m}, -2 \mu\text{m}]$. (a) initial momentum $p_0 = 1.8 m_e c$ and varying elevation angle, and (b) initial elevation angle -120° and varying initial momentum size. Black solid arc represents the border of the bubble.

angular and energy spectrum which is observed here in the presence of injection pulse is a characteristic feature of the stochastic heating [Bellan, 2008].

Since, without the presence of the bubble, no electrons can be trapped and accelerated, the injection mechanism was further investigated using the analytical model of electric and magnetic fields inside the ion cavity. The spherical ion cavity with infinitely thin electron sheath at its border was assumed. In this case, the resulting fields take shape [Kostyukov et al., 2004, Lu et al., 2006, Esarey et al., 2009]

$$E_x = \frac{m_e \omega_p^2}{2|e|} \xi, \quad (3.20)$$

$$E_y = \frac{m_e \omega_p^2}{4|e|} y, \quad (3.21)$$

$$B_z = -\frac{m_e \omega_p^2}{4|e|c} y, \quad (3.22)$$

where ξ is comoving coordinate defined as $\xi = x - v_p t + C$, and C is a constant chosen in a way that $\xi = 0$ in the center of the bubble. All fields were set to zero outside the bubble, without loss of generality. The set of relativistic electron motion equations with aforementioned fields on the right hand side is not analytically integrable; however, it was solved numerically with the initial conditions, which corresponds to electrons expelled from interaction region in bottom-left direction in simulation depicted in Figure 3.16.

The simulation results plotted in Figure 3.17 support the presented explanation of the injection mechanisms. For illustration, the initial position of a test electron was chosen in the front half of the ion cavity in the region, where electrons trapped by

both crossing beatwave injection or injection by laser field preacceleration are located in certain time moments. The trajectories in Figure 3.17a) show that an electron with initial momentum $p_0 = 1.8m_e c$, which corresponds to energy 1.05 MeV, can be trapped, only if the transverse component of its momentum is high enough. In the presented case, the elevation angle $\theta = \arctan p_y/p_x$ must be greater than -130° to prolong the time spent in the longitudinal accelerating field in order to gain sufficient forward momentum to get trapped.

Similarly, electron trajectories plotted in Figure 3.17b) illustrate that the initial electron momentum must be relatively low for the electron to get injected.

This explanation can be also confronted with the previous model from the literature. It is possible to estimate analytically the minimum longitudinal forward momentum which an electron must have to get trapped by using equation (4) derived for one-dimensional nonlinear plasma wave in [Esarey and Pilloff, 1995], cf. also equation (2) in [Dodd et al., 2004]. Similarly, the maximum transverse momentum of a trapped electron can be estimated from equation (5) in [Dodd et al., 2004], where also the transverse variation of the plasma wave potential is considered. We will show that, after injection, both electrons shown in Figure 3.15 fulfill the above conditions for longitudinal and transverse trapping [Esarey and Pilloff, 1995, Dodd et al., 2004]. These electrons stop oscillating in the electromagnetic field of the laser pulse approximately after 180–240 fs of the simulation time; they are then injected into the bubble and trapped.

From the aforementioned PIC simulations of the OC3P configuration, we have $\phi \approx 3.5$. By inserting this value together with other simulation parameters into equation (4) in [Esarey and Pilloff, 1995], we obtain for the minimum longitudinal momentum of an injected electron necessary for trapping in the bubble the value $p_x = 1.64 m_e c$.

For the maximum transverse momentum of a trapped electron (which has the minimum necessary longitudinal trapping momentum), we get similarly from equation(5) in [Dodd et al., 2004] the value $p_y = 5.1 m_e c$. As we can see from the PIC simulations for the particle in Figure 3.15, the longitudinal and transverse trapping conditions are fulfilled.

In conclusion of this theoretical section, the process of injection in the OC3P configuration is pre-determined by the electron dynamics in the fields of the drive and injection pulses. However, equations of electron motion are not integrable in the field of two waves which propagate in crossed directions [Patin et al., 2005]. Numerical analysis indicates that such a motion tends to be chaotic. Further, the beatwave in the OC3P configuration does not produce time averaged ponderomotive force pattern with scale length comparable to the laser field wavelength (as in the case of the

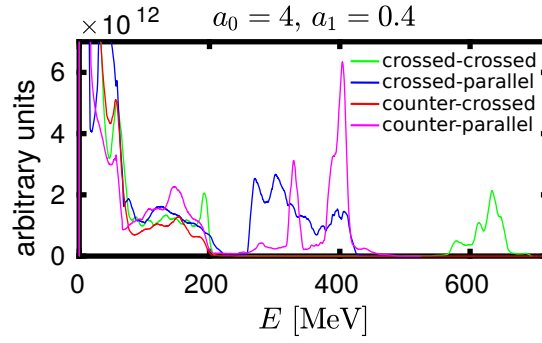


Figure 3.18: Energy distribution functions of accelerated electrons at the time of 8 ps for $I_{IP} = 0.01I_{DP}$ for four basic configurations: green curve – crossed pulses with crossed polarisations (OC3P), blue curve – crossed pulses with parallel polarizations, red curve – counter-propagating pulses with crossed polarizations, and magenta curve for counter-propagating pulses with parallel polarizations. Figure taken from [Horný et al., 2017b].

parallel polarization of the drive and injection pulses) such ponderomotive force pattern results in dephasing of the electron motion from the plasma wave oscillations [Kotaki et al., 2004, Fubiani et al., 2004, Lehe et al., 2013] and subsequent electron injection.

Comparison with similar optical injection mechanisms

The configuration of the drive and injection pulse polarizations significantly affects the energy spectrum of accelerated electrons. Figure 3.18 compares energy distribution functions of accelerated electrons for all four basic configurations of orthogonally colliding and counter-propagating laser pulses. The comparison is performed for $I_{IP} = 0.01I_{DP}$ at the time of 8 ps.

There is an observation which must be addressed. The peak energy of the optically injected electrons seems to depend on the configuration of the drive and injection pulse. For counter-crossed case, no injection into the first bucket occurs for $I_{IP} = 0.01I_{DP}$ and energetic electrons shown in Figure 3.18 are accelerated in following buckets. The energy of the electron bunch accelerated in the first bucket is higher for crossed-crossed case (OC3P) than for the counter-parallel case and crossed-parallel case. The reason is that the electrons in the OC3P case are trapped in the most rear part of the first bucket where the longitudinal accelerating field is the highest; whereas in other cases they are trapped in the whole rear half of the first ion cavity. Therefore they do not gain the energy from the plasma wave so efficiently. Relatively low energy spread in the case counter-parallel case is depreciated due to the effect of beam-loading [Katsouleas and Su, 1987].

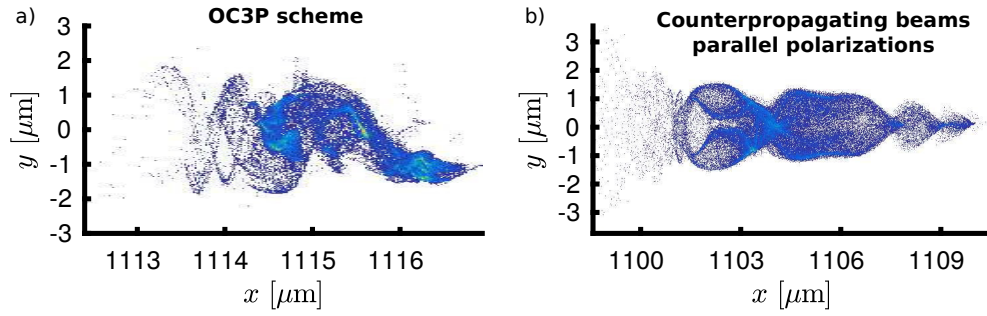


Figure 3.19: Position distributions of trapped electrons in the time of 4 ps. Figure taken from [Horný et al., 2017b].

| Time | OC3P | counter-parallel | crossed-parallel |
|------|------|------------------|------------------|
| 2 ps | 1.72 | 1.04 | 1.08 |
| 8 ps | 2.27 | 1.76 | 3.36 |

Table 3.2: Table of transverse emittance ε_y [$\pi \cdot \text{mm} \cdot \text{mrad}$] in time of 2 ps and 8 ps for considered laser pulses configurations with $I_{IP} = 0.01I_{IP}$. The counter-crossed case is not included, as there is no optically injected bunch in the first ion cavity for this set of parameters. The values for the counter-parallel configuration and crossed-parallel configurations are not far from 3D simulations by Lehe [Lehe et al., 2013] and 2D simulations by Wang [Wang et al., 2008], where lower drive pulse intensity and different plasma density are used, respectively. The emittance for the OC3P case, 1.72 $\pi \cdot \text{mm} \cdot \text{mrad}$ in the time of 1 ps, is higher than these values. Table taken from [Horný et al., 2017b].

The 2D particle-in-cell simulations reveal that the OC3P scheme with the injection intensity of $0.01I_{DP}$ produces 2.1 μm long (7.0 fs) electron bunch at 4 ps of acceleration. In comparison, the counter-propagating parallel polarization injection pulse with same intensity generated approximately 3 times longer beams. The spatial distribution of the bunch electrons at the time of 4 ps is depicted in Figure 3.19.

The quantity known as the beam emittance is the fundamental parameter of the electron beam [Buon, 1994, Lehe, 2014]. It imposes a fundamental limit on the beam size and divergence which can be reached by the beam manipulations.

The table 3.2 shows values of ε_y in times of 1 ps and 8 ps of acceleration for bunches in the crossed-crossed (OC3P case, shown in Figure 3.11) and counter-parallel cases, and also for the crossed-parallel configuration for the same parameters ($I_{IP} = 0.01I_{DP}$).

In spite of this larger emittance value, the electron bunch is short even in the time of

8 ps after injection, with the mean energy of about 630 MeV and a low energy spread about 20 MeV (Figure 3.11).

■ Dependence on other characteristics

To understand better the influence of initial parameters on the bunch characteristics in the simulations, we scanned for various intensities $I_{IP} = 0.01I_{DP}$, $0.1I_{DP}$ and I_{DP} , the effect of

1. the time delay of the IP arrival by ± 10 fs,
2. the waist size of the IP
3. the case with parallel polarizations of both beams.

The results after 1 ps of the simulation when injection process is finished and acceleration phase is stabilized are summarized below in Tables 3.3 – 3.6. All the simulations were done for same basic physical parameters as in the previous section, i.e. the plasma density $n_e = 5 \times 10^{18} \text{ cm}^{-3}$, the laser wavelength $0.8 \text{ }\mu\text{m}$, waist size $w_0 = 9.5 \text{ }\mu\text{m}$, both pulse durations of 25 fs, OC3P scheme.

We can see in Table 3.3 that the maximum energy in the bunch E weakly depends on the time of the IP arrival. On the other hand, the maximum spectral density peak N (in arbitrary, but mutually comparable units) is the largest for low IP intensity when the IP arrives *in time*. For the low intensity of the IP, the width of the energy spectrum of the bunch electrons is small, independently on the time of the IP arrival.

Table 3.4 shows that for low IP intensities, for which the width of the electron energy spectrum is smallest, the same size of the DP and IP waist seems to be an optimum choice. However, it seems that the lower IP waist size provides better results than the opposite case which is non-ideal from the point of the practical implementation.

Table 3.5 shows that for low IP intensities, for which the width of the electron energy spectrum is the smallest, the peak electron energy E for the perpendicular polarization

| I_{IP}/I_{DP} | E (MeV) | | | N (a.u.) | | | ΔE (MeV) | | |
|-------------------------------|-----------|------|------|------------|-----|-----|------------------|------|------|
| | 0.01 | 0.1 | 1 | 0.01 | 0.1 | 1 | 0.01 | 0.1 | 1 |
| $\Delta\tau = 10 \text{ fs}$ | 90.6 | 76.9 | 68.1 | 270 | 160 | 370 | 2.5 | 5 | 5 |
| $\Delta\tau = 0$ | 90.6 | 76.9 | 76.2 | 320 | 180 | 230 | 2.5 | 7.5 | 6.87 |
| $\Delta\tau = -10 \text{ fs}$ | 90 | 89.3 | 77.5 | 230 | 180 | 180 | 2.5 | 12.5 | 11.9 |

Table 3.3: Dependence of the electron bunch characteristics on the time delay of the injection pulse. Table taken from [Horný et al., 2017c].

| | E (MeV) | | | N (a.u.) | | | ΔE (MeV) | | |
|----------------------------|-----------|------|------|------------|-----|-----|------------------|------|------|
| I_{IP}/I_{DP} | 0.01 | 0.1 | 1 | 0.01 | 0.1 | 1 | 0.01 | 0.1 | 1 |
| $w_{IP} = 4 \mu\text{m}$ | – | 91.9 | 62.5 | – | 460 | 85 | – | 0.93 | 12.5 |
| $w_{IP} = 7 \mu\text{m}$ | 93.7 | 93.7 | 81.2 | 180 | 460 | 170 | 6.25 | 7.25 | 11.2 |
| $w_{IP} = 9.5 \mu\text{m}$ | 90.6 | 76.9 | 76.2 | 320 | 180 | 230 | 2.5 | 7.5 | 6.87 |
| $w_{IP} = 12 \mu\text{m}$ | 81.2 | 78.1 | 81.2 | 110 | 130 | 190 | 21.2 | 15 | 25 |

Table 3.4: Dependence of the electron bunch characteristics on injection pulse waist size. Table taken from [Horný et al., 2017c].

| | E (MeV) | | | N (a.u.) | | | ΔE (MeV) | | |
|---------------------------|-----------|------|------|------------|-----|-----|------------------|------|------|
| I_{IP}/I_{DP} | 0.01 | 0.1 | 1 | 0.01 | 0.1 | 1 | 0.01 | 0.1 | 1 |
| \perp polarizations | 90.6 | 76.9 | 76.2 | 320 | 180 | 230 | 2.5 | 7.5 | 6.87 |
| \parallel polarizations | 71.9 | 62.5 | 71.9 | 450 | 450 | 550 | 2.5 | 6.25 | 3.12 |

Table 3.5: Dependence of the electron bunch characteristics on mutual polarizations of the main and injection pulse. Table taken from [Horný et al., 2017c].

| n_e [10^{18} cm^{-3}] | 1.75 | 2 | 3 | 4 | 5 | 6 | 7 |
|-------------------------------------|------|-----|----|----|----|-----|-----|
| Q [pC] | 0.8 | 8 | 14 | 27 | 44 | 56 | 98 |
| l [μm] | 1.5 | 1.5 | 2 | 3 | 3 | 3.5 | 3.5 |
| E [MeV] | 47 | 87 | 81 | 75 | 66 | 50 | 47 |
| ΔE [MeV] | 25 | 25 | 7 | 6 | 6 | 3.8 | 31 |

Table 3.6: Dependencies of the injected charge, bunch length, peak energy and energy width on the electron density for the parameters: $a_0 = 4$, $a_1 = 0.4$, $w_{0,DP} = w_{0,IP} = 9.5 \mu\text{m}$. Table taken from [Horný et al., 2017c].

is higher than for the parallel polarization, while the opposite is true for N .

Finally, also the study of the dependencies of the injected charge, bunch length, peak energy and energy width on the electron density was performed; it is presented in Table 3.6. The electron charge was estimated supposing cylindrical symmetry of the accelerated bunch. It can be seen that the maximum electron energy drops with the increase in the electron density. On the other hand, the length of the electron bunch and the injected charge grows with the electron density. There is an optimum value of electron density regarding the monoenergeticity. For the electron density of $6 \times 10^{18} \text{ cm}^{-3}$, the relative energy spread $\Delta E/E$ is lower than 8%. Nevertheless, the suggested mechanism of the orthogonally crossed pulses with perpendicular polarizations seems to be usable in the wide range of laser and plasma parameters.

3.5 Injection by collinear pulses

Previous scheme of crossed pulses offers a solution to the potential issue of a certain injection pulse degradation due to its long propagation in plasma before the collision with the plasma wave drive pulse. On the other hand, the temporal and spatial synchronization of both ultrashort pulses is still quite challenging from experimental point of view. Alternative optical injection scheme by preceding injection pulse which can be more easy to implement is proposed too. It predicts the generation of high charge ultrashort electron bunches. This scheme was introduced at an international conference [Horný and Krůs, 2017] and is currently in the review process in a specialized journal [Horný et al., 2018a]. Within this section, the main results of this research will be presented. Nonetheless, let us review first the alternative schemes with two collinear pulses.

3.5.1 Optically induced ionization injection

In this approach, a more intense laser pulse is delayed to provide injection by optically induced ionization of the heavier atom inner shell electrons of the dopant gas. Such a scheme is intended to be employed in the linear or moderately non-linear LWFA regimes [Bourgeois et al., 2013, Xu et al., 2014]. Both simulation works report few pC bunches with low energy spread and emittance due to localized ionization injection by tightly focused injection pulse. The principle of ionization injection will be discussed in more details in Section 3.6.

3.5.2 Injection by collinear pulse with different focusing

The production of monoenergetic electron beams by two copropagating ultrashort laser pulses was reported in [Thomas et al., 2008]. In this case, the second pulse is intended rather to guide the plasma wave drive pulse. It was shown though, that the presence of this guide pulse and its proper timing can significantly decrease the self-injection threshold. Thus, also this scheme can be thought of as a case of the optical injection. The core idea of this scheme is that a high-amplitude plasma wave is generated and sustained for longer time than what is possible with either of the laser pulses individually, due to plasma wave-guiding of the driver by the guiding pulse.

Such a technique enabled the production of few pC electron bunches. These bunches were quasimonoenergetic; their energy was $\approx (15 \pm 1)$ MeV; significant dark current depreciates the spectra though. These results were achieved with relatively modest laser and plasma parameters: 2×300 mJ, $\tau_{0,1} = 40$ fs, $w_0 = 5$ μm , $w_1 = 25$ μm , $a_0 = 3.0$,

$a_1 = 0.6$, $n_e = 1.0 \times 10^{19} \text{ cm}^{-3}$. The best spectra were observed when both pulses overlapped perfectly.

Another approach uses very sharp ($< 10 \text{ }\mu\text{m}$) vacuum-plasma transition [Hu et al., 2016]. The tightly focused injection pulse is delayed by the distance of the bubble length. It enters the plasma at the moment when the rear edge bubble is sealed. Thus, a part of electrons from this bubble rear edge receives a kick by the injection pulse; these electrons are trapped in the bubble. Injection pulse diffracts very early due to its tiny spot size; whereas the drive pulse with the spot size close to the matched condition for self-guiding (2.56) and with the intensity under the self-injection condition propagates for a long distance in the low-density plasma.

It is challenging to produce such a sharp density transition in experiments using state-of-art technology though. Few pC, GeV electron beams with energy spread under 0.5 % and sub- μm normalized transverse emittance are predicted employing the phase-space rotation with the rephasing technique [Hu et al., 2016]. Laser and plasma parameters were the following: $\tau_0 = 23 \text{ fs}$, $\tau_1 = 6 \text{ fs}$, $w_0 = 24.8 \text{ }\mu\text{m}$, $w_1 = 3 \text{ }\mu\text{m}$, $a_0 = 3.0$, $a_1 = 4.0$, $n_e = 1.0 \times 10^{18} \text{ cm}^{-3}$.

3.5.3 Collinear multi-pulse scheme

The use of multiple collinear laser pulses following each other may lead to the significant resonant amplification of the generated plasma wave [Berezhiani and Murusidze, 1992, Umstadter et al., 1994]. To a certain extent, it is comparable with the self-modulated LWFA [Joshi et al., 1981, Esarey et al., 1994] with a laser pulse longer than the plasma wavelength λ_p . The resonant accelerator [Umstadter et al., 1994] uses optimized train of short pulses to excite the plasma wave; the spacing between pulses and the width of each pulse is independently controlled.

3.5.4 Optical injection by preceding pulse

The novel optical injection scheme with a weaker injection pulse preceding the accelerating plasma wave driving pulse is proposed by the author. Its crucial advantage is relatively easy implementation in comparison with all aforementioned optical injection schemes. The incident laser can be divided into two parts by combination of pellicle beamsplitter and standard flat mirror; the delay between preceding injection pulse and following drive pulse is easily controllable by the distance between these mirrors. The ratio of the intensities of both laser pulses is determined by a pellicle splitting ratio. The waist size of both pulses in our scheme is the same. The possible experimental setup is drawn in Figure 3.20.

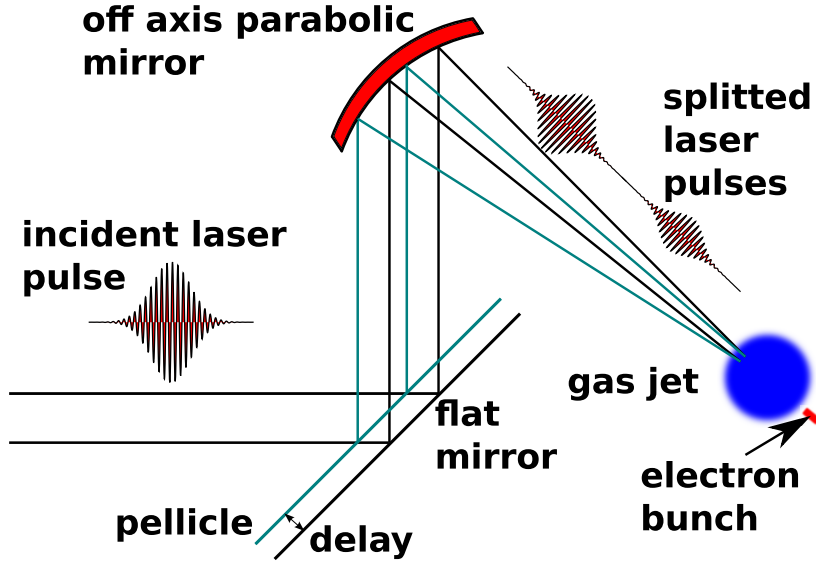


Figure 3.20: Proposed experimental configuration for the injection by the preceding pulse.

This simple configuration avoids the issues with temporal and spatial synchronization which are characteristic for other optical injection schemes. Contrary to all previously mentioned schemes with collinear pulses [Bourgeois et al., 2013, Xu et al., 2014, Thomas et al., 2008, Hu et al., 2016] where the injection is longitudinal, the presented injection process is transverse and it leads to much higher charge of accelerated electron bunches.

This injection mechanism is in a certain way inspired by standard self-injection. As it was claimed previously in Section 3.2, the collection volume for the transversely self-injected electrons in nonlinear bubble regime is a ring around laser propagation axis with the radius given by equation (3.9).

The intensity of the injection pulse is assumed to be high enough ($a_1 \gtrsim 1.8$) to generate its own bubble. The longitudinal radii of drive and injection bubbles are [Benedetti et al., 2013] (in the case when pulse duration perfectly matches with plasma oscillations, which is the case in the presented example configuration)

$$R_{\parallel,0,1} = k_p^{-1}(2.9 + 0.305a_{0,1}). \quad (3.23)$$

Drive pulse delay is chosen in such a way that the collection ring for self-injection is localized just in front of the electron bunch accelerating bubble and coincides with the electron sheath of the first bubble, i.e. under the assumption of a spherical bubble:

$$\Delta t = \frac{1}{c}(\sqrt{R_{\parallel,0}^2 - r_0^2} + \sqrt{R_{\parallel,1}^2 - r_0^2}) + \frac{\tau}{2}, \quad (3.24)$$

or, if the bubble is considered as an ellipse:

$$\Delta t = \frac{1}{c} \left(R_{\parallel,0} \sqrt{1 - \frac{r_0^2}{R_{\perp,0}^2}} + R_{\parallel,1} \sqrt{1 - \frac{r_0^2}{R_{\perp,1}^2}} \right) + \frac{\tau}{2}. \quad (3.25)$$

However, there is no estimate of transverse radii of a bubble yet. Such configuration increases the electron density in a region where electrons could be potentially injected to bubble dragged by the main pulse.

The injection can be induced by the bubble expansion, as it was shown in the Section 3.2 or in the concept of optical transverse injection [Lehe et al., 2013]. Such expansions can be understood as a Langmuir wave-breaking. Within our scheme, bubble expansion can occur due to stochastic nature of the bubble dynamics, but such a scheme would not be stable.

Therefore, the wave breaking is achieved in a controlled manner at a density up-ramp at a vacuum plasma transition, similarly as by the up-ramp injection by a single pulse in much higher plasma densities [Li et al., 2013]. Such a localized injection leads to quasimononenergetic electron spectra and potentially to a good reproducibility.

The injection pulse also modulates the electron density in the location where the main pulse propagates. In some sense, presented configuration may be thought of as if the injection pulse generates a plasma waveguide for the drive pulse [Borisov et al., 1994, Chen et al., 1998b].

Numerical PIC simulations

The injection process was studied by means of 3D particle-in-cell (PIC) simulations using the code EPOCH [Arber et al., 2015]. The following parameters were chosen to demonstrate the scheme: laser wavelength $\lambda = 0.8 \mu\text{m}$, waist size $w_0 = 9.5 \mu\text{m}$, pulse length $\tau = 25 \text{ fs}$, drive and injection laser pulses strength parameters $a_0 = 4$ and $a_1 = 2.5$. The mutual delay between pulses was 65 fs which corresponds to the plasma period; both pulses are linearly polarized. A uniform electron gas with density $3 \times 10^{18} \text{ cm}^{-3}$ and immobile ions were assumed (they were not simulated). The initial demonstration used 20 μm long linear front plasma density ramp. Simulation box dimensions were 85 $\mu\text{m} \times 36 \mu\text{m} \times 36 \mu\text{m}$ with $25 \times 4 \times 4$ cells per wavelength and 2 particles per cell.

The snapshots of the injection process from the 3D PIC simulation are shown in Figure 3.21. The injected electrons lying initially at the ring around the propagation axis located at the transition between the end of the density ramp and the homogeneous plasma are at first disturbed by the injection pulse and after that trapped in the bubble dragged by the main pulse. The nature of this injection process is transverse. The incline of the

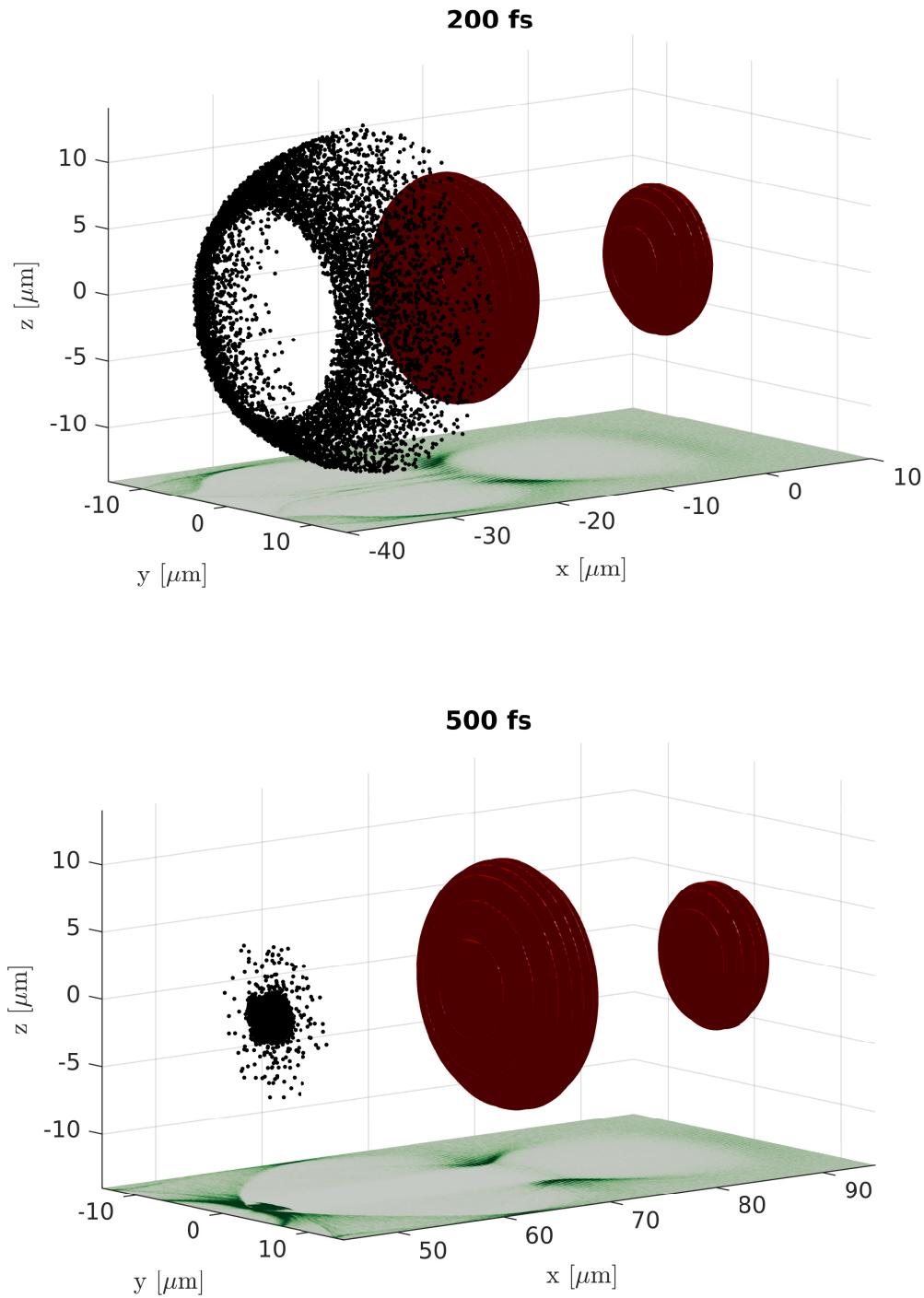


Figure 3.21: Visualization of the injection process from 3D PIC simulation. Isosurfaces of laser pulse electric field are displayed in brown. Trapped electrons (black dots, selection) are initially at the ring around axis. The electron density in the plane $z = 0$ is shown at the bottom of both boxes.

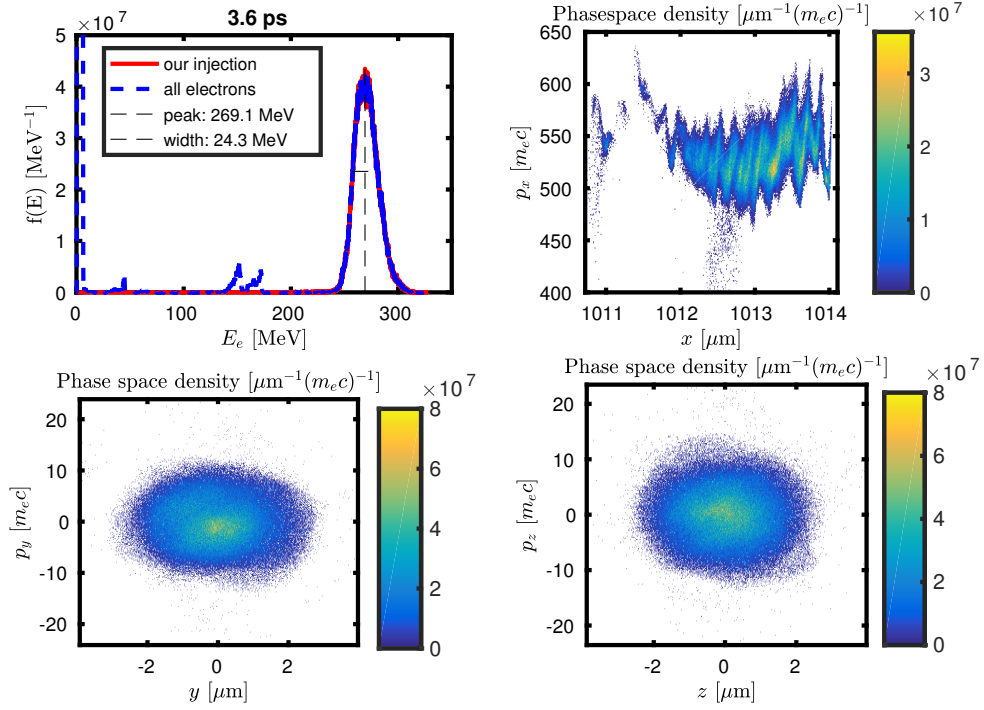


Figure 3.22: Electron spectrum and phase-space densities of the accelerated electron bunch after 3.6 ps of acceleration.

density ramp tunes the injected charge; the shorter density ramp leads to the higher charges. This behaviour was studied for feasible ramp lengths of 20–100 μm .

Energy, relative energy spread, charge, and transverse emittance of the trapped electron bunch in the simulation are 269 MeV, 9 %, 188 pC, and $1.63 \pi\text{-mm-mrad}$, respectively, after 3.6 ps of simulation. Optically injected electrons are well separated from the dark current; energy spectrum is depicted in Figure 3.22. The longitudinal and transverse phase-space plots are also shown there. The bunch length is 1.8 μm (FWHM of bunch density along x -axis). Energy spread could be reduced by intricate density tailoring techniques in a further stage of acceleration, similarly as in [Hu et al., 2016]. The rotation in the electron bunch phase space is induced there by the continuous decrease of the plasma density in the leading plasma channel.

Additional 3D simulations were performed in order to determine the dependence of the accelerated electron bunch parameters on the density ramp length and on the injection pulse intensity. The results were compared at the time of 2 ps of simulation when the injection process is already finished and acceleration phase is stabilized. It was observed, that for given parameters, the ramp length of 20 μm is the optimal from the viewpoint of the highest injected charge Q , while energy spread ΔE (FWHM of energy peak) is kept as low as 9%. Such a ramp length is also feasible from the experimental point of

| a_0 | a_1 | l_r [μm] | E [MeV] | ΔE [MeV] | Q [pC] |
|-------|-------|-------------------------|-----------|------------------|----------|
| 4 | 2.5 | 10 | 163 | 12 | 182 |
| 4 | 2.5 | 20 | 160 | 14 | 188 |
| 4 | 2.5 | 30 | 162 | 20 | 167 |
| 4 | 2.5 | 50 | 175 | 22 | 128 |
| 4 | 2.5 | 100 | 154 | 50 | 75 |

Table 3.7: Dependence of electron bunch parameters on density ramp length at time 2 ps of simulation. l_r is initial linear ramp length, E is energy of a peak of electron spectra, ΔE is its width, Q is injected charge.

| a_0 | a_1 | l_r [μm] | E [MeV] | ΔE [MeV] | Q [pC] |
|-------|-------|-------------------------|-----------|------------------|----------|
| 4 | 1 | 30 | 227 | 25 | 39 |
| 4 | 2 | 30 | 218 | 23 | 122 |
| 4 | 2.5 | 30 | 162 | 20 | 167 |
| 4 | 3 | 30 | 119 | 37 | 127 |

Table 3.8: Dependence of electron bunch parameters on injection pulse intensity at time 2 ps of simulation. l_r is initial linear ramp length, E is energy of a peak of electron spectra, ΔE is its width, Q is injected charge.

| a_0 | a_1 | $\Delta\tau$ [fs] | l_r [μm] | E [MeV] | ΔE [MeV] | Q [pC] |
|-------|-------|-------------------|-------------------------|-----------|------------------|------------|
| 4 | 2.5 | 60 | 30 | 130 | 25 | 103 |
| 4 | 2.5 | 65 | 30 | 162 | 20 | 167 |
| 4 | 2.5 | 70 | 30 | <i>97</i> | <i>26</i> | <i>140</i> |
| 4 | 2.5 | 75 | 30 | <i>97</i> | <i>9</i> | <i>81</i> |

Table 3.9: Dependence of electron bunch parameters at time 2 ps of simulation on mutual delay between both pulses $\Delta\tau$. l_r is initial linear ramp length, E is energy of a peak of electron spectra, ΔE is its width, Q is injected charge. Values in italic are at the time of 1 ps due to later collapse of acceleration, see Figure 3.23. When $\Delta\tau$ was set to 55 fs, injection occurred stochastically around the time of 1.8 ps.

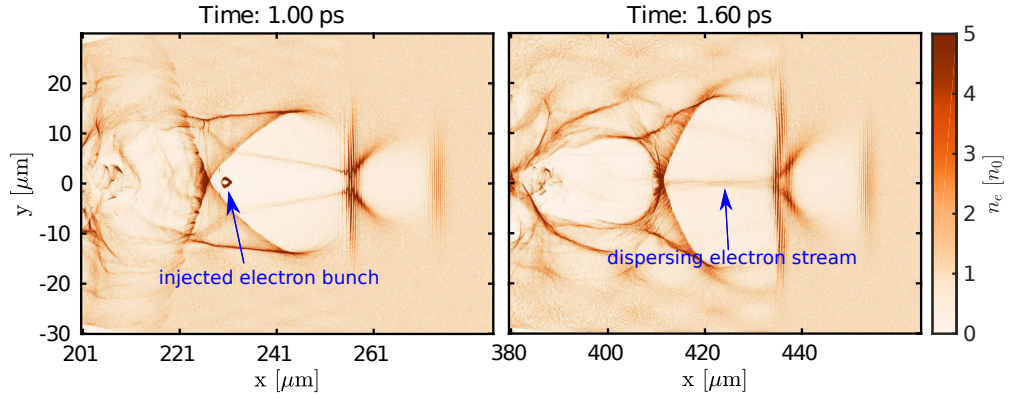


Figure 3.23: Disruption of the trapped electron bunch by the electron stream caused by the contact of the rear part of the first bubble and the drive pulse. Time delay between pulses was 75 fs.

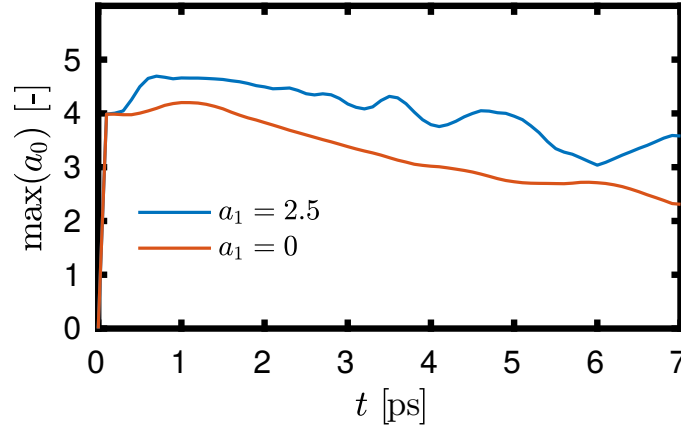


Figure 3.24: Presence of the injection pulse slows down the loss of the drive pulse intensity.

view. The dependence is presented in Table 3.7.

Table 3.8 illustrates that there is a wide range of injection pulse intensities which lead to high charge electron bunches. Nevertheless, the optimum parameters are achieved when injection pulse intensity is high enough to generate its own wake, i.e. $a_1 \gtrsim 1.8$. However, too strong injection pulse can destroy wakefield driven by drive pulse, i.e. in the optimal case $(a_1/a_0)^2 < 0.5$. Our injection mechanism was not observed for $a_1 \gtrsim 3.5$; self-injection occurred in the first bubble. However, the injected bunch is soon scattered by the main pulse located at the rear side of the first bubble.

Presented scheme is very sensitive to the time delay between pulses. According to equation (3.24), the optimum delay between both pulses is 67 fs for our demonstration example. Table 3.9 shows that the parameters of accelerated electron bunches are optimal around this predicted value.

However, if the delay between pulses is too long, trapped electron bunch may be dispersed by an electron stream generated due to the contact between the most rear part of the injection pulse bubble and the drive pulse. Such a phenomenon is displayed in Figure 3.23 for the time delay between both pulses of 75 fs. At the time of 1 ps, a high-quality electron bunch is formed. Nevertheless, the electron streams, which eventually destroy the bunch, are already apparent.

This acceleration scheme has yet another beneficial side effects. As it is shown in Figure 3.24 the intensity of the drive pulse decreases more slowly if the injection pulse is present. The cause of this effect is that the drive pulse does not propagate in a homogeneous plasma anymore, but rather in the channel with the density profile perturbed by the injection pulse. Whereas the central part of the drive pulse propagates in the very low-density plasma located in the rear part of the bubble generated by the injection pulse; the edges are cut by the electron streams of which the front bubble is comprised. This effect can be well seen by comparing of the pulse position and the density cut shown in Figure 3.21. As a consequence, the beam diffraction is suppressed.

3.6 Ionization injection

In previous injection schemes, the chemical composition of the target does not play a significant role. Typically, the low- Z targets are used, because of their relatively low ionization energies. For example, ionization energies of helium are 24.6 eV and 54.4 eV [NIST, 2018]; therefore, the plasma is immediately fully ionized in the whole interaction region due to optical field ionization.

Another convenient mechanism to trap the electrons in the wake wave is an ionization injection [Pak et al., 2010]. A mixture of two gases is used, typically the dominant part of the mixture are light elements such as helium and the trace amount of the heavier elements is added (e.g. 99 % of He + 1 % of Ar as in the experiment at PALS, or 90 % of He + 10 % of N₂ in the original work [Pak et al., 2010]). The heavier elements have typically a huge gap between ionization potentials of individual atomic levels, especially for the inner shells and when the shells are fully ionized. The ionization energies of selected atoms are shown in Table 3.10. For example, whereas the ionization energy of the electrons from the L -shell of the nitrogen atom is comparable with the helium (up to 97.9 eV), and typically all these electrons are released from the atoms in the whole interaction region, the ionization of the inner K -shell electron requires an order of magnitude higher energy (552 eV and 667 eV) [NIST, 2018].

Electrons are injected into the wakefield due to the tunnel ionization of the inner

| | | | | | | | | | |
|-----|--------|--------|-------|-------|-------|-------|--------|-------|-------|
| Z | 1 | 2 | 3 | 4 | 5 | 6 | 7 | 8 | 9 |
| | 10 | 11 | 12 | 13 | 14 | 15 | 16 | 17 | 18 |
| H | 13.60 | | | | | | | | |
| He | 24.59 | 54.42 | | | | | | | |
| Li | 5.392 | 75.64 | 122.5 | | | | | | |
| N | 14.532 | 29.602 | 47.45 | 77.47 | 97.90 | 552.1 | 667.01 | | |
| O | 13.62 | 35.12 | 54.94 | 77.41 | 113.9 | 138.1 | 739.3 | 871.4 | |
| Ar | 15.76 | 27.63 | 40.74 | 59.81 | 75.02 | 91.01 | 124.3 | 143.5 | 422.5 |
| | 478.7 | 539.0 | 618.3 | 686.1 | 755.7 | 854.8 | 918.0 | 4120 | 4426 |

Table 3.10: Ionization energies of selected atoms in eV [NIST, 2018].

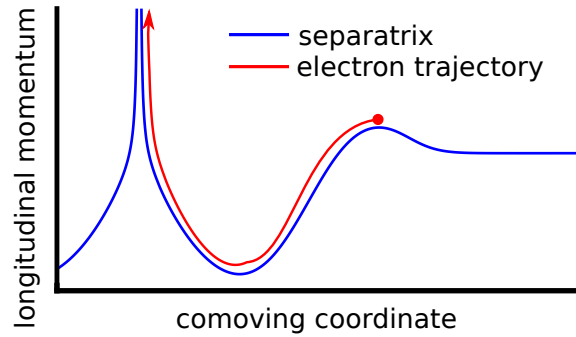


Figure 3.25: Electron motion in the phase space illustrates the principle of the ionization injection. The red point illustrates the place where the trapped electron is born.

K -shell electrons which occurs only in the region of very high intensity, i.e. close to the peak intensity. Some of them are born with momentum already above the separatrix and they are trapped, as it is schematically shown in Figure 3.25. Therefore, the ionization process is well spatially and temporally localized (in the case of lower intensity); it may result in short quasimonoenergetic electron beams generation with the proper alignment.

The power of the laser pulse is kept under one third of the critical power (2.59) to suppress the self-injection when using this scheme. Therefore, such a scheme is suitable even for low power laser systems ($\lesssim 10$ TW).

The first experimental result with ionization injection employed was presented in [McGuffey et al., 2010]. They used neutral helium gas mixed with 1-5% additives of various high- Z gases. Laser parameters were sufficiently high to observe self-injection in the bubble regime. Nevertheless, an increase in the order of magnitude of the electron bunch charge was observed in comparison with pure helium at the same electron density.

The theory of ionization injection was introduced in [Chen et al., 2012a]. An important conclusion is that the minimum energy spread of accelerated electrons is determined by

the spread in initial ionized phases of the electrons in the wakefield due to the tunneling ionization process within the laser pulse. Additionally, the trapping condition was derived. From the perspective of Section 3.1, it can be written as

$$1 + \psi_{min} - \psi(\xi_b) \leq \frac{[1 + a^2(\xi_b)]^{1/2}}{\gamma_p}, \quad (3.26)$$

where ξ_b is the location where the electron was born. Interestingly, it was found that this injection mechanism requires $a_0 \gtrsim 1.7$ assuming the nitrogen as an additive in the helium.

A similar idea was already suggested earlier for plasma wakes, which can be generated by the electron bunch previously accelerated in the standard radiofrequency accelerator propagating through the plasma. The ionization induced injection into these wakes was observed in the plasma comprised of the lithium vapour and a helium gas [Oz et al., 2007]. Contrary to the ionization injection in LWFA, the helium atoms played a role of the element with the higher ionization potential which could be eventually trapped. Some electrons gain up to 7.6 GeV in a 30.5 cm plasma.

■ 3.6.1 Experiment at PALS

An experimental campaign was run at Ti:sapphire laser system located at PALS facility in Prague in 2016 [Boháček et al., 2018]. Its purpose was to stabilize the properties of accelerated electron bunches. It was achieved by slight modification of the ionization injection technique. The dry air, i.e. a mixture of nitrogen and oxygen without the presence of other gases) was used as a target. The experiment was carried out with only few-TW of laser power. Thus, the high density plasma was used with the intention to provide the relativistic self-focusing. Such an approach enables to achieve the necessarily high laser intensity and sustain it sufficiently long time. The advantage of the dry air in comparison with the standard mixture of low- Z and high- Z gases is purely technical, the high plasma densities can be reached without the necessity of usage of high backing pressure (it would require almost four times higher backing pressure to reach the same density if helium target was used).

The experimental setup was following: 50 fs, 0.6 J, 800 nm laser pulse interacted with the dry air stream produced from the supersonic de Laval nozzle. The electron density measured by Mach-Zehnder interferometry was rather high in the focal spot; it varied around $5 \times 10^{19} \text{ cm}^{-3}$. The laser beam was focused to the spot of the size $(14.4 \pm 2.1) \mu\text{m}$ in horizontal and $(10.1 \pm 1.2) \mu\text{m}$ in vertical direction. The energy delivered to the target in the region where $I > I_{max}/e^2$ was $(366 \pm 30) \text{ mJ}$.

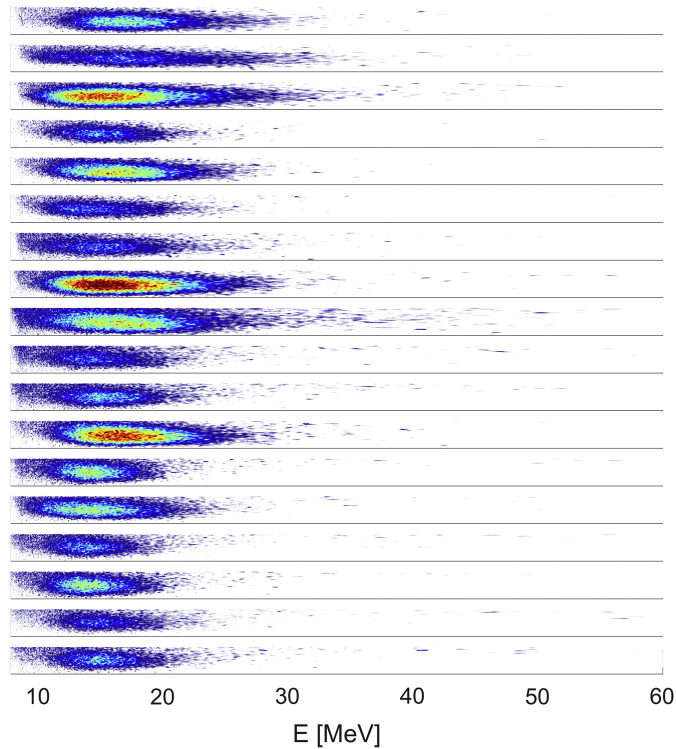


Figure 3.26: Consecutive electron spectra corrected on the beam pointing and obtained using the air gas jet target showing high stability in the beam mean energy $\bar{E} = (17.4 \pm 1.1)$ MeV. Figure from [Boháček et al., 2018].

Highly stable electron bunches with the mean energy of (17.4 ± 1.1) MeV and the FWHM energy spread of (13.5 ± 1.5) MeV were measured (see Figure 3.26). The charge of the accelerated bunches was 3.1 pC with the relative fluctuation of 21 %.

The experimental results were supported by a 3D particle-in-cell (PIC) simulation that was performed using the EPOCH code [Arber et al., 2015]. The field ionization according to ADK model [Ammosov et al., 1986] was employed. The simulation started with a neutral gas comprised of nitrogen and oxygen atoms as constituents of synthetic air with their respective densities $n_N = 5.6 \times 10^{18} \text{ cm}^{-3}$ and $n_O = 1.2 \times 10^{18} \text{ cm}^{-3}$, and the measured experimental parameters described above were used in the simulation.

Therefore, the atoms in the simulation were ionized by the 50 fs laser pulse containing an energy of 360 mJ in the focal spot with the waist size of 6 μm , resulting in the generation of a plasma with the off-axis electron density of approximately $3.5 \times 10^{19} \text{ cm}^{-3}$. The defined number of cells per wavelength was 25 in longitudinal and 3 in the transversal directions with respect to the laser pulse propagation direction. Each cell contained one macroparticle of oxygen and one macroparticle of nitrogen, which after ionization generated on average 11 electron macroparticles per cell. The simulation indicates that a

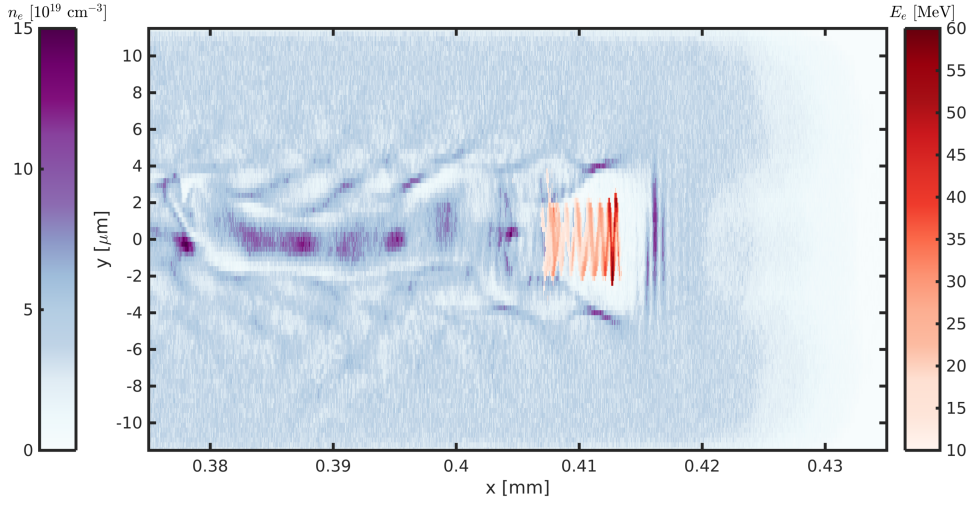


Figure 3.27: Electron density (blue) and electron energy (orange) plot from 3D PIC simulation.

formation of non-linear wake wave occurs (shown in Figure 3.27), in which the trapped electrons are accelerated. Firstly, the laser pulse undergoes the relativistic self-focusing over a Rayleigh length in plasma and the minimum waist size of the laser pulse reached only $3 \mu\text{m}$. This corresponds to the peak laser strength parameter of approximately 3.4, which is enough to completely ionize both nitrogen and oxygen atoms as intended.

The PIC simulation suggests that continuous spectrum of accelerated electrons up to 60 MeV is generated. The most energetic electrons are located at the front of the injected bunch. The accelerating structure differs from a standard bubble, it is relatively long and it develops dynamically during the acceleration process. The regions where electrons are accelerated and decelerated follow each other within this structure. As the electrons traverse between these regions, they repetitively gain and lose energy. Thus, they are not accelerated to the higher energies than $\lesssim 20$ MeV in the most cases. After approximately 0.6 mm of the propagation through the target, the laser pulse and also the accelerating structure decay due to the pump depletion. Nevertheless, the accelerated electrons advance further through the gas/plasma without significant deceleration.

Based on these observations, it can be concluded that the PIC simulation captures the main features of this acceleration mechanism. Within this scheme, the injection process is continuous, thus the typical requirement on the low energy spread, emittance or the short length is omitted. Nevertheless, the low demands on laser system and the experimental ease makes this scheme attractive for possible applications, among other for betatron radiation generation.

3.7 State-of-the-art of laser wakefield accelerators

As it was explained in this and in the previous chapters, laser wakefield acceleration of electrons is a dynamically evolving branch of research. This section intends to summarize both experimental results and simulation findings achieved for the time being. The list of the important publications, the respective demands on the laser pulse, and the properties of accelerated electron bunches are shown in Table 3.11. Let us stress that the table is not a complete overview of the examined or proposed injection schemes.

Also, the data in the table may not be fully accurate and comparable with each another. For instance, the total energy in the pulse was often estimated using equation (2.16), assuming the Gaussian pulse profile in both temporal and spatial domain. However, the real shapes of pulses used in experiments may be quite irregular. The irregular shape of the focus presented in the experimental papers was replaced by the average value. The pulse lengths are presented using FWHM of power.

Additionally, a significant part of the energy may be dissipated due to the optical aberrations, pre-pulses and other effects which are difficult to avoid. In general, the demanded energy should be to some degree higher than what is shown in the table for both experiments and simulations.

On the other hand, the energies of accelerated electrons are often underestimated for simulation results, because only injection and early acceleration phases were simulated. The energy spread is given as the FWHM of the high energy peak.

It can be stated that there are two basic paths in the LWFA research. The first one is focused on the generation of the most energetic electrons. The currently record value on this path was achieved by the group from the Lawrence Berkeley National Laboratory in 2014; the electron bunch with the charge of 6 pC was accelerated up to 4.2 GeV [Leemans et al., 2014]. This direction will be further developed at the PW-class laser systems which are built around the world. The acceleration up to such a high energy requires cm-scale acceleration distances and low plasma densities. Both these requirements suppress the effect of laser self-guiding significantly. Thus, the external guiding of the laser pulse is necessary. Typically, the channel created by e.g. the capillary discharge is intended to be used for that reason.

The alternative path, which is also developed in this work, focuses on optimization other properties of the generated electron bunches as their energy spread, emittance, bunch length, charge, and the stability and reproducibility of these parameters overall. Its motivation is to provide the usable source of accelerated electrons for the practical applications and as the injector stage for PW systems. Hence, the laser pulse parameters

which can be achieved with sub-100-TW-class laser systems are chosen. Such systems are often called table-top systems, because they can almost fit on one (large) optical table. Also, such systems are already available commercially and their cost will be soon feasible for the industrial companies, hospitals, universities, or similar institutions.

A lot of attention is paid to minimizing of the electron bunch emittance; it is required for the construction of the compact X-ray free electron laser, a source of coherent X-rays. Recently, the generation of electron bunches with the emittance lower than $1 \pi \cdot \text{mm} \cdot \text{mrad}$ was reported [Barber et al., 2017]. Other works focus on the reduction of the energy spread, shortening of the bunch, or the increase of the bunch charge. All these efforts are beneficial for the potential medical or industrial applications, and for the improvement of the secondary incoherent X-ray radiation features. For example, 220 pC electron bunches with 14% energy spread were reported recently [Couperus et al., 2017].

Two new optical injection schemes presented in Sections 3.4.4 and 3.5.4 propose short high charge electron bunches with relatively low energy spread and with an acceptable magnitude of emittance simultaneously.

| Reference and injection type | | Laser pulse parameters | | | | Electron bunch parameters | | | | |
|------------------------------|-------|------------------------|-------------------|-------------|-------------------------|---------------------------|------------------|------------|---------------|---|
| | | a_0 | \mathcal{E} [J] | τ [fs] | w_0 [μm] | E_e [MeV] | $\Delta E/E$ [%] | l/c [fs] | Q [pC] | ε_y [$\pi \cdot \text{mm} \cdot \text{mrad}$] |
| [Plateau et al., 2012] | 3.2 | 1 | 1.3 | 56 | 10.2 | 466 | 2.8 | ? | 0.4 | 0.1 |
| [Kneip et al., 2012] | 3.2 | 3 | 2.2 | 32 | 9 | 230 | large | large | 130 \pm 100 | 0.5 |
| [Leemans et al., 2014] | 3.2 | 1.66 | 16 | 40 | 52 | 4 200 | 14 | ? | 6 | ? |
| [Lundh et al., 2011] | 3.4.2 | 1.3+0.26 | 1.1 | 30 | 16.2 | 1 000 | 12 | 1.6? | 15 | ? |
| [Swanson et al., 2017] | 3.3 | 1.4 | 1.8 | 47 | 15.8 | 188 | 6.9 | ? | 5 | ? |
| [Barber et al., 2017] | 3.3 | 1.5 | 1.8 | 45 | 22 | 57 | 16 | ? | 86 | 0.5 |
| [Couperus et al., 2017] | 3.6 | 2.6 | 2.1 | 30 | 17 | 36 | 14 | 5? | 220 | ? |
| [Boháček et al., 2018] | 3.6.1 | 1.8 | 0.6 | 50 | 11 | 17 | high | ? | 3 | ? |
| [Lu et al., 2007] | 3.2 | 4 | 6.5 | 30 | 19.5 | 1.5 | 3.8 | 10 | 300 | ? |
| [Yu et al., 2014] | 3.5.1 | 1.17+0.135 | 0.25 | 92+16 | 36+5 | 45 | 2.5 | ? | 0.1 | 0.03 |
| [Xu et al., 2014] | 3.5.1 | 1.2+0.25 | 0.1 | 18+7 | 10+0.64 | ? | small | 10 | 1.5 | 0.008 |
| [Bourgeois et al., 2013] | 3.5.1 | 1+2 | 1.24 | 30+30 | 30+8 | 370 | 2 | ? | 5 | 2 |
| [Thomas et al., 2008] | 3.5.2 | 3+0.6 | 0.5 | 40+40 | 4.3+21 | 15 | 7 | ? | few | ? |
| [Hu et al., 2016] | 3.5.2 | 3+4 | 5.5 | 27+7 | 25+3 | > 1 000 | < 1 | ? | 2 | < 1 |
| [Tooley et al., 2017] | 3.3 | 4 | 3.3 | 20 | 17 | high | ? | 9 | 180 | ? |
| [Horný et al., 2017b] | 3.4.3 | 4+0.4 | 1.3 | 25 | 9.5 | 630 | 3.8 | 7 | 80 | 2.27 |
| [Lehe et al., 2013] | 3.4.2 | 4+0.2 | 1.1 | 30 | 7.8 | 40 | 2 | 3 | 100 | 0.17 |
| [Davoine et al., 2009] | 3.4.2 | 4+0.1 | 4.1 | 30 | 15.3 | 60 | 1 | 4.8 | 50 | 2.6 |
| [Horný et al., 2018a] | 3.5.4 | 4+2.5 | 1.8 | 25 | 9.5 | 269 | 9 | 6 | 188 | 1.63 |

Table 3.11: State-of-the-art of laser wakefield accelerators. The upper part of the table is devoted to the experimental demonstrations, the bottom one to simulation results. Electron energies from the simulations might often be much higher, since only the injection phase is simulated in many cases. Pulse wavelength is 0.8 μm in all the cases, with exceptions of [Yu et al., 2014], where wavelengths of the drive and injection pulses are 5 μm and 0.4 μm , respectively, and [Xu et al., 2014], where injection pulse wavelength is 80 nm. l/c is a bunch length.

Chapter 4

X-Rays from Laser Plasmas

As seen on previous example, the interaction of the high-intensity laser pulse with plasma leads to the emission of X-rays by various physical phenomena. Within this work, the attention is paid mostly to the generation of the hard X-rays with the energy higher than few keV from the relativistic electron bunches accelerated in underdense plasmas by the LWFA mechanism. Namely, betatron radiation and the inverse Compton scattering are investigated in greater detail. Such methods are based on the wiggling of the electron trajectory connected with the emission of electromagnetic radiation. An overview of all considered sources of X-ray radiation from laser-plasma accelerators is given in the review article [Corde et al., 2013].

Within this chapter, the theory of the radiation of a moving charge will be reviewed. The new method to efficiently calculate the betatron radiation spectrum and even its spectrogram from the knowledge of the electron trajectories will be introduced and demonstrated. Angular and frequency spectra of the Thomson/Compton source will be reviewed too. A brief overview of other methods to generate X-rays by the interaction of laser pulses with matter will be presented as well.

4.1 Radiation by a moving charge

Theory of electrodynamics [Landau and Lifshitz, 1951, Jackson, 1999] states that an accelerated charged particle emits the electromagnetic radiation. The change of the direction of motion is acceleration too, even if the speed remains constant. Hence, high energy moving charge can emit high energy electromagnetic radiation (X-rays) when its motion is properly tailored.

The problem of radiation of electromagnetic waves by single charged moving particle has been firstly formulated by Liénard and Wiechert⁷, independently of each other, even

⁷Liénard-Wiechert potentials, formulated in 1898 (Alfred-Marie Liénard) and 1900 (Emil Wiechert).

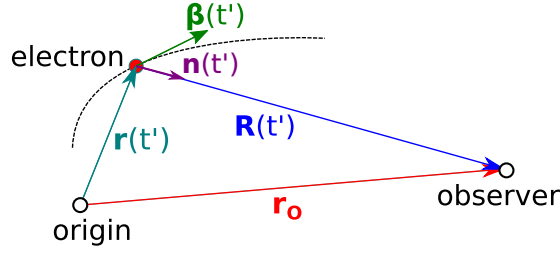


Figure 4.1: Schematic illustration of discussed quantities.

before the formulation of the special theory of relativity. In a non-relativistic regime, the radiation power depends only on the acceleration of charged particles. In relativistic regime, as the particle velocity $v = |\mathbf{v}|$ is comparable to the speed of light in vacuum c , radiation power increases rapidly and radiation is emitted especially along the direction of propagation with the angular spread $\theta = 1/\gamma$, where $\gamma = 1/\sqrt{1 - \beta^2}$ is the Lorentz factor and $\beta = \mathbf{v}/c$ is dimensionless velocity.

The properties of radiation are interconnected with the electron trajectory. Retarded potentials of a moving electron can be derived directly from Maxwell's equations and are given as [Jackson, 1999]

$$\begin{aligned}\Phi(\mathbf{r}_0, t) &= \frac{e}{4\pi\epsilon_0} \frac{1}{R(t')[1 - \mathbf{n}(t') \cdot \boldsymbol{\beta}(t')]}, \\ \mathbf{A}(\mathbf{r}_0, t) &= \frac{e}{4\pi\epsilon_0 c} \frac{\boldsymbol{\beta}(t')}{R[1 - \mathbf{n}(t') \cdot \boldsymbol{\beta}(t)]},\end{aligned}\quad (4.1)$$

where $R(t') = |\mathbf{R}| = |\mathbf{r}_0 - \mathbf{r}(t')|$ is the distance between the point of emission and observer, \mathbf{r} is the position of radiating charge, \mathbf{n} is the unit vector in direction of observation $\mathbf{R} = \mathbf{r}_0 - \mathbf{r} \approx \mathbf{r}_0$, if the observer is located in the far field. Consider that the vectors \mathbf{n} and $\boldsymbol{\beta}$ are expressed in the retarded time t' . The retarded time is the time when the field began to propagate from the point where it was emitted \mathbf{r} to the observer which is located in the point \mathbf{r}_0 . The relation between the retarded time t' and observer's time t is

$$t' = t - \frac{|\mathbf{R}|}{c}. \quad (4.2)$$

It is worth mentioning that in non-relativistic limit when $\beta \ll 1$ the potentials (4.1) take shape of classical scalar and vector potentials. The schematic drawing of the discussed quantities is depicted in Figure 4.1.

Associated electric and magnetic field can be obtained from the relations

$$\begin{aligned}\mathbf{E} &= -\nabla\Phi - \frac{\partial\mathbf{A}}{\partial t}, \\ \mathbf{B} &= \nabla \times \mathbf{A},\end{aligned}\quad (4.3)$$

where time derivative pertains to t (observing time). However, electric and magnetic fields are usually expressed in the retarded time t' . Relation between observer's and retarded time (4.2) has to be differentiated to perform a transform to the observer's time t . This gives

$$\frac{dt}{dt'} = 1 - \mathbf{n}(t') \cdot \boldsymbol{\beta}(t'). \quad (4.4)$$

Combining this relation with formulas for potentials (4.1), electromagnetic field emitted by relativistic moving charge is found

$$\begin{aligned} \mathbf{E}(\mathbf{r}_O, t) &= \frac{e}{4\pi\epsilon_0} \left\{ \frac{(1 - \boldsymbol{\beta}^2)(\mathbf{n} - \boldsymbol{\beta})}{R^2(1 - \mathbf{n} \cdot \boldsymbol{\beta})^3} + \frac{\mathbf{n} \times [(\mathbf{n} - \boldsymbol{\beta}) \times \dot{\boldsymbol{\beta}}]}{cR(1 - \boldsymbol{\beta} \cdot \mathbf{n})^3} \right\}_{ret}, \\ \mathbf{B}(\mathbf{r}_O, t) &= \frac{e}{4\pi\epsilon_0 c} \left\{ \frac{(1 - \boldsymbol{\beta}^2)[\mathbf{n} \times (\mathbf{n} - \boldsymbol{\beta})]}{R^2(1 - \mathbf{n} \cdot \boldsymbol{\beta})^3} + \frac{\mathbf{n} \times \dot{\boldsymbol{\beta}} + \mathbf{n} \times [\mathbf{n} \times (\boldsymbol{\beta} \times \dot{\boldsymbol{\beta}})]}{cR(1 - \boldsymbol{\beta} \cdot \mathbf{n})^3} \right\}_{ret} \\ &= \frac{1}{c} [\mathbf{n} \times \mathbf{E}]_{ret}. \end{aligned} \quad (4.5)$$

Indices *ret* mean that vector quantities \mathbf{r} , \mathbf{n} , $\boldsymbol{\beta}$ and $\dot{\boldsymbol{\beta}} = d\boldsymbol{\beta}/dt$ are evaluated in retarded time introduced in (4.2). Proper derivation can be found in [Jackson, 1999] and even in various courses on electrodynamics, e.g. in [Hirose, 2011]. First terms in braces are so called *velocity fields* which are independent of acceleration; second ones are *acceleration fields*, which depend linearly on $\dot{\boldsymbol{\beta}}$. Velocity fields are static Coulomb fields falling of as R^{-2} ; acceleration fields decrease with R^{-1} . Velocity fields can be omitted, as we are only interested in radiation in the far field.

Let us introduce Poynting's vector as

$$\mathbf{S} = \mathbf{E} \times \mathbf{H} = \frac{1}{\mu_0} \mathbf{E} \times \mathbf{B}, \quad (4.6)$$

because index of refraction of X-rays in underdense (with respect to the laser driver) plasmas is very close to unity. After substitution into the last relation from equations (4.5) and the use of the *bac minus cab* rule from vector calculus⁸ we obtain

$$\mathbf{S} = \frac{1}{\mu_0 c} \mathbf{E} \times (\mathbf{n} \times \mathbf{E}) = \frac{1}{\mu_0 c} \left[\mathbf{n} |\mathbf{E}|^2 - \mathbf{E} (\mathbf{E} \cdot \mathbf{n}) \right]_{ret}. \quad (4.7)$$

Let us omit the first Coulomb term in the equation for the electric field in (4.5) and substitute this relation into (4.7). The second term in (4.7) vanishes in our case and we can write the radial component of the Poynting's vector as

$$\mathbf{S} \cdot \mathbf{n} = \frac{e^2}{16\pi^2 \epsilon_0 c} \left| \frac{\mathbf{n} \times [(\mathbf{n} - \boldsymbol{\beta}) \times \dot{\boldsymbol{\beta}}]}{R(1 - \mathbf{n} \cdot \boldsymbol{\beta})^3} \right|_{ret}^2. \quad (4.8)$$

⁸The *bac minus cab* rule express the vector triple product identity [Semendyayev and Mühlig, 1997]

$$\mathbf{A} \times (\mathbf{B} \times \mathbf{C}) = \mathbf{B}(\mathbf{A} \cdot \mathbf{C}) - \mathbf{C}(\mathbf{A} \cdot \mathbf{B}).$$

Two observations can be underlined; firstly, the angular distribution of the emitted radiation is determined by the relation between observation direction \mathbf{n} and electron velocity $\boldsymbol{\beta}$ and acceleration $\dot{\boldsymbol{\beta}}$. Furthermore, the strong dependence on the factor $(1 - \mathbf{n} \cdot \boldsymbol{\beta})$ causes that only forward directed beam is produced in the ultrarelativistic case.

We can understand the quantity $[\mathbf{S} \cdot \mathbf{n}]_{ret}$ as an energy per unit area per unit time detected at an observation point at time t of radiation emitted in the retarded time t' . Based on this understanding, radiated power per unit solid angle can be defined as

$$\frac{dP}{d\Omega} = R^2(\mathbf{S} \cdot \mathbf{n}) \frac{dt}{dt'} = R^2(\mathbf{S} \cdot \mathbf{n})(1 - \boldsymbol{\beta} \cdot \mathbf{n}) \quad (4.9)$$

and from the equation (4.8) it is found that

$$\frac{dP}{d\Omega} = \frac{e^2}{16\pi^2\epsilon_0 c} \frac{|\mathbf{n} \times [(\mathbf{n} - \boldsymbol{\beta}) \times \dot{\boldsymbol{\beta}}]|^2}{(1 - \mathbf{n} \cdot \boldsymbol{\beta})^5}. \quad (4.10)$$

The energy radiated per solid angle is

$$\frac{d\mathcal{E}}{d\Omega} = \int_{-\infty}^{+\infty} \frac{dP}{d\Omega} dt \quad (4.11)$$

and after substitution of the acceleration term of electric field from (4.5) into (4.10) we can write

$$\frac{d\mathcal{E}}{d\Omega} = c\epsilon_0 \int_{-\infty}^{+\infty} |R\mathbf{E}|^2 dt. \quad (4.12)$$

Let us introduce the Fourier transform as

$$F(\omega) = \mathfrak{F}[f(t)](\omega) = \int_{-\infty}^{+\infty} f(t)e^{i\omega t} dt \quad (4.13)$$

and inverse Fourier transform as

$$f(t) = \mathfrak{F}^{-1}[F(\omega)](t) = \frac{1}{2\pi} \int_{-\infty}^{+\infty} F(\omega)e^{-i\omega t} d\omega. \quad (4.14)$$

In this case, Parseval's theorem takes the form

$$\int_{-\infty}^{+\infty} |f(t)|^2 dt = \frac{1}{2\pi} \int_{-\infty}^{+\infty} |F(\omega)|^2 d\omega \quad (4.15)$$

and we can rewrite the formula for emitted energy (4.12) as

$$\frac{d\mathcal{E}}{d\Omega} = \frac{c\epsilon_0}{2\pi} \int_{-\infty}^{+\infty} |\mathfrak{F}[R(t)\mathbf{E}(t)](\omega)|^2 d\omega = \frac{c\epsilon_0}{\pi} \int_0^{+\infty} |\mathfrak{F}[R(t)\mathbf{E}(t)](\omega)|^2 d\omega. \quad (4.16)$$

The radiated energy per solid angle can be related to the integral

$$\frac{d\mathcal{E}}{d\Omega} = \int_0^{+\infty} \frac{d^2I}{d\omega d\Omega} d\omega, \quad (4.17)$$

and the formula for the frequency and the angular distribution of the radiation emitted by the moving charge is

$$\frac{d^2I}{d\omega d\Omega} = \frac{c\epsilon_0}{\pi} |\mathfrak{F}[R(t)\mathbf{E}(t)](\omega)|^2. \quad (4.18)$$

This formula is essential for the calculations presented in this chapter. The task to investigate the properties of the radiation emitted by a moving charge was reformulated as the Fourier transform of the electric field generated by the charge. This electric field depends according to equation (4.5) only on the trajectory of the moving charge.

By substituting the formula for electric field (4.5) into (4.18) it can be written that

$$\frac{d^2I}{d\omega d\Omega} = \frac{c\epsilon_0}{\pi} \left| \int_{-\infty}^{+\infty} \frac{e}{4\pi\epsilon_0} \left[R \frac{\mathbf{n} \times [(\mathbf{n} - \boldsymbol{\beta}) \times \dot{\boldsymbol{\beta}}]}{cR(1 - \mathbf{n} \cdot \boldsymbol{\beta})^3} \right]_{ret} e^{i\omega t} dt \right|^2, \quad (4.19)$$

where $t = t' + \mathbf{n} \cdot \mathbf{R}(t')/c$ and by changing the integration variable from t to t' we finally obtain the famous formula for the radiation emitted by moving charge as

$$\frac{d^2I}{d\omega d\Omega} = \frac{q^2}{16\pi^3\epsilon_0 c} \times \left| \int_{-\infty}^{\infty} \exp\left(i\omega \left[t' - \frac{\mathbf{n} \cdot \mathbf{R}(t')}{c}\right]\right) \times \frac{\mathbf{n} \times [(\mathbf{n} - \boldsymbol{\beta}) \times \dot{\boldsymbol{\beta}}]}{(1 - \boldsymbol{\beta} \cdot \mathbf{n})^2} dt' \right|^2. \quad (4.20)$$

Such a major formula deserves at least a brief discussion. Let us pinpoint several observations:

1. Moving charge radiates only when it is accelerated, decelerated or changing the direction of motion.
2. Radiated energy is maximum when $\boldsymbol{\beta} \cdot \mathbf{n} \rightarrow 1$, so in the case when $\beta \approx 1$ and $\boldsymbol{\beta} \parallel \mathbf{n}$. It means that relativistic electron radiates by orders of magnitude more power than non-relativistic one and that the radiation is highly directional along the direction of its velocity.
3. Radiated energy increases with the square of the acceleration $\dot{\boldsymbol{\beta}}$.
4. The goal for X-rays generation from the relativistic electrons is to force the transverse motion of accelerated electrons. This is the principle of standard undulators and wigglers and laser plasma X-ray sources are based on this fact too.

Up to this point, radiation only of a single electron was investigated. If an incoherent electron bunch is comprised of N_e electrons, which are randomly distributed inside the bunch, then the total radiation is simply a sum of the contributions from single electrons and can be estimated as N_e times the radiation emitted by the typical electron [Corde et al., 2013]

$$\frac{d^2I}{d\omega d\Omega} = \sum_{i=1}^{N_e} \frac{d^2I_i}{d\omega d\Omega} \approx N_e \frac{d^2I}{d\omega d\Omega} \Big|_{ave}. \quad (4.21)$$

This condition is fulfilled in large synchrotrons or in laser-plasma accelerators.

Proper analysis performed in [Jackson, 1999] leads to the formula for the temporal evolution of the radiating power per unit frequency. It can be written in SI units as [Corde et al., 2013]

$$\frac{dP}{d\omega}(t) = \frac{\sqrt{3}q^2}{12\pi^2\varepsilon_0c} \frac{\omega}{\gamma^2} \int_{\omega/\omega_c}^{\infty} K_{5/3}(\zeta) d\zeta, \quad (4.22)$$

where

$$\omega_c = \frac{3\gamma^3c}{2\rho} \quad (4.23)$$

is the critical frequency, ρ is the instantaneous radius of curvature⁹ and $K_{5/3}$ is the modified Bessel function of the second kind.

Temporal evolution of the radiated power can be obtained as

$$P(t) = \int_0^{+\infty} \frac{dP}{d\omega}(t) d\omega = \frac{2e^2\omega_c^2}{17\pi\varepsilon_0c\gamma^2}, \quad (4.24)$$

total energy radiated by moving charge is

$$\mathcal{E} = \int_{t_1}^{t_2} P(t) dt = \int_{t_1}^{t_2} \int_0^{+\infty} \frac{dP}{d\omega}(t) d\omega dt. \quad (4.25)$$

Figure 4.2 shows the radiation of typical electron during its acceleration and also deceleration phases in a bubble. Its trajectory was taken from PIC simulation of the laser wakefield acceleration with the self-injection. It also includes evolution of its energy and transverse coordinate. Radiated power was calculated according to the formula (4.22). Characteristics of its radiation are linked with its trajectory. For instance, electron radiates at the most when it reaches the turning points of its betatron oscillations. Furthermore, it almost does not radiate when passing its central position on axis $y = 0$. The energy of radiation strongly depends on electron energy.

When a test electron is accelerated up to 107 MeV, the amplitude of its betatron oscillations reaches 1.56 μm at that time. The total energy radiated by the electron obtained from equation (4.25) is 4.53 keV. The critical energy of radiation averaged over

⁹If we have curve described in the Cartesian coordinates as $y = y(x)$, than radius of curvature is

$$\rho = \left| \frac{(1 + y'^2)^{3/2}}{y''} \right|.$$

The prime represents the differentiation with respect to x . If the curve is described parametrically by functions $x = x(t)$ and $y = y(t)$, than radius of curvature is

$$\rho = \left| \frac{(\dot{x}^2 + \dot{y}^2)^{3/2}}{\dot{x}\ddot{y} - \dot{y}\ddot{x}} \right|.$$

The dot means the differentiation with respect to t .

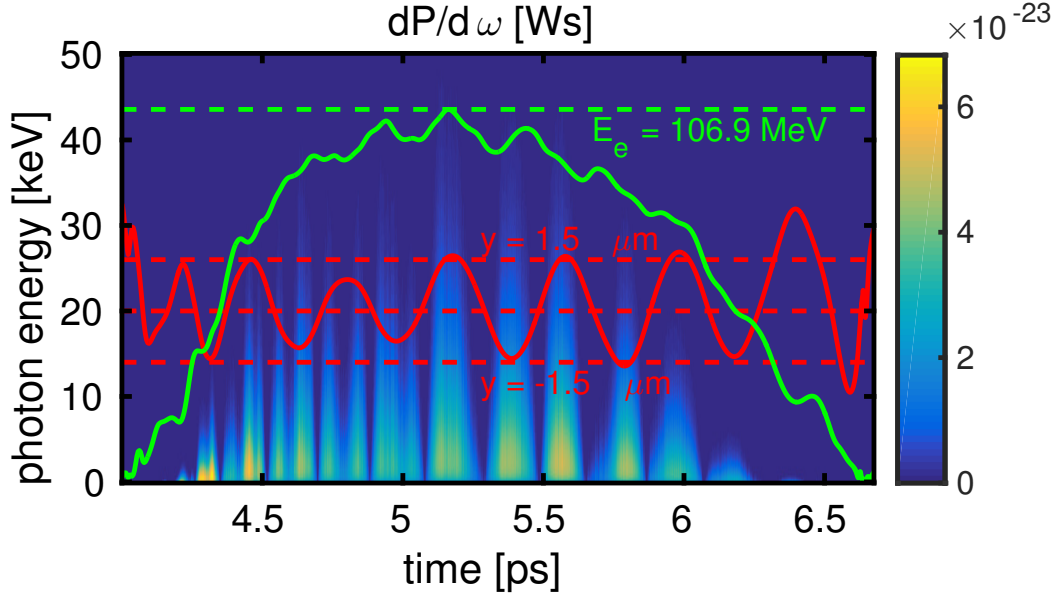


Figure 4.2: Radiation of test electron from 2D PIC simulation ($a_0 = 1.56$, $\tau = 50$ fs, $w_0 = 8 \mu\text{m}$, $n_e = 2.3 \times 10^{19} \text{ cm}^{-3}$) during its acceleration and also deceleration process. Its oscillations in transverse direction (red) and evolution of its energy (green) are schematically represented. Electron radiates most in its turning points. Energy of radiation strongly depends on electron energy.

time is 5.50 keV, according to equation (4.23). This electron emits 0.82 photons at the critical energy.

The length of X-ray bunch Δt radiated by single electron observed in the far field on the axis can be calculated. Let us consider that the radiation begins in the time t_1 and ends in the time t_2 . Hence, the time delay of between photons emitted at times of t_2 and t_1 can be written as

$$\Delta t \approx \frac{\int_{t_1}^{t_2} [c - v_x(t)] dt}{c}, \quad (4.26)$$

where v_x is the velocity of the electron in the longitudinal direction. In this case, when $t_1 \approx 4.45$ ps and $t_2 = 5.95$ ps as can be seen from the plot, the length of the radiation is 2.23 fs¹⁰. Therefore, the length of the X-ray bunch generated by all electrons in the bunch depends mainly on the length of the bunch. In principle, X-ray pulses even significantly shorter than the laser pulse length can be generated.

¹⁰Proper values of longitudinal electron velocity from PIC simulation have been substituted into equation (4.26).

4.2 Betatron radiation

The bubble acts not only as an accelerator but also as a wiggler in the bubble regime of the LWFA. It is due to the presence of the transverse electric field, which in the first approximation¹¹ takes the shape given by equation (3.21). This electric field produces a restoring force directed towards the laser pulse propagation axis. Therefore, electrons perform transverse oscillations in addition to their acceleration in the longitudinal direction. Since their energy is relativistic, X-rays are emitted. The betatron radiation mechanism was proposed and firstly demonstrated independently by Kisilev [Kiselev et al., 2004] and Rousse [Rousse et al., 2004] in 2004. The principle of a synchrotron is reproduced on a millimeter scale in order to produce X-rays.

The trajectory of the accelerated electron is sine-like. However, the amplitude of betatron oscillations r_β and betatron wavelength $\lambda_\beta \approx \frac{2\pi c}{\omega_\beta}$ evolves as the electron is accelerated. According to the model introduced by Lu [Lu et al., 2007], the frequency of the transverse oscillations (betatron frequency) is given as

$$\omega_\beta = \frac{\omega_p}{\sqrt{2\gamma}} \quad (4.27)$$

and the amplitude of the betatron oscillations is proportional to $r_\beta \sim \gamma^{-1/4}$.

In principle, two regimes of the radiation with very different features can be distinguished. The undulator regime corresponds to the situation when an accelerated electron radiates all the time along its motion. It means that the maximal angle of the trajectory with respect to the propagation axis Ψ is smaller than the opening angle of the radiation cone $\theta = 1/\gamma$. In the wiggler regime, the different sections of the electron trajectory radiate in the different directions. Both regimes are depicted in Figure 4.3. The fundamental parameter separating them is generally denoted as K and is given as

$$K = \Psi\gamma = r_\beta k_p \sqrt{\frac{\gamma}{2}}, \quad (4.28)$$

where r_β is betatron transverse amplitude of motion. In practical units, K parameter for betatron oscillations can be expressed as

$$K = 1.33 \times 10^{-10} \sqrt{\gamma n_e [\text{cm}^{-3}]} r_\beta [\mu\text{m}]. \quad (4.29)$$

The undulator regime occurs when $K \ll 1$, or alternatively when the angle Ψ is very low. An electron radiates in the longitudinal direction exclusively. The continuous profile

¹¹Model of electric and magnetic field within the elliptical bubble can be found in [Horný et al., 2018b].

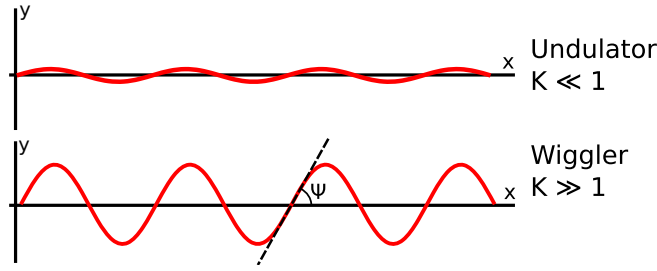


Figure 4.3: Undulator and wiggler regimes.

of emitted radiation is observed. The axis spectrum is almost monoenergetic with the fundamental frequency

$$\omega_1 = \frac{2\gamma^2\omega_\beta}{1 + K^2/2}. \quad (4.30)$$

The radiation cone angle is $\Delta\theta = 1/\gamma$ in this case.

The wiggler regime with $K \gg 1$ is characterized by the fact that during the different stages of one betatron oscillation period electron radiates in different directions. As we already know from the equation (4.20), the electron radiates mainly when its acceleration $\dot{\beta}$ is maximal, i.e. in the turning points of its trajectory. Hence, the observer on the axis receives bursts of radiation separated by a time $\lambda_\beta/2c$. The observer out of axis observes less energetic radiation bursts separated by a time λ_β/c . The duration of one burst is

$$\tau = \frac{13\rho}{24\gamma^3c} \approx \frac{1}{\omega_c}. \quad (4.31)$$

The radiation cone angle is $\Delta\theta = K/\gamma^2$, which is greater than $1/\gamma$. The radiated spectrum is comprised of many harmonics of the fundamental frequency up to the critical frequency

$$\omega_c = \frac{3}{2}K\gamma^2\omega_\beta. \quad (4.32)$$

A related critical energy can be written in practical units as

$$\hbar\omega_c [\text{eV}] = 5.24 \times 10^{-21}\gamma^2n_e[\text{cm}^{-3}]r_\beta[\mu\text{m}]. \quad (4.33)$$

The experimental findings have shown that the betatron radiation occurs dominantly in the wiggler regime [Rousse et al., 2004, Ta Phuoc et al., 2006], [Kneip et al., 2008, Mangles et al., 2009] and it was demonstrated that the spectrum of betatron radiation in the wiggler regime is synchrotron-like [Fourmaux et al., 2011]. Influence of direct laser acceleration (i.e. Thomson scattering) on the spectrum of betatron radiation from LWFA is currently being extensively discussed [Li et al., 2016, Shaw et al., 2016]. However, it seems that such a phenomenon only plays a minor role in the early stages of the acceleration process; therefore it can be omitted.

4.2.1 Method to calculate the radiation properties

A new method to calculate the properties of the betatron radiation from the knowledge of the trajectories of the accelerated electrons was proposed, implemented, and demonstrated. It enables to calculate the angular and the frequency spectrum of the betatron radiation $\frac{d^2I}{d\omega d\Omega}$ emitted by an electron bunch. Firstly, the electric field generated by an oscillating electron is calculated using the equation (4.5). Afterwards, the Fourier transform of its *only relevant parts* is performed using equation (4.18). The novelty of this method in comparison with the state-of-art approaches is that the uninteresting and insignificant parts of the signal can be neglected; thus a memory demands are reduced significantly. Moreover, the proposed method can be generalized to the construction of the spectrogram $\frac{d^3I}{dt d\omega d\Omega}$ for most cases.

This method was recently published [Horný et al., 2017a]. It is complementary to the alternative treatments earlier proposed by Thomas [Thomas, 2010a] and by Chen [Chen et al., 2013], which are based on the semi-analytical approach to the solution of the integral in (4.20).

As it was already implied, the core of the method is to perform the Fourier transform of the quantity $\mathbf{E}(t)R(t)$. Thus, such a quantity must be properly sampled in order to calculate the full spectrum of emitted X-rays. The minimum sampling frequency is determined by Whittaker–Nyquist–Kotelnikov–Shannon sampling theorem¹². It states that the accurate reconstruction of the continuous signal whose frequencies are limited is possible only if the sampling frequency is higher than twice the highest frequency component of the sampled signal. In practice, if the radiation energy spectrum is requested to be calculated up to the energy 15 keV, the corresponding photon’s frequency is 3.64×10^{18} Hz, the sampling frequency of the signal should be 7.28×10^{18} Hz and it means that the length of the time step Δt of the electric field in the observer’s spot has been at most 0.14 as. If the radiation bandwidth reaches as far as 1 MeV, such a time step has to be at most 2.1 zs long. In comparison, a typical time step in PIC simulations of LWFA is 0.01–0.1 fs citetsung2006simulation, which results to typically sub-as time steps in the observer’s time t .

Furthermore, sampling in the observer’s time t is usually not equidistant. The interpolation of the function $\mathbf{E}(t)R(t)$ must be carried out to obtain better sampling. Various interpolation methods may be used; however, shape-preserving piecewise cubic interpolation offers satisfactory results with respect to the computational time demands. Once the interpolated signal $\mathbf{E}(t)R(t)$ is sampled properly, its fast Fourier transform can be computed. It is advisable to use the zero-padding technique [Smith, 2007] to increase

¹²Its overview is given e.g. in [Jerri, 1977].

the resolution of spectra obtained via FFT.

A certain alternative for low energy radiation can be non-uniform fast Fourier transform algorithm (NUFFT) [Fessler and Sutton, 2003]. However, this algorithm was not implemented in this work.

4.2.2 Test of the method

Let us firstly demonstrate this new method and the related physics on the several text-book examples. Example electron trajectories were calculated using the simple model

$$y(t) = r_\beta \sin(\omega_\beta t), \quad (4.34)$$

for the ambient electron density $n_e = 5 \times 10^{18} \text{ cm}^{-3}$. Electron propagated for 4 ps without any acceleration, it means that both r_β and ω_β do not evolve.

The electric field in the far field approximation was calculated using the radiation term in the formula (4.5). Without loss of generality, let us assume that the electron propagates in the x -direction and performs transverse betatron oscillations in the y -direction. Then $|E_x/E_y| \ll 1$ and $|E_z/E_y| \ll 1$, and

$$|\mathfrak{F}[R(t)\mathbf{E}(t)](\omega)| \approx |\mathfrak{F}[R(t)E_y(t)](\omega)|.$$

Hence, the contribution of the electric field components E_x and E_z can be neglected.

The results of these computations for various parameters of the electron trajectory are plotted in Figure 4.4. The quantity $E_y(t)R(t)$ is plotted in the left column, the time duration t correspond to the inertial reference frame of the observer. In the right column, the corresponding spectrum on the axis of laser propagation is shown. The clear difference between undulator and wiggler regime is apparent. It is worth mentioning that this betatron radiation pulse length decreases with the electron energy and increases with the oscillation amplitude.

In the case A, the electric field signal is continuous and the Fourier series comprise only of the fundamental frequency. The electron has low energy $E_e = 10 \text{ MeV}$ and it oscillates with the amplitude $0.05 \text{ }\mu\text{m}$. The emitted radiation profile has a sine-like shape with the turning points interconnected with the peaks of the electron's trajectory. The length of the observed signal is 4.8 fs. The only fundamental harmonic peak position is at 10.8 eV, as it can be calculated from equation (4.30). As the electron performed eleven oscillations, the width of the line is $\Delta\omega/\omega = 1/11$. This case represents an undulator regime with the K parameter 0.066.

In the case B, the electron energy is 25 MeV and its oscillation amplitude is $0.5 \text{ }\mu\text{m}$, the value of K is 1.0. The basic harmonic energy increases up to 26.1 eV and third, fifth

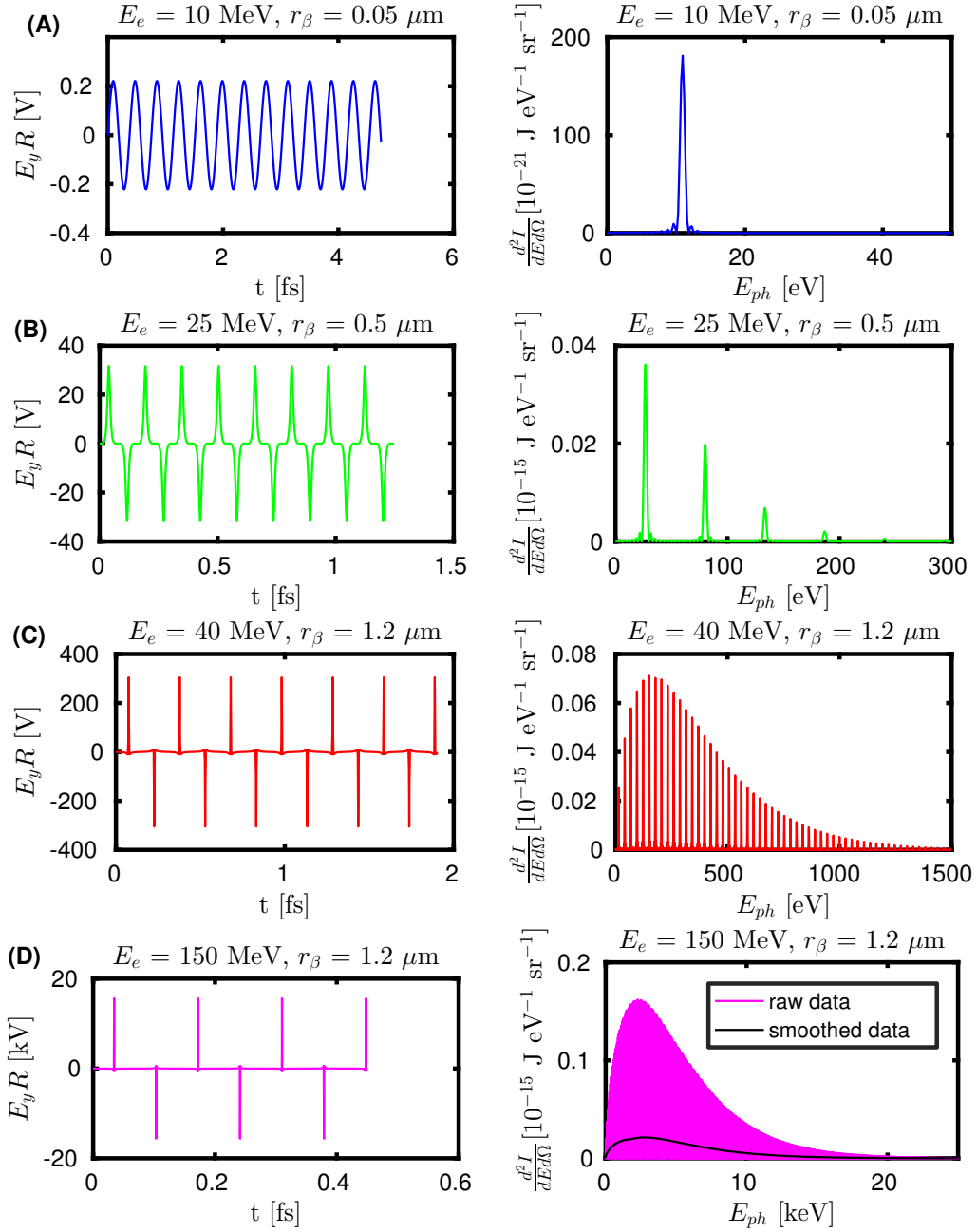


Figure 4.4: Electric field and radiated spectrum on axis by a moving electron for various electron energies and amplitudes of the betatron oscillations.

seventh and ninth harmonics are present, because the even ones vanish. The third case C is close to the wiggler regime. Electron energy is 40 MeV, amplitude of oscillations is $1.2 \mu\text{m}$, $K = 3.15$. It is still possible to distinguish single harmonics; nevertheless, their envelope has already characteristic shape of the synchrotron radiation. The basic harmonic is 13.6 eV, the highest harmonic effectively present is approximately the 137th one with the energy 1.86 keV.

The case D represents example of wiggler regime with the $E_e = 150 \text{ MeV}$, $r_\beta = 1.2 \mu\text{m}$ and $K = 5.46$. The emitted radiation is comprised of many very closely spaced harmonics, therefore it can be considered as a continuous synchrotron radiation. The black line represents spectrum smoothed using moving average window technique¹³. The critical energy of radiation, calculated as the median in the spectral intensity on axis divided by the factor of 1.54¹⁴, is 2.70 keV in this case, which is in the agreement with the expectation according to the formula (4.33). Furthermore, the high energy tail of the radiation reaches up to 20 keV, i.e. hard X-rays are generated. The most contemporary experiments are carried out in such a regime.

4.2.3 Simplification of the method for the wiggler case

It can be understood from Figure 4.4 that in the wiggler case, the electron emits radiation almost exclusively in the turning points of its sine-like trajectory. Hence, there are only a few very narrow time intervals, which contribute significantly to the betatron radiation emission, while the rest can be neglected.

Analogical behaviour was observed also previously for nonlinear Thomson scattering [Andreev et al., 2011]. It was shown that the trajectory of an electron oscillating in the field of the relativistic laser pulse is comprised of relatively long rectilinear segments with the short looping turns between them. Such a trajectory can be seen in Figure 2.3. The temporal evolution of the electric field $\mathbf{E}(t)R(t)$ is therefore similar to the one in Figure 4.4d.

Let us consider the signal of the radiation $\mathbf{u}(t) = \mathbf{E}(t)R(t)$ as a sum of the contributions

¹³Moving average window technique is a standard statistical tool to analyze data points by creating series of averages of partial subsets of the full data set in order to smooth out short-term fluctuations and highlight longer-term trends or cycles [Kenney and Keeping, 1965]. The size of inner subsets was 1/25000 of the full radiation spectrum bandwidth in examples presented in this work.

¹⁴Median in the synchrotron radiation spectral intensity on axis $\left. \frac{d^2 I}{dE d\Omega} \right|_{\theta=0}$ is $1.54 \times$ higher than the median in the angularly integrated spectral intensity $\frac{dI}{dE}$ [Esarey et al., 2002], which is one of the characteristics of the critical energy [Jackson, 1999]. See also an explanation in [Ju, 2013], but avoid the confusion due to different definitions of the critical energy.

by single peaks $\mathbf{u}_j(t)$, i.e.

$$\mathbf{u}(t) = \sum_{j=1}^{N_p} \mathbf{u}_j(t), \quad (4.35)$$

where N_p is number of peaks. Each contribution can be written as

$$\mathbf{u}_j(t) = \begin{cases} \mathbf{E}(t)R(t) & |t - t_j| < \Delta t \\ 0 & \text{otherwise,} \end{cases} \quad (4.36)$$

where t_j are the times of the signal peaks and Δt are the widths of the considered peaks. These widths has to include the whole peaks and cannot overlap each other.

The equation for the radiated energy per solid angle (4.12) can be in this case reformulated to

$$\frac{d\mathcal{E}}{d\Omega} = c\varepsilon_0 \int_{-\infty}^{+\infty} \left| \sum_{j=1}^{N_p} \mathbf{u}_j(t) \right|^2 dt. \quad (4.37)$$

Thanks to the fact that the contributions of the single peaks do not overlap, the square of the absolute value of the sum of the contributions is equal to the sum of the squares of the single contributions

$$\frac{d\mathcal{E}}{d\Omega} = c\varepsilon_0 \int_{-\infty}^{+\infty} \sum_{j=1}^{N_p} |\mathbf{u}_j(t)|^2 dt \quad (4.38)$$

and thanks to the linearity of integration

$$\frac{d\mathcal{E}}{d\Omega} = c\varepsilon_0 \sum_{j=1}^{N_p} \int_{-\infty}^{+\infty} |\mathbf{u}_j(t)|^2 dt. \quad (4.39)$$

Using once again Parseval's theorem and sum rule we obtain

$$\begin{aligned} \frac{d\mathcal{E}}{d\Omega} &= \frac{c\varepsilon_0}{\pi} \sum_{j=1}^{N_p} \int_0^{+\infty} |\mathfrak{F}[\mathbf{u}_j(t)](\omega)|^2 d\omega \\ &= \int_0^{+\infty} \frac{c\varepsilon_0}{\pi} \sum_{j=1}^{N_p} |\mathfrak{F}[\mathbf{u}_j(t)](\omega)|^2 d\omega. \end{aligned} \quad (4.40)$$

Hence, the spectral intensity of the radiation is similar as in the equation (4.18)

$$\frac{d^2 I}{d\omega d\Omega} = \frac{c\varepsilon_0}{\pi} \sum_{j=1}^{N_p} |\mathfrak{F}[\mathbf{u}_j(t)](\omega)|^2. \quad (4.41)$$

In conclusion, the calculation of the radiation emitted by a single electron in the wiggler case can be simplified to the calculation of the sum of the contributions to the radiation emitted in N_p turning points of its sine-like trajectory

$$\frac{d^2 I}{d\omega d\Omega} = \sum_{j=1}^{N_p} \left. \frac{d^2 I}{d\omega d\Omega} \right|_j. \quad (4.42)$$

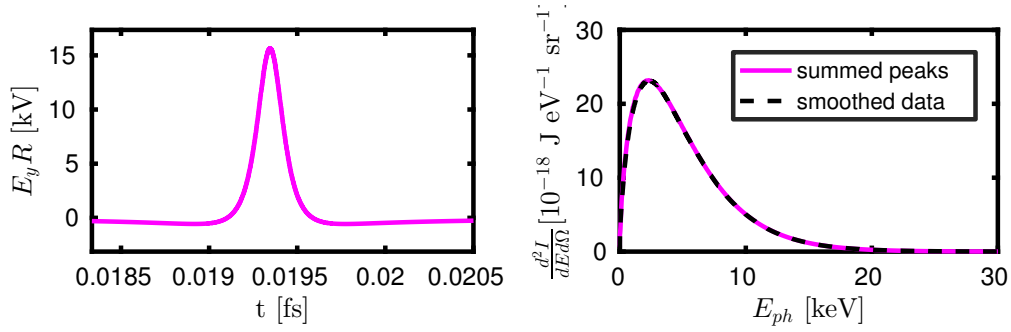


Figure 4.5: Left: One peak of the radiation signal $R(t)E_y(t)$ from the case D in Figure 4.4. Right: Its spectrum calculated as a sum of the contributions by single peaks (magenta solid) and a smoothed spectrum calculated according to the equation (4.18) using the Fourier transform of the whole signal (black dashed).

Thus, the long time interval can be replaced by several much shorter time intervals. This is particularly helpful when high energy radiation is expected and the length of the signal due to huge sampling rate places high demands on the memory.

The radiation spectrum of the 150 MeV electron oscillating with the betatron amplitude $1.2 \mu\text{m}$ (wiggler case from Figure 4.4) calculated as a sum of contributions to the radiation by single peaks is practically equal to its smoothed spectrum calculated according to the equation (4.18) as can be seen in Figure 4.5.

Additionally, a similar demonstration was performed also for a more realistic problem, in particular for the example electron trajectory from PIC simulation. This trajectory was taken from simulation, which will be introduced in Section 4.2.5. Figure 4.6 claims that the radiation spectrum calculated using simplified method is practically indistinguishable from the one obtained by the general approach if this is smoothed. The information about fine structure is lost using the smoothing or the simplified method though.

If the incoherent nature of the electrons in the bunch is justified, the radiation power emitted by an electron bunch is equal to the sum of powers emitted by each electron, as it was pointed out earlier by equation (4.21). Adapting the simplification introduced above, the total radiation emitted by a bunch containing N_e electrons can be written as

$$\frac{d^2I}{d\omega d\Omega} = \sum_{i=1}^{N_e} \sum_{j=1}^{N_{p,i}} \left. \frac{d^2I}{d\omega d\Omega} \right|_{ij} = \sum_{k=1}^{N_P} \left. \frac{d^2I}{d\omega d\Omega} \right|_k, \quad (4.43)$$

because all the contributions to the total radiation by all electrons are summed up and it does not depend on the order of the summation.

As the trajectories of individual electrons in the beam differ, the spectra of emitted radiation do not show the same fine structure. Therefore, the fine structure in Figure 4.6 is likely the feature only of the radiation by a single particle, and it vanishes when

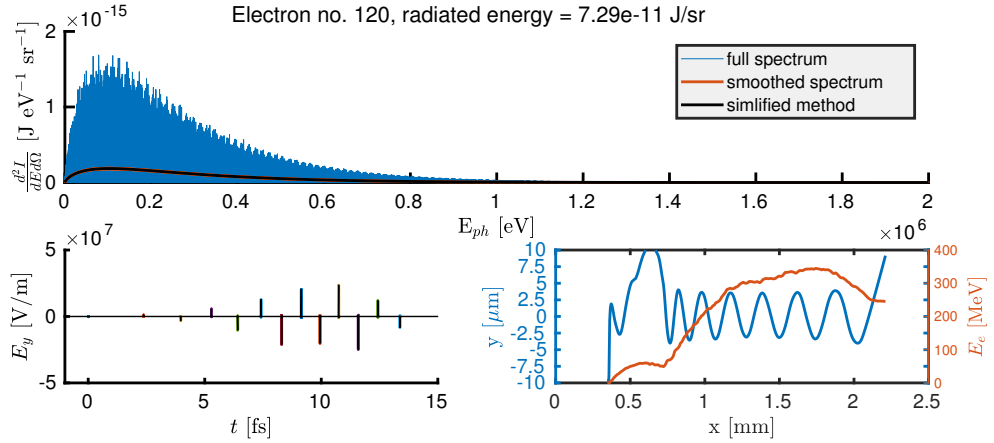


Figure 4.6: Upper row: Radiated spectrum by a moving electron on axis for the electron trajectory taken from simulation introduced in Section 4.2.5 Blue: calculated using general approach. Brown: blue line smoothed using moving average window technique. Black: corresponding spectrum calculated as a sum of contributions by single peaks. Bottom left: Radiation signal $E_y(t)R(t)$ (black) and chosen separated peaks. Bottom right: Electron trajectory in xy -plane (blue, left axis) and evolution of electron energy (brown, right axis).

summing the spectra of N_e particles.

4.2.4 Spectrogram: temporal evolution of radiation profile

We can define the quantity of radiated energy per unit frequency and per unit solid angle received during certain time interval $t \in [\tau - \Delta\tau, \tau + \Delta\tau]$ as

$$\left. \frac{d^2 I}{d\omega d\Omega} \right|_{t \in [\tau - \Delta\tau, \tau + \Delta\tau]} = \sum_{k | t_k \in [\tau - \Delta\tau, \tau + \Delta\tau]} \left. \frac{d^2 I}{d\omega d\Omega} \right|_k. \quad (4.44)$$

In a practical implementation, every time moment t_k when the peak of the radiation by any single electron occurs is stored and total radiation received during time interval $t \in [t_{k_i}, t_{k_{i+1}}]$ is summed up applying the equation (4.44). In further text, the quantity $\left. \frac{d^2 I}{d\omega d\Omega} \right|_{t \in [\tau - \Delta\tau, \tau + \Delta\tau]}$ will be marked as $\frac{d^3 I}{dt d\omega d\Omega}$ (or rather $\frac{d^3 I}{dt dE d\Omega}$, since energy spectrograms will be plotted).

4.2.5 Betatron radiation pulse length

The characteristics of the betatron radiation pulse including their length will be investigated for four different parameter regimes of LWFA. The first one is a standard configuration of bubble regime with the self-injection available with current 100 TW class laser systems [Esarey et al., 2009]. The second and the third cases investigate schemes of optical injection by transverse laser pulse [Horný et al., 2017b] introduced

in Section 3.4.4, and preceding laser pulse [Horný et al., 2018a] introduced in Section 3.5.4, respectively, under similar conditions. It enables significant shortening of the X-ray pulse duration to values below 3 fs. The last one is the experimental configuration using sub-10 TW laser system employing ionization injection. The EPOCH 2D code [Arber et al., 2015] extended by particle tracker subroutine¹⁵ was used to perform PIC simulations of laser wakefield electron acceleration and to store the trajectories of trapped particles.

Simulation parameters were following: simulation box size was $120\ \mu\text{m} \times 60\ \mu\text{m}$ (moving window), grid resolution was 30 cells per wavelength in the longitudinal direction and 6 cells per wavelength in the transverse direction. There were 3 electron macroparticles per cell in all the examples except the ionization injection, where one oxygen and one nitrogen macroparticle were placed in every cell at the beginning of a simulation, and macroparticles representing electrons were initialized during the simulation.

■ Standard self-injection with 100 TW laser

The 40 fs long 800 nm wavelength Gaussian laser pulse with laser strength parameter $a_0 = 4$ interacts with transversally uniform 2 mm thick plasma layer with electron density $n_e = 1.5 \times 10^{19}\ \text{cm}^{-3}$ and 40 μm long linear density ramps on both sides in the propagation direction. The focus is located at the end of the front ramp and the waist size is 9 μm .

The PIC simulation has shown, that electron self-injection into the bubble is continuous. Electron energy spectrum is therefore continuous as well, with maximum energy around 380 MeV. The spectrogram of the radiation calculated using the stored trajectories of 5 000 randomly selected trapped macroparticles ($\approx 24\%$ of all of them)¹⁶ is depicted

¹⁵The subroutine which enables to store the trajectories of the selected macroparticles from PIC simulation was implemented to the EPOCH code by the author. The positions and momenta of these electrons are stored in every time step of the simulation. The simulation is always run twice. Firstly, the identification numbers of the trapped macroparticles are determined. Then, a certain representative sample of them is selected and stored in an additional input file. Afterwards, the simulation is rerun from the same compiled binary.

If the code runs on N parallel central processing units (CPU), N additional output files are generated, each of them belongs to the corresponding CPU in order to obviate the I/O errors in MPI (massive parallel interface) parallelization. In every time step of PIC simulation, when a certain CPU processes some macroparticle selected to be tracked, the immediate information about such a macroparticle is stored in the related output file. However, such an approach leads to unsorted results, as the macroparticles may migrate between CPUs. Thus, post-processing tools were developed. These scripts create special files for each selected macroparticle trajectory and sort it with respect to time.

¹⁶The sample of trapped macroparticles must well represent the properties of injected electron bunch. Based on authors' experience, at least 5% of trapped macroparticles should be tracked to provide

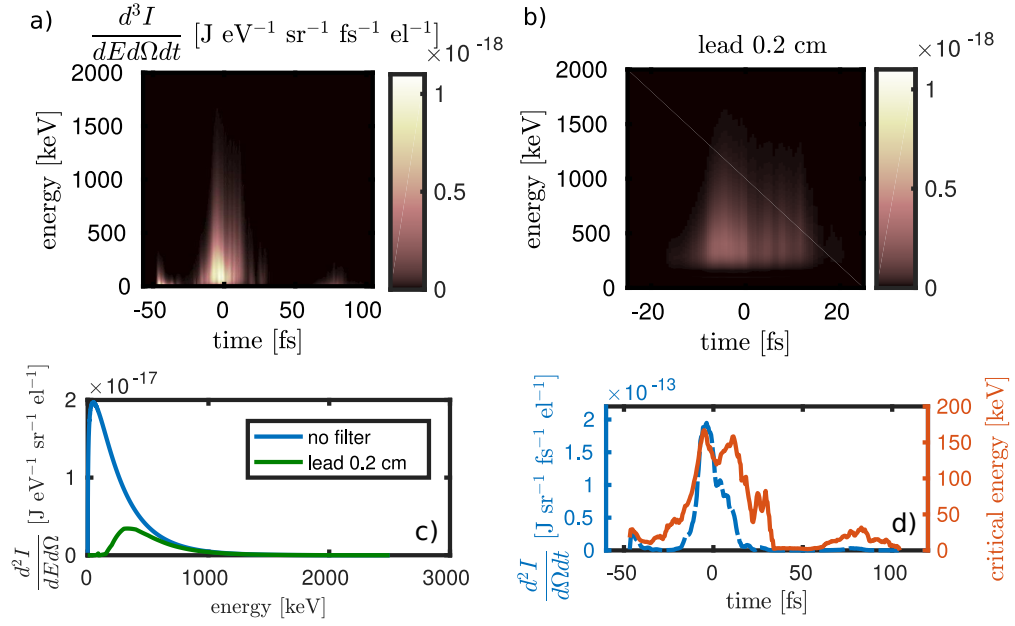


Figure 4.7: Betatron radiation from standard LWFA experiment ($\tau = 40$ fs, $\lambda = 800$ nm, $a_0 = 4$, $w_0 = 9$ μm , $n_e = 1.5 \times 10^{19}$ cm^{-3}). a) Original spectrogram without any filter. b) Radiation spectrogram filtered using 2 mm lead foil. c) Total energy spectrum on axis without (blue) and with 2 mm lead filter (green). d) Temporal profile of radiated power (left axis, blue) and temporal evolution of critical energy (right axis, brown).

together with its time and energy integrals in Figure 4.7. The critical energy of the radiation is 127 keV, X-ray pulse length is 13.7 fs (FWHM). Although there are additional X-ray pulses occurring 40 fs before and 70 fs after the main pulse, their intensities are much weaker.

Generated pre-pulse and post-pulse can be conveniently removed using suitable transmission filter. The impact of the usage of 2 mm thick lead filter on generated X-rays is represented on spectrogram in Figure 4.7b). The X-ray mass attenuation coefficients were taken from [Hubbell and Seltzer, 1995]. Figure 4.7c) illustrates the change of the radiation energy spectrum after propagation through the aforementioned filter. Relatively low energy radiation is fully absorbed; whereas the high energy tail remains uninfluenced. Figure 4.7d) shows a temporal profile of radiated power and confirms the elimination of pre- and post-pulses.

sufficiently accurate result.

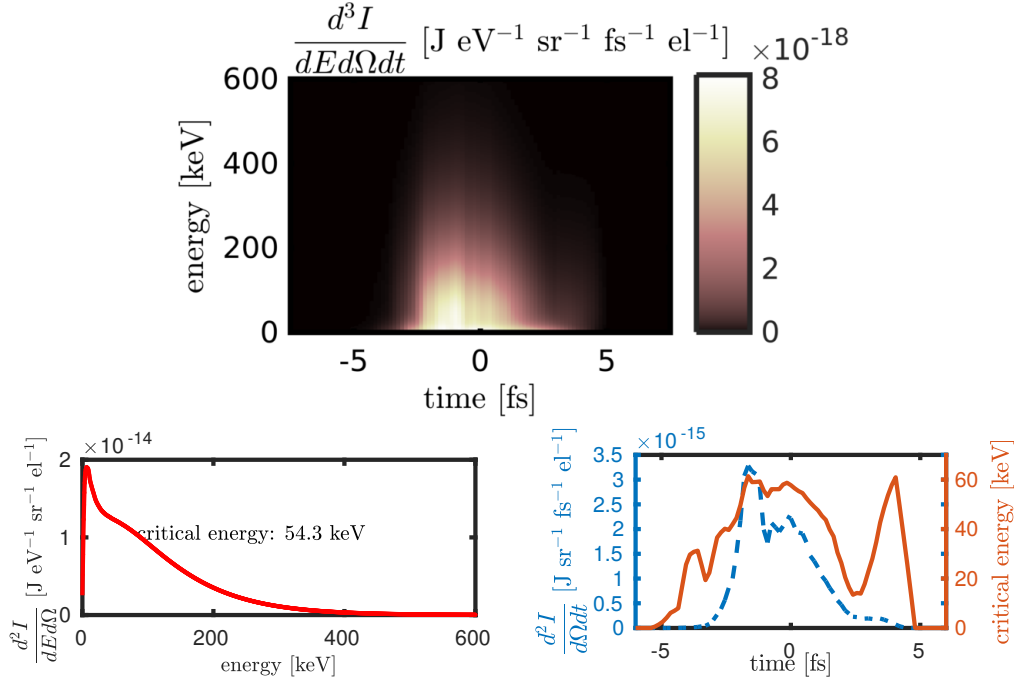


Figure 4.8: Betatron radiation in OC3P case. The electron spectrum is quasimonoenergetic with a peak energy of 530MeV and relative energy spread of 8% when the bunch is leaving the plasma layer. Betatron oscillations amplitude is up to 1.3 μm . a) X-ray spectrogram. b) Spectrum on axis, $E_c = 54.3$ keV. c) Temporal profile of radiated power on axis (blue dashed, left axis), pulse duration is 2.64 fs (FWHM), and temporal evolution of critical energy (brown solid, right axis).

Short X-ray pulses by novel crossed pulse scheme

The properties of the betatron radiation generated by newly introduced optical injection scheme with crossed laser pulses were also calculated. The trajectories from the PIC simulation described in Section 3.4.4 was used, plasma layer is 2 mm thick, similarly as in Section 4.2.5. 10 000 trapped macroparticles ($\approx 55\%$ of all of them) were used to calculate the spectrogram of radiation. Thanks to the short length of the electron bunch ($L = 1.95$ μm), the estimated duration of the X-ray pulse is short too. The X-ray pulse length is 2.64 fs (FWHM), its critical energy is 54.3 keV. The spectrogram of the betatron radiation on axis and its energy and temporal integrals are depicted in Figure 4.8.

Short X-ray pulses by novel scheme of preceding injection pulse

The spectrogram of the emitted radiation is calculated for the optical injection scheme by preceding pulse described in Section 3.5.4 too. The trajectories of 10 000 macroparticles

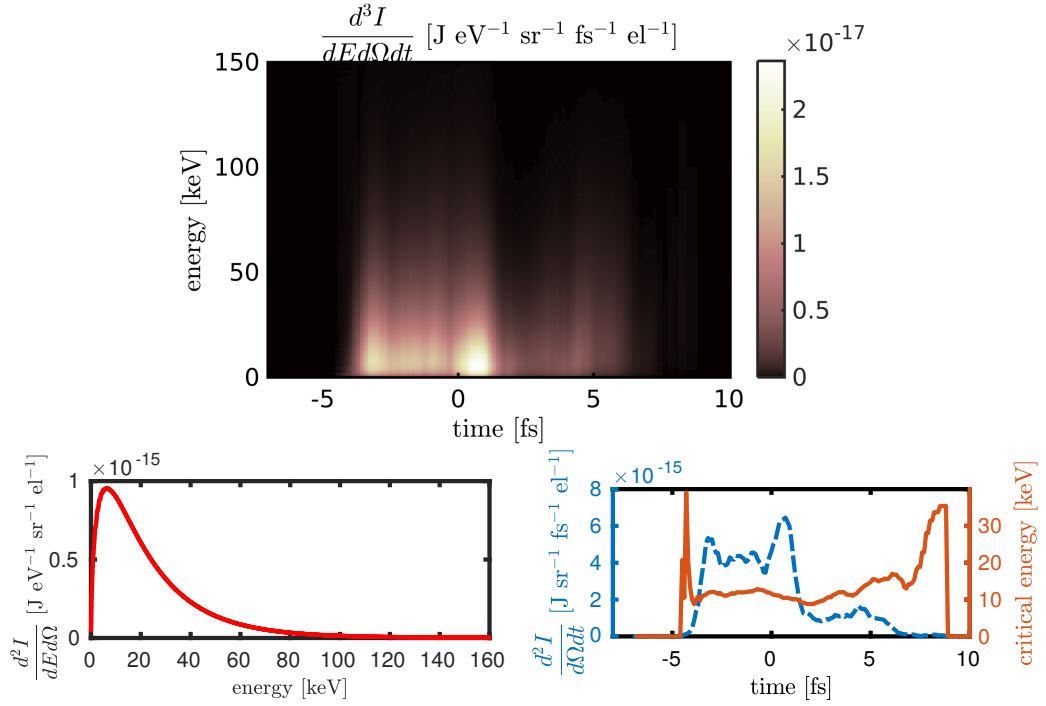


Figure 4.9: Betatron radiation in the case of optical injection by preceding pulse. Electrons are accelerated up to 390 MeV with 10% energy spread. Betatron oscillations amplitude is up to 1.2 μm . a) X-ray spectrogram. b) Spectrum on axis, critical energy is $E_c = 11.6$ keV. c) Temporal profile of radiated power on axis (blue dashed, left axis), pulse duration is 4.8 fs (FWHM), and temporal evolution of critical energy (brown solid, right axis).

($\approx 58\%$ of all of them) from 2D PIC simulation similar to the previous example are chosen. The laser and plasma parameters are the following: $a_0 = 4$, $a_1 = 2.5$, $\tau = 25$ fs, $w_0 = 9.5$ μm , $n_e = 3 \times 10^{18}$ cm^{-3} , a delay between both pulses is 65 fs. The plasma layer is 2 mm thick, the same as in both previous examples. Similarly, as in OC3P case, the estimated duration of the X-ray pulse is short as well. The length of the electron bunch is ($L = 5.9$ μm). It results in the X-ray pulse length of 4.8 fs (FWHM). Its critical energy is 11.6 keV. The spectrogram of the betatron radiation on axis and its energy and temporal integrals are depicted in Figure 4.9.

■ Comparisons between three previous configurations

Despite the similar characteristics of the laser pulses in all three previous examples, the betatron radiation characteristics differ significantly. The betatron radiation features strongly depend on the technique of the electron injection into the bubble. The comparison is given in Table 4.1. The highest critical energy of the betatron radiation was calculated for the self-injection case. It corresponds to expectations given by equation (4.33), as

| | n_e [10^{18} cm^{-3}] | τ [fs] | a_0 | a_1 | w_0 [μm] | E_c [keV] | τ_γ [fs] | N |
|-----------------|--|----------------|-------|-------|----------------------------|----------------|-----------------------|------|
| self-injection | 15 | 40 | 4 | - | 9 | 127 | 13.7 | 0.95 |
| OC3P | 5 | 25 | 4 | 0.4 | 9.5 | 54.3 | 2.6 | 0.54 |
| preceding pulse | 3 | 25 | 4 | 2.5 | 9.5 | 11.6 | 4.8 | 0.48 |

Table 4.1: Betatron radiation features for different injection schemes. Length of the plasma layer was 2 mm in all the cases.

E_c is directly proportional to the electron density. Interestingly, both optical injection schemes differ even more than it would be expected from the differences of their plasma densities. Such a difference is explained by the dynamics of both injections. It leads to the lower amplitude of betatron oscillations in the injection scheme by the preceding pulse.

On the other hand, both optical injection schemes suggest the generation of much shorter X-ray pulses. The duration of X-ray pulse depends mainly on the length of the injected electron bunch L . However, it is worth noting that our calculation suggests that this duration is shorter than classical estimate L/c , which would be 6.5 fs for the OC3P case.

The total number of radiated photons at the mean photon energy (i.e. ≈ 0.3 of critical energy) per trapped electron N is the highest for self-injection case, and comparable for both optical injection cases. The higher injected charge in the self-injection scheme leads to higher intensity of betatron radiation in this case.

■ Ionization injection by sub-10 TW laser

Finally, the features of the betatron radiation generated during the experimental campaign at the PALS laboratory, which was discussed already in Section 3.6.1, were determined

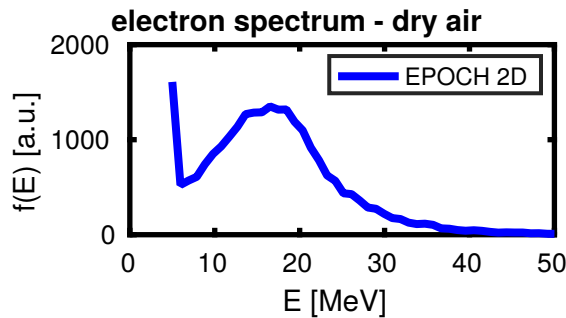


Figure 4.10: Electron spectra from PIC simulations at the end of the plasma layer.

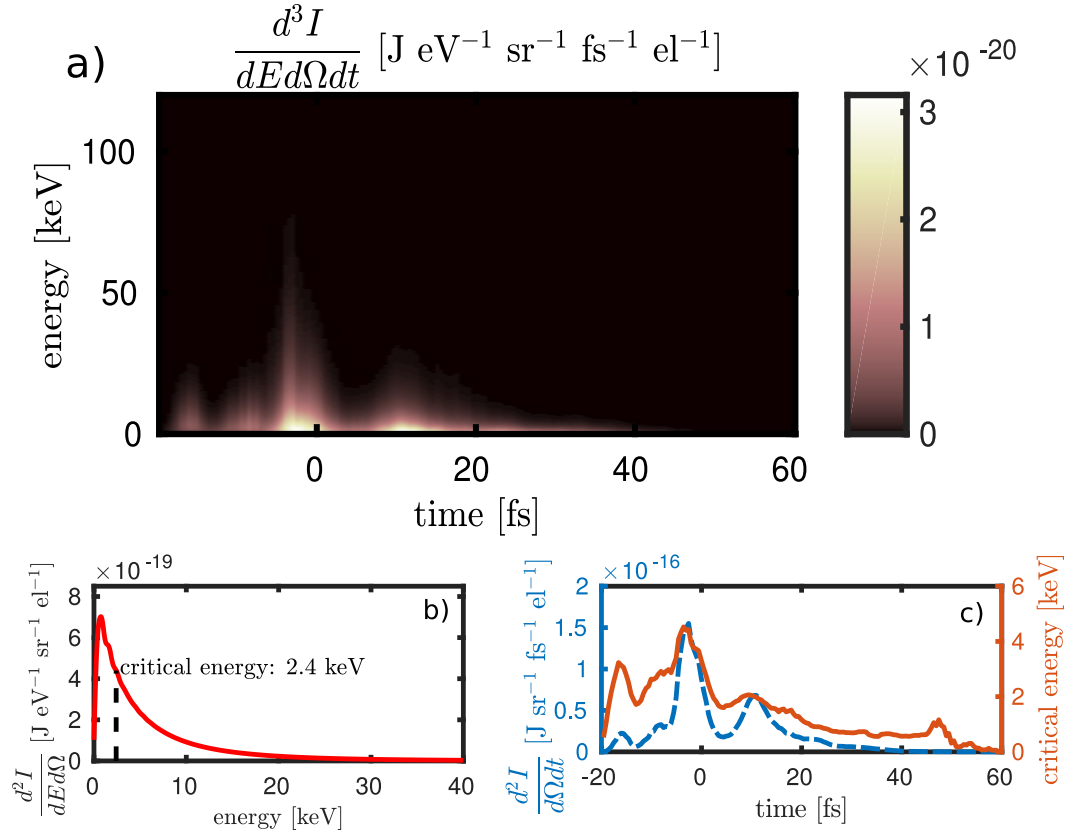


Figure 4.11: Betatron radiation for ionization injection for the experiment at PALS laboratory. Electrons are accelerated up to 30 MeV; the spectrum is continuous. Betatron oscillations amplitude exceeds 2 μm . a) X-ray spectrogram. b) Spectrum on axis, $E_c = 2.4$ keV. c) Temporal profile of on axis radiated power (blue dashed line, left axis), pulse duration is ≈ 30 fs, and temporal evolution of critical energy (brown solid line, right axis).

too. Unfortunately, the betatron radiation features were not measured at that stage. Thus, the calculation results cannot be compared with the experimental data.

As it was already stated in Section 3.6.1 and in [Boháček et al., 2018], highly stable electron bunches with mean energy 17 MeV and energy spread 14 MeV (root mean squared) were measured. Corresponding PIC simulations are carried out to support this observation. The peak electron energy of 17.1 MeV with the energy spread of 12.1 MeV obtained from the simulations well agrees with measured data (compare Figures 3.26 and 4.10). The simulated spectrum shown in Figure 4.10 comes from the end of the plasma layer at the time 1.7 ps after the moment when the laser pulse reached the focal spot.

The trajectories of the representative sample of the trapped electrons were tracked (3 000 macroparticles i.e. $\approx 15\%$ of all of them). The spectrogram of the radiation calculated using our method is presented in Figure 4.11. The shape of the X-ray

spectrogram is well reflecting the fact that there were two moments of injection in the simulation. The length of the X-ray signal is approximately 30 fs and the critical energy is 2.4 keV.

4.2.6 Discussion

Betatron radiation can be considered as a promising tool which provides hard X-rays of superior features in certain aspects. Its main advantage is a tiny source size as small as few microns and, as it was shown in this section, a very short pulse duration. Such compact sources provide intense incoherent femtosecond X-ray pulses with low divergence beams, which may find application in fundamental science, industry, or medicine [Yamanouchi et al., 2015, Miller, 2014, Bloembergen, 1999, Rousse et al., 2001, Chapman et al., 2011].

The calculations presented here indicate that generated X-ray pulse lengths are typically shorter than the driver laser pulse lengths. Moreover, the betatron hard X-ray pulses as short as few femtoseconds can be generated using new optical injection scheme. Such a short length enables novel applications such as measurement of vibrational spectra dynamics in atoms because of their periods in the order of tens of femtosecond [Levitin, 2004]. Once having an X-ray source producing even shorter pulses, the fundamental physical processes such as electron transfer, lattice vibrations, phase transitions, chemical reactions, or a spin dynamics could be sampled and therefore possibly better understood. Thus, the knowledge of the laser produced betatron X-ray pulse length and even temporal profile is crucial.

Unfortunately, the betatron radiation pulse length is a characteristic which can be measured only using sophisticated pump-probe techniques that most likely have not been performed experimentally yet. Nevertheless, we are convinced the introduced method represents a useful tool to investigate or to tailor the betatron X-ray pulse temporal profiles and it can be used to design sources for future applications such as probing of ultrafast fundamental physical processes.

4.3 Thomson scattering

The femtosecond X-ray pulses can be also produced from electrons oscillating in the field of an electromagnetic wave. The responsible physical phenomenon is often referred to as Compton scattering. From the quantum mechanics viewpoint, it is actually an absorption of one or several photons by an electron and consequential emission of a single photon. In the case, when photon energy is much lower than the rest energy of

the electron in its rest frame, i.e. $\hbar\omega \ll mc^2$, the phenomenon is known as Thomson scattering. In other words, Thomson scattering can be considered as the low energy limit of Compton scattering. Quantum electrodynamics effects, such as radiation reaction [Jackson, 1999] of an electron, are neglected here as we focus mainly on sub-GeV single electron scattering in the field of the laser with $a_0 \lesssim 15$.

In principle, two regimes of X-ray generation based on Thomson scattering can be considered. They are nonlinear Thomson scattering and Thomson backscattering. The difference between them is in the initial energy of electrons. The characteristics of X-rays generated in these two regimes differ significantly.

■ 4.3.1 Nonlinear Thomson scattering

The first regime is a nonlinear Thomson scattering, probably the simplest possible mechanism of X-ray generation which consists only of the focusing of the high-intensity laser to the (e.g. gaseous) target. Electrons which are initially at rest interact with this pulse with $a_0 \gg 1$, therefore the attribute *nonlinear*. In the linear case, electron only oscillates in the plane perpendicular to the laser pulse propagation direction and emits the radiation with the frequency of the laser. Thus, no X-rays are generated.

As the relativistic laser pulse wiggles electrons, they perform the highly nonlinear motion. The emitted radiation consists of many high order harmonics. However, the generation of X-rays in the keV region requires intense laser pulse with $a_0 > 10$.

As an illustration, several radiation spectra are calculated for the case with the linear laser polarization. The electron is located on the axis and it was at rest before the laser pulse arrival. A plane laser wave with Gaussian temporal envelope with $\tau = 25$ fs and $\lambda_L = 0.8 \mu\text{m}$ is considered. Its electric field is given as

$$\mathbf{E}(x, t) = \frac{m_e c \omega_L a_0}{e} \exp \left[-2 \ln 2 \frac{(x - ct)^2}{c^2 \tau^2} \right] \cos(\omega_L t - k_L x) \mathbf{e}_y. \quad (4.45)$$

Approximation of the plane wave with temporal envelope is sufficient for this particular case. The electron trajectory is described by analytical equations (2.28) introduced earlier. As the laser pulse is of finite length, a_0 is replaced by the factor which involves also the temporal envelope of the pulse $a_0 f(t) = a_0 \exp \left[-2 \ln 2 \frac{(x - ct)^2}{c^2 \tau^2} \right]$ in equations (2.28). As it can be derived from these equations, the electron performs rapid oscillations from $\gamma = 1$ up to $\gamma = 1 + a_0^2/2$ for each half period of its motion along the straight line segment. As an illustration, electron trajectory for $a_0 = 8$ and $\tau = 15$ fs is plotted in Figure 4.12. Contrary to the case of betatron radiation, the emitted radiation dominantly originates from the longitudinal acceleration and deceleration.

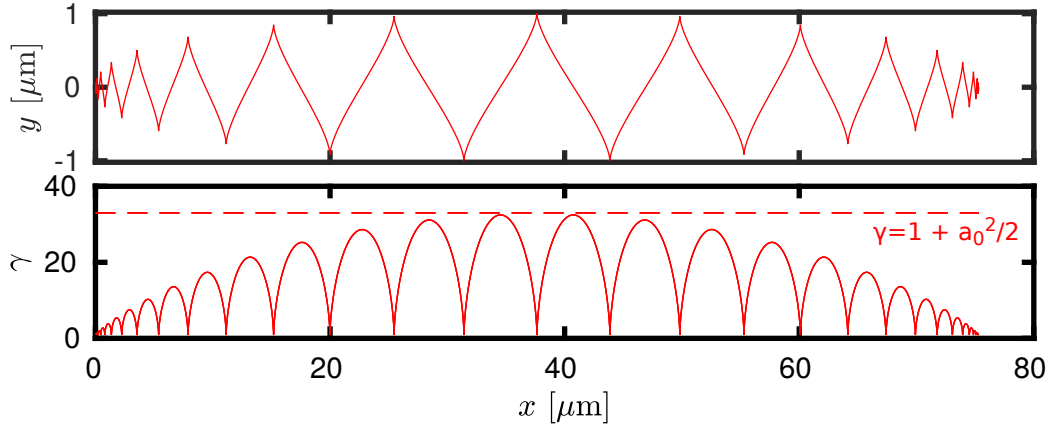


Figure 4.12: Electron trajectory for nonlinear Thomson scattering with $a_0 = 8$, $\tau = 15$ fs.

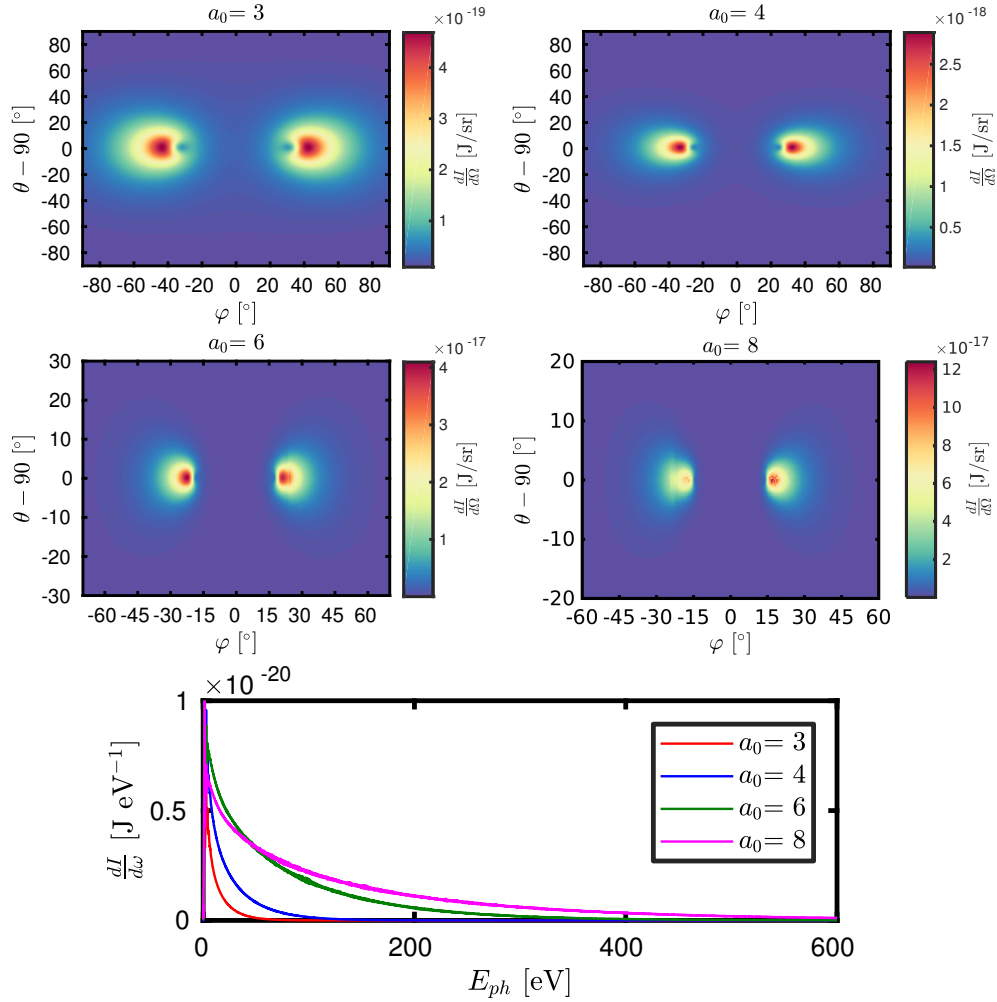


Figure 4.13: Angular distribution of nonlinear Thomson scattering and its energy spectra for $a_0 = [3, 4, 5, 8]$, $\tau = 25$ fs, and $\lambda_L = 0.8 \mu\text{m}$. Angles φ and θ correspond to standard spherical coordinates, i.e. $\varphi = \arctan \frac{y}{x}$, $\theta = \arccos \frac{z}{\sqrt{x^2 + y^2 + z^2}}$.

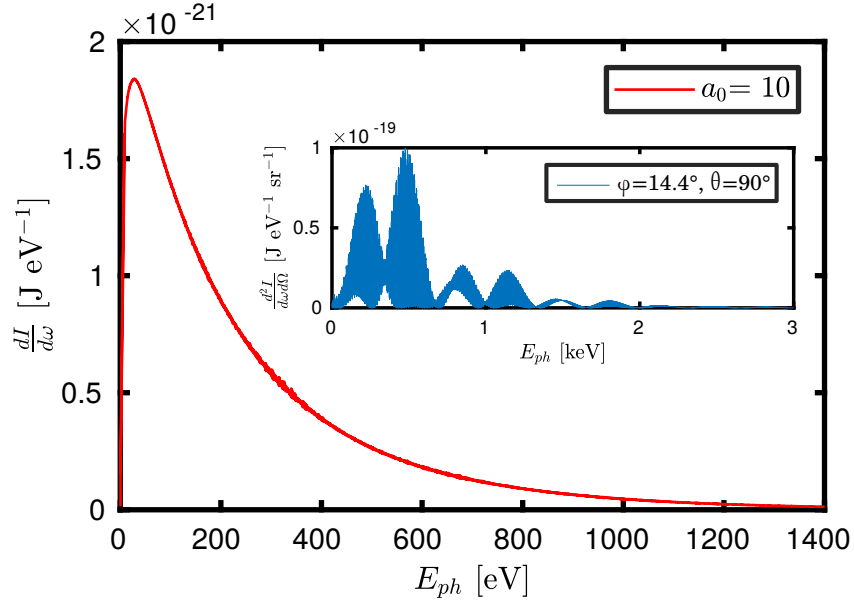


Figure 4.14: Energy spectrum of nonlinear Thomson scattering for $a_0 = 10$, $\tau = 25$ fs, and $\lambda_L = 0.8$ μm . Inset: radiation in the peak direction.

The radiation features were calculated by inserting these trajectories into equation (4.18). The angular and energy spectra were obtained by integration of these results over ω and Ω , respectively.

Several numerical results of nonlinear Thomson scattering are shown in Figure 4.13. Angular spectra consist of two dominant radiation peaks which correspond to the direction of the straight line segment of the electron trajectory. Energy of radiated photons is relatively low; the spectrum tail ends at ≈ 60 eV for $a_0 = 3$ or at ≈ 600 eV for $a_0 = 8$.

Figure 4.14 shows the energy spectrum of nonlinear Thomson scattering for $a_0 = 10$. The spectrum extends up to 2 keV. Its structure in the direction of dominant radiation emission is complex. It is a consequence of the characteristics of the electron motion [Lee et al., 2003, Corde et al., 2013].

Table 4.2 compares the basic characteristics of nonlinear Thomson scattering as total radiated energy per electron and the position of the radiation peak in dependence on the laser strength parameter. Each electron radiates a relatively low amount of energy, only in order of tens of electronvolts. Nevertheless, anticipating that each electron in the interaction volume contributes to the emission, total radiated energy can be satisfactorily high (10^{-4} – 10^{-2} photons per electron was reported in early experiments [Chen et al., 1998a, Banerjee et al., 2002], and there can be 10^{11} electrons in the interaction volume of ≈ 10 $\mu\text{m} \times 10$ $\mu\text{m} \times 500$ μm with electron density of $\approx 10^{18}$ cm^{-3}). The angle of dominant radiation direction decreases as laser strength grows.

| a_0 | radiated energy [eV/el] | peak position [°] |
|-------|-------------------------|-------------------|
| 3 | 2.65 | 42.6 |
| 4 | 6.41 | 32.7 |
| 6 | 20.7 | 21.8 |
| 8 | 27.8 | 16.8 |
| 10 | 39.2 | 14.6 |

Table 4.2: Properties of nonlinear Thomson scattering for a laser pulse with $a_0 = 10$, $\tau = 25$ fs, and $\lambda_L = 0.8$ μm .

It is important to point out that results of a single electron interacting with the plane wave presented above cannot be directly generalized to the achievable tightly focused laser pulses. As it can be seen from Figure 2.4, off-axis electrons are expelled from the interaction volume due to the ponderomotive force. Thus, they perform less number of oscillations; therefore they radiate less. Additionally, as these electrons gain significant transverse momenta, the peak structure of the angular distribution pattern is compromised. Other effects which may influence the electron trajectories should be considered. These are (i) the presence of ions and (ii) the fact that the laser group velocity is smaller than c in plasma and electrons may even overtake the laser pulse.

Indeed, the experimental results [Ta Phuoc et al., 2005] for similar parameters ($a_0 = 5$, $\tau = 30$ fs) as presented here report maximum radiation intensity on axis. It shows that this topic is very complex and requires a complex treatment. Currently, author and his colleagues are working on the more accurate method to calculate the angular spectra of nonlinear scattering, which considers all the aforementioned issues. This method will be based on tracking of the electron trajectories from PIC simulation and further post-processing by the radiation code. Its future findings may be applied not only to determine the radiation features but also as a diagnostics tool of the ultrashort tightly focused laser pulses.

4.3.2 Thomson backscattering

In Thomson backscattering configuration, electrons are first accelerated and subsequently wiggled by the counter-propagating laser wave. This scheme was proposed already in 1963 [Arutyunian and Tumanian, 1963, Milburn, 1963]. In this work, only the LWFA acceleration mechanism will be considered. Such an approach was at first suggested in [Catravas et al., 2001]; it leads to a rediscovery of the whole concept. Two intense laser pulses are considered. The first one drives the laser wakefield accelerator; the second one

is responsible for the scattering of the accelerated electrons.

Thomson backscattering can be thought of as a linear or nonlinear Thomson scattering from the previous section in the inertial frame co-moving with the average electron velocity. The Lorentz equation of the electron motion can be solved in such a frame with the laser fields transformed into this frame. The resulting trajectories can be used for the calculation of the radiation properties. This radiation is then once again transformed back to the laboratory frame by another Lorentz transform.

This double Compton down-shift in wavelength results in significant increase in the photon energy. A head-on collision of electron and laser is the most effective approach from this perspective. As the scattered photon actually gains energy, this process is often called *inverse Compton scattering*, contrary to standard Compton scattering, where scattered photon transfers part of its energy to the electron. In the linear or moderately nonlinear regime, the mean energy of the generated photons can be estimated as [Corde et al., 2013, Sarri et al., 2014]

$$E_{ph} = 4\gamma_e^2 \hbar\omega_L f(a_0), \quad (4.46)$$

where $f(a_0) \approx 1$ for $a_0 \ll 1$ and $f(a_0) \approx a_0$ for $a_0 \geq 1$ [Corde et al., 2013]. It means that when the initial 1.55 eV photon is scattered by the 150 MeV electron, the maximum energy of the scattered photon reaches 534 keV. 500 MeV electrons colliding with laser beam with $a_0 = 2$ may generate 18 MeV photons, as it was reported in experiment [Sarri et al., 2014].

The idea of the Thomson backscattering was simplified [Ta Phuoc et al., 2012] by using the plasma mirror to reflect the laser pulse which drives the laser wakefield accelerator. The plasma mirror is realized by a foil placed orthogonally to the axis of laser beam propagation in the place, where the trapped electrons are already sufficiently accelerated. Reflected laser pulse makes the electrons wiggle with a shorter wavelength than their betatron oscillation wavelength and therefore emit hard X-rays.

Two illustrative electron trajectories are plotted in Figure 4.15. These were calculated by the numerical integration of the motion equation of electron in the laboratory frame. The electron is moving in the negative direction along the x -axis, laser pulse arrives from the opposite direction. The laser pulse is again approximated as a plane wave according to equation (4.45). Such an approximation is quite natural in this case, as the transverse shift of the electrons due to the ponderomotive force of the laser pulse is negligible thanks to their large longitudinal momentum. The resulting trajectory is sine-like, contrary to the case of the nonlinear Thomson scattering.

The electron is wiggled by the counter-propagating laser pulse only during the short time of their interaction. The amplitude of such transverse oscillations is only a few

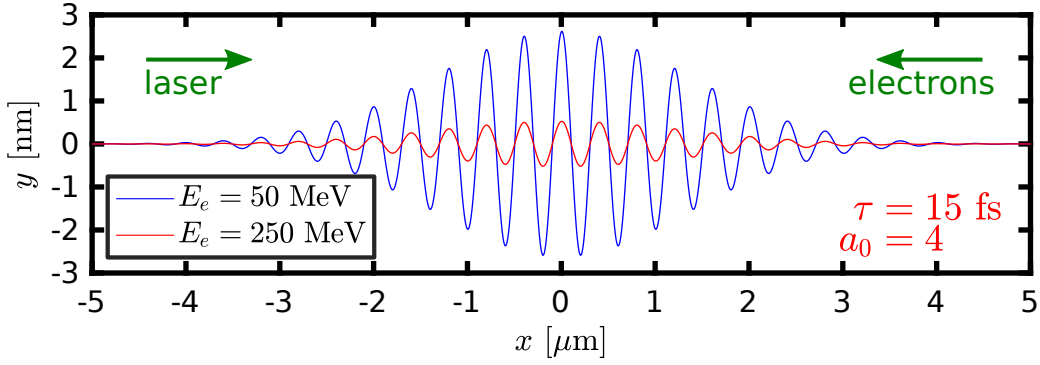


Figure 4.15: Electron trajectory for Thomson backscattering. Calculated numerically.

nanometers for standard parameters of both laser pulse and electron. The wavelength of the transverse oscillations is $\lambda_L/2$. The amplitude of these oscillations declines as the electron energy grows. For parameters of Figure 4.15, the pulse lengths emitted by a single electron calculated according to equation (4.26) is 4.60 as and 0.19 as for 50 MeV and 250 MeV electrons, respectively. Such lengths are extremely short. Thus, the total X-ray pulse length generated by Thomson backscattering is determined exclusively by the length of the electron bunch, as it is in order of femtoseconds.

The radiation is once again calculated using the Fourier approach represented by equation 4.18. The angular distribution of the radiated power for several typical parameters

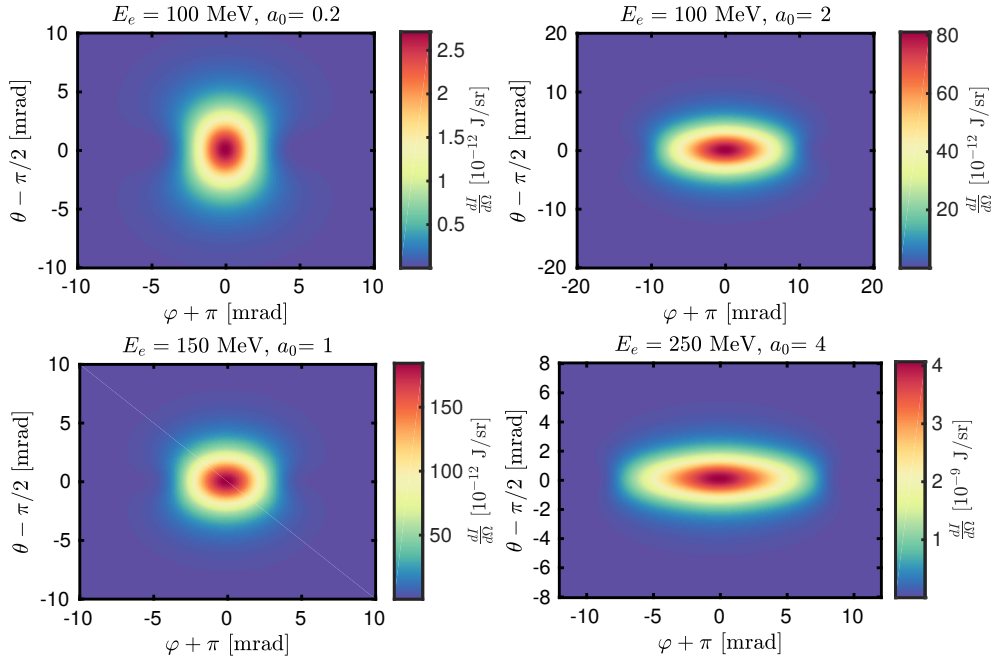


Figure 4.16: Spatial distribution of Thomson backscattering.

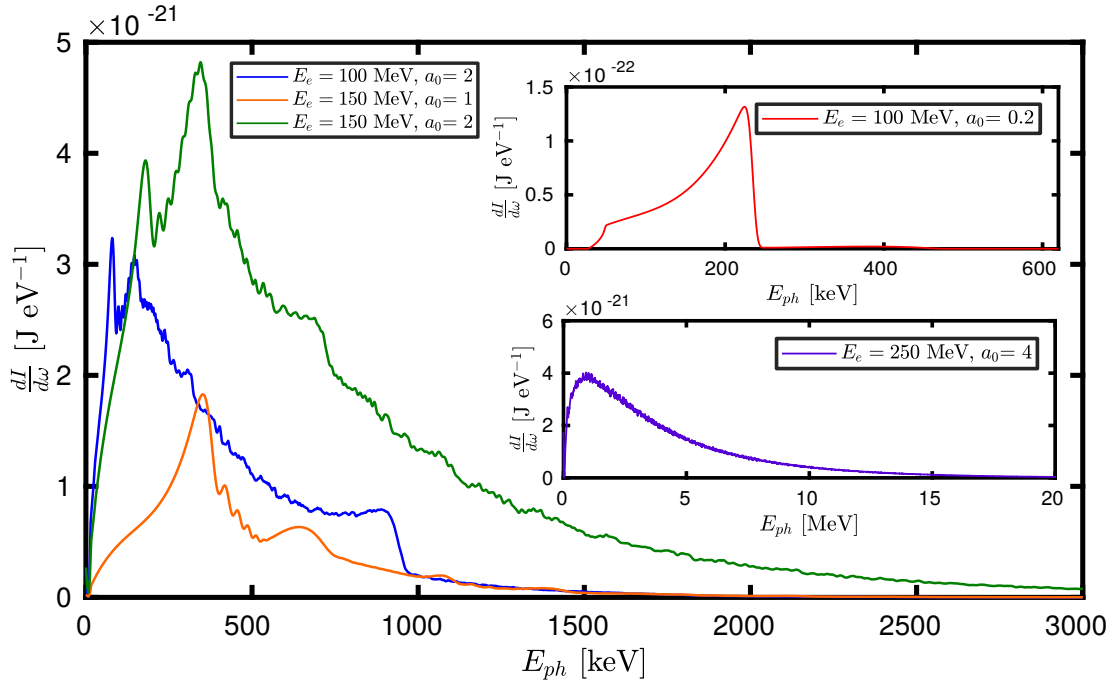


Figure 4.17: Energy spectrum of Thomson backscattering.

is shown in Figure 4.16. The radiation cone points along the axis in the direction of the electron velocity. The literature [Corde et al., 2013] claims that the radiation is collimated into the typical cone with the opening angle $\Delta\varphi = \Delta\theta = 1/\gamma$ for $a_0 \ll 1$ and $\Delta\varphi = a_0/\gamma$ and $\Delta\theta = 1/\gamma$ for $a_0 \gg 1$.

Energy spectra of Thomson backscattering are plotted in Figure 4.17. The radiation is much more energetic than in the case of the nonlinear Thomson scattering with the electron at rest. Hard X-rays with the radiation peak of 224 keV and with the total energy of 0.467 keV per electron are emitted even for the modest laser and electron parameters as $a_0 = 0.2$ and $E_e = 100$ MeV. As the laser intensity and/or electron energy grow, more energetic X-rays are generated, and also in a greater amount. The spectrum shape is synchrotron-like for $a \gg 1$. In the case of $E_e = 250$ MeV and $a_0 = 4$, which can be achieved with current 100TW laser systems, the critical energy of the synchrotron spectrum is 4.44 MeV. The properties of the generated X-rays for few parameter configurations are compared in Table 4.3.

Thomson backscattering is a very promising source of hard X-rays. The all-optical configuration, i.e. the case when electrons are both accelerated and wiggled by the intense laser pulse, could be potentially a very efficient and accessible tool for numerous applications in the fundamental research, industry, or medicine. In principle, only sub-100TW laser systems are required to deliver even 100MeV photons. The stability and the

| E_e [MeV] | a_0 | radiated energy [keV/el] | $\Delta\varphi$ [mrad] | $\Delta\theta$ [mrad] |
|-------------|-------|--------------------------|------------------------|-----------------------|
| 100 | 0.2 | 0.467 | 3.5 | 5.3 |
| 100 | 2 | 48.6 | 12.3 | 6.1 |
| 150 | 1 | 27.3 | 5.5 | 4.0 |
| 150 | 2 | 109 | 8.5 | 4.1 |
| 250 | 4 | 753 | 10.6 | 2.7 |

Table 4.3: Characteristics of Thomson backscattering.

tunability of the generated X-rays is the critical issue which currently limits the practical applications. These features are determined by the properties of the accelerated electron bunch.

Within this dissertation, the two novel optical injection schemes were suggested in order to optimize and stabilize the accelerated electron bunches. Such schemes could be used together with the third laser pulse propagating in the opposite direction. A stable electron bunches would then deliver stable X-ray photons of the superb characteristics.

4.4 Synchrotron radiation

Synchrotron radiation can be also generated from laser plasma accelerated electrons wiggled in the conventional undulator. Electrons are firstly accelerated in an underdense target and later delivered to the meter-scale-size undulator. Contrary to betatron source, the wavelength of the transverse oscillations is in a cm-range. Thus, GeV class electron bunches are necessary to generate radiation in X-ray energy range.

Nevertheless, this approach still represents a possible path toward the free electron laser based on the electrons accelerated in laser plasmas [Grüner et al., 2007]. In the shorter term, this method might be also used to the generation of extreme ultraviolet light or soft X-rays at university-scale laboratories [Corde et al., 2013].

The K parameter is given as [Corde et al., 2013]

$$K = \frac{eB_0}{k_u m_e c}, \quad (4.47)$$

where B_0 is the magnetic field amplitude, $k_u = 2\pi/\lambda_u$, and λ_u is an undulator period. The radiation energy depends on K parameter. For $K \ll 1$, single harmonic with the energy

$$\hbar\omega = \frac{2\gamma^2 hc}{\lambda_u(1 + K^2/2)} \quad (4.48)$$

is emitted. For $K \gg 1$, the spectrum is comprised of many closely spaced harmonics and can be characterized by critical energy

$$\hbar\omega_c = K \frac{3}{2} \gamma^2 \frac{hc}{\lambda_u}. \quad (4.49)$$

4.5 Other radiation sources

Few alternative approaches to generate X-rays from laser plasma without the use of any external manipulation techniques will be briefly introduced in this last section of chapter 4. These are K- α radiation from overdense targets, coherent soft X-rays as high order harmonics of the incident laser pulse interacting with the gaseous target, and a few considered implementations of free electron laser in laser plasmas.

4.5.1 K- α radiation

When laser with the intensity of the order of 10^{16} W/cm² or higher irradiates the solid target, the plasma is created in the interaction region and it expands back to the vacuum. Mechanisms like resonance absorption, vacuum heating, and $\mathbf{j} \times \mathbf{B}$ heating [Kruer, 1988] lead to the generation of hot electrons (their energy is of the order of tens or hundreds of keV, i.e. much higher than the energy corresponding to the plasma temperature). This process is illustrated in Figure 4.18. The hot electrons penetrate into the cold part of the target, which results, among other effects, in the ionization of the inner shells of atoms. As the relaxation periods of the ionized atoms with missing electron in the inner shell are very short, the atoms immediately proceed to the state with lower energy by two possible physical processes considered [Mewe, 1999].

Firstly, an electron from a higher shell can jump down into the empty inner shell. The energy released is carried away by another electron from the outer shell as its kinetic

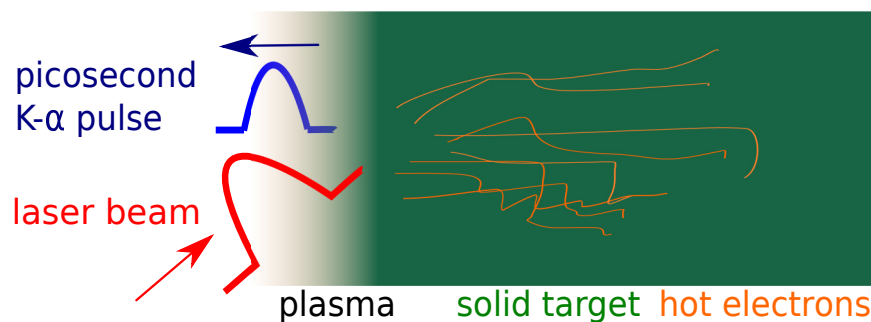


Figure 4.18: Scheme of K- α radiation source.

energy. This mechanism is called Auger effect and occurs rather for low Z elements. No radiation is emitted.

The second mechanism leads to the X-ray photon emission. The characteristic radiation is induced by the drop of the electron to the empty inner shell connected with the emission of the well-defined amount of energy in the form of a photon.

Individual electron shells are marked with Latin letters K, L, M etc. and depth of the drop is marked with the Greek letter α , β etc. The symbol K- α means that electron drops to the most inner K shell from the closest L shell. The typical energies of K- α lines are in order of keV (e.g. 1.49 keV for aluminum, 8.02 keV for copper, and 22.0 keV for silver).

Characteristic radiation has discrete line spectrum and positions of lines are unique for every individual chemical element. The disadvantage of the K- α sources is that the radiation is emitted to the angle of 4π steradians. Additionally, a significant part of the radiation is absorbed even before it leaves the solid target.

The phenomenon of the hot electron refluxing and its possible influence on K- α radiation was discussed in [Horný and Klimo, 2015]. Due to the strong electric field induced at the rear side of a thin target, the transmitted electrons are redirected back into the target, where they can initiate the processes leading to the excitation of the inner shells repetitively. It was found that these refluxing electrons increase the K- α radiation yield, as well as the duration of the X-ray pulse and the size of the radiation emitting area. A considerable increase in the number of the emitted K- α photons is observed especially for thin targets made of low- Z materials, and for higher hot electron temperatures. As an example result, electron refluxing must be considered for the aluminum foils which are narrower than 200 μm .

■ 4.5.2 High order harmonics radiation

High harmonic generation (HHG) is another nonlinear process during which a target is illuminated by an intense laser pulse. Laser intensities are of the order of 10^{14} W/cm², typically. Under such conditions, the sample will emit the high harmonics of the laser beam, typically up to the energy of hundreds of eV or units of keV. The electron is released from the atom by the multiphoton ionization; it immediately experiences the laser field. It starts to oscillate with the higher amplitude than the classical radius of an atom (Bohr radius). Some of the released electrons can, as the laser field direction reverses, return back to the parent ion, recombine there and emit single high frequency photon.

The emitted spectrum is comprised of the individual harmonics of the laser frequency.

It can be divided into three parts:

1. the region of lower harmonics with high intensity
2. plateau region where the intensities of neighbour harmonics are similar
3. and the high intensity region where the intensity of individual harmonics with the increasing harmonic number rapidly drops up to the position called harmonic cut-off.

The cut-off energy is given by

$$E_c = E_{ion} + 3.17E_p, \quad (4.50)$$

which was predicted in numerical simulations [Krause et al., 1992]. E_{ion} is the ionization energy and E_p is the ponderomotive potential the laser field, expressing the effective quiver energy acquired by an oscillating electron. It is given by

$$E_p = \frac{e^2 E_0^2}{4m_e \omega_L^2}, \quad (4.51)$$

where E_0 is the laser electric field.

HHG source provides tunable table top source of radiation on the border between extreme ultraviolet light and soft X-rays. The harmonic cut-off varies linearly with increasing laser intensity up to certain saturation intensity. High harmonics generation is used in the generation of attosecond pulses as well [Paul et al., 2001], because of its coherent nature (contrary to nonlinear Thomson scattering). The overview of the high harmonics generation physics is given in [Schultz and Vrakking, 2013].

4.5.3 Free electron laser from laser plasmas

A free electron laser (FEL) is a device, where the high energy electrons move through the structure, which wiggles their trajectories in a way that they become coherent and radiate coherently [Huang and Kim, 2007]. The energy range of the operated FELs ranges from microwaves up to X-rays. Current FELs use a conventional radiofrequency accelerator and an undulator which is actually a periodic arrangement of magnets with alternating poles across the beam path. Such an undulator may be very long (tens of meters).

As the electrons are wiggled in the undulator, the undulator radiation is emitted, similarly to the betatron source (cf. Figure 4.4). However, the radiation emitted by the whole bunch is incoherent and its intensity is proportional to N_e , because randomly distributed electrons interfere constructively and destructively in time.

An electron also experiences the radiation from other electrons in the bunch which modifies its motion and energy. Such an interaction between the bunch and its own

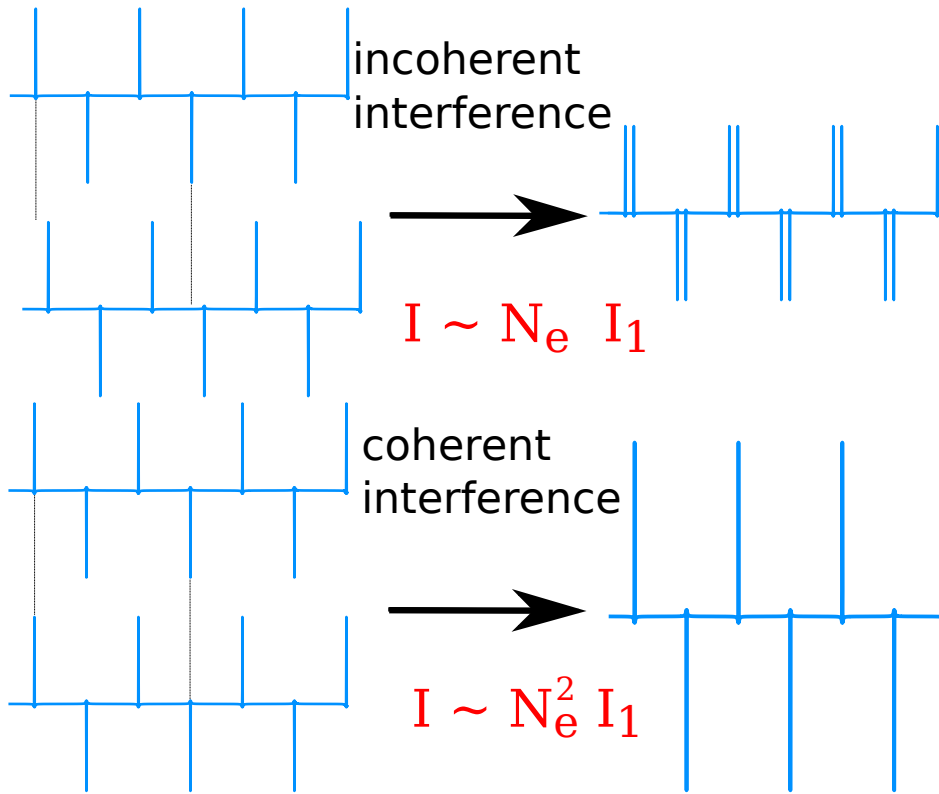


Figure 4.19: Incoherent and coherent summing of the signal. Blue structures illustrate the signal received by the observer.

radiation may lead to so-called *microbunching* at the fundamental wavelength of the radiation. When the bunch is microbunched, the radiation emitted by all the bunched electrons is in phase, and the fields interfere together coherently. The schematic illustration of the great effect of the constructive interference is shown in Figure 4.19.

In other words, the constructive interference occurs when the electron advances one undulator wavelength λ_u as the radiation field slips by the one radiation wavelength λ . Such condition can be written as

$$\lambda = \frac{\lambda_u}{2\gamma^2} \left(1 + \frac{K^2}{2} \right), \quad (4.52)$$

where K is the parameter defined in equation (4.28).

The radiated intensity is proportional to N_e^2 in FEL. However, this FEL effect requires very strict conditions on the electron beam quality. These conditions depend on the Pierce parameter [Bonifacio et al., 1984] and restrict the energy and energy spread of the electrons, propagation length, and the undulator characteristics. In previous sections, these conditions were not fulfilled and the FEL effect was not observed or taken even into an account.

Nevertheless, the generation of coherent X-rays from laser plasmas is an intensively researched topic nowadays. Three mechanisms to achieve microbunching in laser plasma without using any external manipulation will be briefly discussed. They are complementary to the use of the standard undulator after the LWFA acceleration in laser plasmas.

■ All-optical free electron laser

A head-on collision of the accelerated electrons and the laser beam (Thomson backscattering) may lead to FEL effect [Petrillo et al., 2008] under certain circumstances. As it was shown in Section 4.3.2, the undulator period is $\lambda_u = \lambda_L/2$. Currently, the use of relatively slow electron bunches (10 MeV) colliding with infrared CO₂ laser (10 μ m) is considered to obtain keV range coherent radiation. However, it forces high demands on the quality of the low energy electron beams which is (i) difficult and (ii) not investigated very often.

■ Ion channel laser

Ion channel laser is another approach to induce a FEL effect to the accelerated electron bunches. This method suggests introducing the microbunching already in the bubble during LWFA [Whittum et al., 1990]. Such a treatment assumes that it is possible to prepare the conditions when the electrons sustain a constant energy inside the bubble. This could be achieved for instance by forwarding them to the center of the bubble where longitudinal accelerating field vanishes with the forward momentum which corresponds to the wake wave phase velocity. Additionally, all the electrons must oscillate in the same plane and with the same amplitude. It is extensively difficult to achieve such conditions in an experiment.

■ All optical FEL by copropagating laser pulse

Recently, a new scheme of free electron laser from electron bunched accelerated in laser plasma was suggested [Steiniger et al., 2016]. Laser pulse representing an undulator crosses the electron bunch accelerated by LWFA under the small angle. Electrons and the laser pulse then co-propagate together for a relatively long distance, even in order of centimeters. In the frame comoving with the average electron velocity, this configuration represents a Thomson scattering with the laser pulse wavelength prolonged by the Doppler shift. Electron bunches with the energy spread lower than 1 % and normalized emittance lower than 0.2 π -mm-mrad are required to implement this mechanism.



Chapter 5

Conclusion

This dissertation is devoted to the generation of hard X-rays from relativistic electrons accelerated by laser wakefield acceleration mechanism. More specifically, X-ray sources which can be implemented with the currently available 100-TW class laser systems were investigated. Such sources are based on the wiggling of the trajectories of accelerated electrons. Once they become established, these sources will represent a conceptual upgrade in the features of delivered X-rays, as their size is as low as few microns and pulses with lengths in order of femtoseconds are generated. Moreover, such a small source size enables X-ray phase-contrast imaging, a technique which significantly enhances the resolution of sampled images in comparison with standard absorption radiography. Furthermore, femtosecond pulse length enables to sample fundamental physical processes, such as chemical reactions, phase transitions, lattice vibrations or spin dynamics, which can induce a significant progress in other scientific disciplines.

However, X-ray sources from laser plasma cannot yet compete with conventional sources based on synchrotrons and undulators, mainly because of their questionable stability, reproducibility, and tunability. These properties are still unsatisfactory for expected applications in fundamental research, industry, or health care.

The features of the generated X-ray pulses are set by the quality of accelerated electron beams. The injection of the electron bunch into an accelerating phase of a plasma wave is presumably the most important process which determines its final properties, such as the energy spread or the emittance. Therefore, two novel optical injection schemes were proposed. They belong to significant results of this dissertation. Both these schemes of the injection by the perpendicular and by the preceding weaker pulse provide a high charge (tens of pC) and short length (fs) electron bunches. This is advantageous for the generation of short and relatively intense X-ray pulses by mechanisms of betatron radiation and Thomson backscattering.

In the first scheme, the injection pulse is intended to be directed orthogonally with

respect to the main beam propagation direction; the polarization vectors of both pulses are in the plane of both beams propagation. This scheme can be employed for instance in relatively low-density plasmas ($n_e \approx 2\text{--}5 \times 10^{18} \text{ cm}^{-3}$) and with moderate laser intensities ($a_0 \leq 5$), where electrons can be accelerated to energies of hundreds of MeV. Also, a possible delayed self-injection does not influence the features of optically injected electron bunches under these conditions. This introduced method is based on the characteristic nature of the electron motion in the field of laser colliding pulses. Additionally, the accelerating plasma wave is almost undisturbed by the injection pulse which is beneficial for the acceleration process.

The second scheme uses similar laser and plasma parameters like the aforementioned one. It is inspired by a standard self-injection. The injection pulse precedes the main plasma wave drive pulse by approximately one plasma period. The parameters of this injection pulse and following main pulse are the same but intensity. The scheme also provides stable generation of quasimonoenergetic high charge electron bunches accelerated to hundreds-MeV energies. The main advantage of this scheme is its simplicity in comparison with all alternative optical injection schemes. The idea of injection is based on the geometrical approach, and on the wave-breaking on up-ramp-plateau density transition. The experimental tests of both optical injection schemes are planned at the PALS laser center in Prague in autumn 2018.

Another significant result of this dissertation is a new method to calculate the properties of the betatron radiation and even to construct its spectrograms. The method is based on the theory of retarded potentials which are calculated from the trajectories of accelerated electrons. It takes advantage of the fact that the electron oscillates transversally in the accelerating plasma wave in the wiggler regime and, thus, emits radiation almost exclusively in the turning points of its sine-like trajectory. Therefore, there are only a few very narrow time intervals, which contribute significantly to the emission of radiation, while the rest can be neglected. It reduces significantly the memory demands. In principle, the betatron radiation features can be determined from the given laser pulse and plasma parameters combining this method with particle-in-cell simulations of laser wakefield acceleration.

We believe that our method represents a useful tool to investigate or to tailor the betatron X-ray pulse temporal profiles and it can be used to design sources for future applications such as probing of ultrafast fundamental physical processes.



Bibliography

- [Amiranoff et al., 1998] Amiranoff, F., Baton, S., Bernard, D., Cros, B., Descamps, D., Dorchies, F., Jacquet, F., Malka, V., Marques, J., Matthieussent, G., et al. (1998). Observation of laser wakefield acceleration of electrons. *Physical Review Letters*, 81(5):995.
- [Ammosov et al., 1986] Ammosov, M., Delone, N. B., Krainov, V. P., et al. (1986). Tunnel ionization of complex atoms and of atomic ions in an alternating electromagnetic field. *Soviet Physics - Journal of Experimental and Theoretical Physics*, 64(6):1191–1194.
- [Andreev et al., 2011] Andreev, A. A., Galkin, A. L., Kalashnikov, M. P., Korobkin, V. V., Romanovsky, M. Y., and Shiryaev, O. B. (2011). Electrons in a relativistic-intensity laser field: generation of zeptosecond electromagnetic pulses and energy spectrum of the accelerated electrons. *Quantum Electronics*, 41:729–734.
- [Arber et al., 2015] Arber, T., Bennett, K., Brady, C., Lawrence-Douglas, A., Ramsay, M., Sircombe, N., Gillies, P., Evans, R., Schmitz, H., Bell, A., et al. (2015). Contemporary particle-in-cell approach to laser-plasma modelling. *Plasma Physics and Controlled Fusion*, 57(11):113001.
- [Arutyunian and Tumanian, 1963] Arutyunian, F. and Tumanian, V. (1963). The Compton effect on relativistic electrons and the possibility of obtaining high energy beams. *Physics Letters*, 4(3):176–178.
- [Attwood, 2007] Attwood, D. (2007). *Soft x-rays and extreme ultraviolet radiation: principles and applications*. Cambridge university press.
- [Attwood and Sakdinawat, 2017] Attwood, D. and Sakdinawat, A. (2017). *X-rays and extreme ultraviolet radiation: principles and applications*. Cambridge university press.

- [Banerjee et al., 2002] Banerjee, S., Valenzuela, A., Shah, R., Maksimchuk, A., and Umstadter, D. (2002). High harmonic generation in relativistic laser–plasma interaction. *Physics of Plasmas*, 9(5):2393–2398.
- [Barber et al., 2017] Barber, S., van Tilborg, J., Schroeder, C., Lehe, R., Tsai, H.-E., Swanson, K., Steinke, S., Nakamura, K., Geddes, C., Benedetti, C., et al. (2017). Measured emittance dependence on the injection method in laser plasma accelerators. *Physical Review Letters*, 119(10):104801.
- [Bellan, 2008] Bellan, P. M. (2008). *Fundamentals of plasma physics*. Cambridge University Press.
- [Benedetti et al., 2013] Benedetti, C., Schroeder, C., Esarey, E., Rossi, F., and Leemans, W. (2013). Numerical investigation of electron self-injection in the nonlinear bubble regime. *Physics of Plasmas*, 20(10):103108.
- [Berezhiani and Murusidze, 1992] Berezhiani, V. and Murusidze, I. (1992). Interaction of highly relativistic short laser pulses with plasmas and nonlinear wake-field generation. *Physica Scripta*, 45(2):87.
- [Bethe and Salpeter, 2012] Bethe, H. A. and Salpeter, E. E. (2012). *Quantum mechanics of one-and two-electron atoms*. Springer Science & Business Media.
- [Bloembergen, 1999] Bloembergen, N. (1999). From nanosecond to femtosecond science. *Reviews of Modern Physics*, 71(2):S283.
- [Boháček et al., 2018] Boháček, K., Kozlová, M., Nejd, J., Chaulagain, U., Horný, V., Krůs, M., and Ta Phuoc, K. (2018). Stable electron beams from laser wakefield acceleration with few-terawatt driver using a supersonic air jet. *Nuclear Instruments and Methods in Physics Research Section A: Accelerators, Spectrometers, Detectors and Associated Equipment*, 883:24–28.
- [Bonifacio et al., 1984] Bonifacio, R., Pellegrini, C., and Narducci, L. (1984). Collective instabilities and high-gain regime free electron laser. In *AIP Conference Proceedings*, volume 118(1), pages 236–259. AIP.
- [Borisov et al., 1994] Borisov, A., Shi, X., Karpov, V., Korobkin, V., Solem, J., Shiryayev, O., McPherson, A., Boyer, K., and Rhodes, C. (1994). Stable self-channeling of intense ultraviolet pulses in underdense plasma, producing channels exceeding 100 Rayleigh lengths. *Journal of the Optical Society of America B*, 11(10):1941–1947.

- [Bourgeois et al., 2013] Bourgeois, N., Cowley, J., and Hooker, S. M. (2013). Two-pulse ionization injection into quasilinear laser wakefields. *Physical Review Letters*, 111(15):155004.
- [Brantov et al., 2008] Brantov, A., Esirkepov, T. Z., Kando, M., Kotaki, H., Bychenkov, V. Y., and Bulanov, S. (2008). Controlled electron injection into the wake wave using plasma density inhomogeneity. *Physics of Plasmas*, 15(7):073111.
- [Bulanov et al., 2016] Bulanov, S., Esirkepov, T. Z., Hayashi, Y., Kiriya, H., Koga, J., Kotaki, H., Mori, M., and Kando, M. (2016). On some theoretical problems of laser wake-field accelerators. *Journal of Plasma Physics*, 82(3).
- [Bulanov et al., 1989] Bulanov, S., Kirsanov, V., and Sakharov, A. (1989). Excitation of ultrarelativistic plasma waves by pulse of electromagnetic radiation. *Journal of Experimental and Theoretical Physics Letters*, 50(0):4–25.
- [Bulanov et al., 1998] Bulanov, S., Naumova, N., Pegoraro, F., and Sakai, J. (1998). Particle injection into the wave acceleration phase due to nonlinear wake wave breaking. *Physical Review E*, 58(5):R5257.
- [Buon, 1994] Buon, J. (1994). Beam phase space and emittance. *CERN European Organization for Nuclear Research-Reports*, pages 89–89.
- [Catravas et al., 2001] Catravas, P., Esarey, E., and Leemans, W. (2001). Femtosecond x-rays from Thomson scattering using laser wakefield accelerators. *Measurement Science and Technology*, 12(11):1828.
- [Chapman et al., 2011] Chapman, H. N., Fromme, P., Barty, A., White, T. A., Kirian, R. A., Aquila, A., Hunter, M. S., Schulz, J., DePonte, D. P., Weierstall, U., et al. (2011). Femtosecond X-ray protein nanocrystallography. *Nature*, 470(7332):73–77.
- [Chen et al., 2013] Chen, M., Esarey, E., Geddes, C. G. R., Schroeder, C. B., Plateau, G. R., Bulanov, S. S., Rykovanov, S., and Leemans, W. P. (2013). Modeling classical and quantum radiation from laser-plasma accelerators. *Physical Review Special Topics - Accelerators and Beams*, 16(3).
- [Chen et al., 2012a] Chen, M., Esarey, E., Schroeder, C., Geddes, C., and Leemans, W. (2012a). Theory of ionization-induced trapping in laser-plasma accelerators. *Physics of Plasmas*, 19(3):033101.
- [Chen et al., 2012b] Chen, M., Geddes, C., Esarey, E., Schroeder, C., Bulanov, S., Benedetti, C., Yu, L., Rykovanov, S., Leemans, W., Cormier-Michel, E., et al. (2012b).

- Using transverse colliding-pulse injection to obtain electron beams with small emittance in a laser-plasma accelerator. In *AIP Conference Proceedings*, volume 1507(1), pages 262–266. AIP.
- [Chen et al., 1998a] Chen, S.-Y., Maksimchuk, A., and Umstadter, D. (1998a). Experimental observation of relativistic nonlinear Thomson scattering. *Nature*, 396(6712):653.
- [Chen et al., 1998b] Chen, S.-Y., Sarkisov, G., Maksimchuk, A., Wagner, R., and Umstadter, D. (1998b). Evolution of a plasma waveguide created during relativistic-ponderomotive self-channeling of an intense laser pulse. *Physical Review Letters*, 80(12):2610.
- [Corde et al., 2011] Corde, S., Stordeur, A., and Malka, V. (2011). Comment on “Scalings for radiation from plasma bubbles”[Phys. Plasmas 17, 056708 (2010)]. *Physics of Plasmas*, 18(3):034701.
- [Corde et al., 2013] Corde, S., Ta Phuoc, K., Lambert, G., Fitour, R., Malka, V., Rousse, A., Beck, A., and Lefebvre, E. (2013). Femtosecond X-rays from laser-plasma accelerators. *Reviews of Modern Physics*, 85(1):1.
- [Couperus et al., 2017] Couperus, J., Pausch, R., Köhler, A., Zarini, O., Krämer, J., Garten, M., Huebl, A., Gebhardt, R., Helbig, U., Bock, S., et al. (2017). Demonstration of a beam loaded nanocoulomb-class laser wakefield accelerator. *Nature Communications*, 8(1):487.
- [Davoine et al., 2008] Davoine, X., Lefebvre, E., Faure, J., Rechatin, C., Lifschitz, A., and Malka, V. (2008). Simulation of quasimonoenergetic electron beams produced by colliding pulse wakefield acceleration. *Physics of Plasmas*, 15(11):113102.
- [Davoine et al., 2009] Davoine, X., Lefebvre, E., Rechatin, C., Faure, J., and Malka, V. (2009). Cold optical injection producing monoenergetic, multi-GeV electron bunches. *Physical Review Letters*, 102(6):065001.
- [Dodd et al., 2004] Dodd, E., Kim, J., and Umstadter, D. (2004). Simulation of ultrashort electron pulse generation from optical injection into wake-field plasma waves. *Physical Review E*, 70(5):056410.
- [Dodd et al., 1997] Dodd, E., Kim, J., Umstadter, D., Chattopadhyay, S., McCullough, J., and Dahl, P. (1997). Ultrashort-pulse relativistic electron gun/accelerator. In *AIP Conference Proceedings*, volume 398, pages 106–115. AIP.

- [Dubietis et al., 1992] Dubietis, A., Jonušauskas, G., and Piskarskas, A. (1992). Powerful femtosecond pulse generation by chirped and stretched pulse parametric amplification in bbo crystal. *Optics Communications*, 88(4-6):437–440.
- [Esarey et al., 1997] Esarey, E., Hubbard, R., Leemans, W., Ting, A., and Sprangle, P. (1997). Electron injection into plasma wakefields by colliding laser pulses. *Physical Review Letters*, 79(14):2682.
- [Esarey et al., 1994] Esarey, E., Krall, J., and Sprangle, P. (1994). Envelope analysis of intense laser pulse self-modulation in plasmas. *Physical Review Letters*, 72(18):2887.
- [Esarey and Pilloff, 1995] Esarey, E. and Pilloff, M. (1995). Trapping and acceleration in nonlinear plasma waves. *Physics of Plasmas*, 2(5):1432–1436.
- [Esarey et al., 2009] Esarey, E., Schroeder, C., and Leemans, W. (2009). Physics of laser-driven plasma-based electron accelerators. *Reviews of Modern Physics*, 81(3):1229.
- [Esarey et al., 2002] Esarey, E., Shadwick, B., Catravas, P., and Leemans, W. (2002). Synchrotron radiation from electron beams in plasma-focusing channels. *Physical Review E*, 65(5):056505.
- [Esarey et al., 1996] Esarey, E., Sprangle, P., Krall, J., and Ting, A. (1996). Overview of plasma-based accelerator concepts. *IEEE Transactions on Plasma Science*, 24(2):252–288.
- [Esarey et al., 1989] Esarey, E., Ting, A., Sprangle, P., and Joyce, G. (1989). The laser wakefield accelerator. *Comments on Plasma Physics and Controlled Fusion*, 12(4):191–204.
- [Faure, 2016] Faure, J. (2016). Plasma Injection Schemes for Laser – Plasma Accelerators. *Proceedings of the CAS-CERN Accelerator School: Plasma Wake Acceleration*, 1(November 2014):143.
- [Faure et al., 2004] Faure, J., Glinec, Y., Pukhov, A., Kiselev, S., Gordienko, S., Lefebvre, E., Rousseau, J.-P., Burgy, F., and Malka, V. (2004). A laser–plasma accelerator producing monoenergetic electron beams. *Nature*, 431(7008):541.
- [Faure et al., 2010] Faure, J., Rechatin, C., Lundh, O., Ammoura, L., and Malka, V. (2010). Injection and acceleration of quasimonoenergetic relativistic electron beams using density gradients at the edges of a plasma channel. *Physics of Plasmas*, 17(8):083107.

- [Faure et al., 2006] Faure, J., Rechatin, C., Norlin, A., Lifschitz, A., Glinec, Y., and Malka, V. (2006). Controlled injection and acceleration of electrons in plasma wakefields by colliding laser pulses. *Nature*, 444(7120):737–739.
- [Fessler and Sutton, 2003] Fessler, J. A. and Sutton, B. P. (2003). Nonuniform fast Fourier transforms using min-max interpolation. *Signal Processing, IEEE Transactions on*, 51(2):560–574.
- [Floettmann, 2003a] Floettmann, K. (2003a). Erratum: Some basic features of the beam emittance [Phys. Rev. ST Accel. Beams 6, 034202 (2003)]. *Physical Review Special Topics-Accelerators and Beams*, 6(7):079901.
- [Floettmann, 2003b] Floettmann, K. (2003b). Some basic features of the beam emittance. *Physical Review Special Topics-Accelerators and Beams*, 6(3):034202.
- [Fourmaux et al., 2011] Fourmaux, S., Corde, S., Ta Phuoc, K., Leguay, P., Payeur, S., Lassonde, P., Gnediyuk, S., Lebrun, G., Fourment, C., Malka, V., et al. (2011). Demonstration of the synchrotron-type spectrum of laser-produced betatron radiation. *New Journal of Physics*, 13(3):033017.
- [Froula et al., 2009] Froula, D., Clayton, C., Döppner, T., Marsh, K., Barty, C., Divol, L., Fonseca, R., Glenzer, S., Joshi, C., Lu, W., et al. (2009). Measurements of the critical power for self-injection of electrons in a laser wakefield accelerator. *Physical Review Letters*, 103(21):215006.
- [Fubiani et al., 2004] Fubiani, G., Esarey, E., Schroeder, C., and Leemans, W. (2004). Beat wave injection of electrons into plasma waves using two interfering laser pulses. *Physical Review E*, 70(1):016402.
- [Gahn et al., 1999] Gahn, C., Tsakiris, G., Pukhov, A., Meyer-ter Vehn, J., Pretzler, G., Thirolf, P., Habs, D., and Witte, K. (1999). Multi-MeV electron beam generation by direct laser acceleration in high-density plasma channels. *Physical Review Letters*, 83(23):4772.
- [Geddes et al., 2004] Geddes, C., Toth, C., Van Tilborg, J., Esarey, E., Schroeder, C., Bruhwiler, D., Nieter, C., Cary, J., and Leemans, W. (2004). High-quality electron beams from a laser wakefield accelerator using plasma-channel guiding. *Nature*, 431(7008):538.
- [Geddes et al., 2005] Geddes, C., Toth, C., Van Tilborg, J., Esarey, E., Schroeder, C., Bruhwiler, D., Nieter, C., Cary, J., and Leemans, W. (2005). Production of high-quality

- electron bunches by dephasing and beam loading in channeled and unchanneled laser plasma accelerators. *Physics of Plasmas*, 12(5):056709.
- [Gibbon, 2004] Gibbon, P. (2004). *Short pulse laser interactions with matter*. World Scientific Publishing Company.
- [Gorbunov and Kirsanov, 1987] Gorbunov, L. and Kirsanov, V. (1987). Excitation of plasma waves by an electromagnetic wave packet. *Soviet Physics - Journal of Experimental and Theoretical Physics*, 66(290-294):40.
- [Grassi et al., 2014] Grassi, A., Fedeli, L., Macchi, A., Bulanov, S. V., and Pegoraro, F. (2014). Phase space dynamics after the breaking of a relativistic Langmuir wave in a thermal plasma. *The European Physical Journal D*, 68(6):178.
- [Grüner et al., 2007] Grüner, F., Becker, S., Schramm, U., Eichner, T., Fuchs, M., Weingartner, R., Habs, D., Meyer-ter Vehn, J., Geissler, M., Ferrario, M., Serafini, L., van der Geer, B., Backe, H., Lauth, W., and Reiche, S. (2007). Design considerations for table-top, laser-based VUV and X-ray free electron lasers. *Applied Physics B*, 86(3):431–435.
- [Hartemann et al., 1995] Hartemann, F., Fochs, S., Le Sage, G., Luhmann Jr, N., Woodworth, J., Perry, M., Chen, Y., and Kerman, A. (1995). Nonlinear ponderomotive scattering of relativistic electrons by an intense laser field at focus. *Physical Review E*, 51(5):4833.
- [He et al., 2013] He, Z., Hou, B., Nees, J., Easter, J., Faure, J., Krushelnick, K., and Thomas, A. (2013). High repetition-rate wakefield electron source generated by few-millijoule, 30 fs laser pulses on a density downramp. *New Journal of Physics*, 15(5):053016.
- [Hemker et al., 1998] Hemker, R., Tzeng, K.-C., Mori, W., Clayton, C., and Katsouleas, T. (1998). Computer simulations of cathodeless, high-brightness electron-beam production by multiple laser beams in plasmas. *Physical Review E*, 57(5):5920.
- [Hemker, 2015] Hemker, R. G. (2015). Particle-in-cell modeling of plasma-based accelerators in two and three dimensions. *arXiv preprint arXiv:1503.00276*.
- [Hirose, 2011] Hirose, A. (2011). PHYS 812.3 - Electromagnetic Theory. <http://physics.usask.ca/~hirose/p812/p812fp.htm>. [Online; accessed 11-April-2016].

- [Horný and Klimo, 2015] Horný, V. and Klimo, O. (2015). Hot electron refluxing in the short intense laser pulse interactions with solid targets and its influence on K- α radiation. *Nukleonika*, 60(2):233–237.
- [Horný et al., 2018a] Horný, V., Klimo, O., and Krůs, M. (2018a). High charge plasma electron bunches from two collinear laser pulses. Submitted to Applied Physics Letters.
- [Horný and Krůs, 2017] Horný, V. and Krůs, M. (2017). Optical injection into the laser wakefield accelerator by co-propagating weaker pulse. In *Proceedings of the 44th EPS Conference on Plasma Physics*.
- [Horný et al., 2018b] Horný, V., Mašlářová, D., Petržílka, V., Klimo, O., Kozlová, M., and Krůs, M. (2018b). Optical injection dynamics in two laser wakefield acceleration configurations. *Plasma Physics and Controlled Fusion*, 60(6):064009.
- [Horný et al., 2017a] Horný, V., Nejd, J., Kozlová, M., Krůs, M., Boháček, K., Petržílka, V., and Klimo, O. (2017a). Temporal profile of betatron radiation from laser-driven electron accelerators. *Physics of Plasmas*, 24(6):063107.
- [Horný et al., 2017b] Horný, V., Petržílka, V., Klimo, O., and Krůs, M. (2017b). Short electron bunches generated by perpendicularly crossing laser pulses. *Physics of Plasmas*, 24(10):103125.
- [Horný et al., 2017c] Horný, V., Petržílka, V., Klimo, O., and Krůs, M. (2017c). Short energetic electron bunches from laser wakefield accelerator with orthogonally polarized perpendicularly crossed laser pulses. In *Laser Acceleration of Electrons, Protons, and Ions IV*, volume 10240, page 1024011. International Society for Optics and Photonics.
- [Hu et al., 2016] Hu, R., Lu, H., Shou, Y., Lin, C., Zhuo, H., Chen, C., and Yan, X. (2016). Brilliant GeV electron beam with narrow energy spread generated by a laser plasma accelerator. *Physical Review Accelerators and Beams*, 19(9):091301.
- [Huang and Kim, 2007] Huang, Z. and Kim, K.-J. (2007). Review of X-ray free-electron laser theory. *Physical Review Special Topics-Accelerators and Beams*, 10(3):034801.
- [Hubbell and Seltzer, 1995] Hubbell, J. H. and Seltzer, S. M. (1995). Tables of X-ray mass attenuation coefficients and mass energy-absorption coefficients 1 keV to 20 MeV for elements Z= 1 to 92 and 48 additional substances of dosimetric interest. Technical report, National Inst. of Standards and Technology-PL, Gaithersburg, MD (United States). Ionizing Radiation Div.
- [Jackson, 1999] Jackson, J. D. (1999). *Classical electrodynamics*. Wiley.

- [Jerri, 1977] Jerri, A. J. (1977). The Shannon sampling theorem — Its various extensions and applications: A tutorial review. *Proceedings of the IEEE*, 65(11):1565–1596.
- [Joshi et al., 1981] Joshi, C., Tajima, T., Dawson, J., Baldis, H., and Ebrahim, N. (1981). Forward raman instability and electron acceleration. *Physical Review Letters*, 47(18):1285.
- [Ju, 2013] Ju, J. (2013). *Electron acceleration and betatron radiation driven by laser wakefield inside dielectric capillary tubes*. PhD thesis, Université Paris Sud-Paris XI.
- [Kalmykov et al., 2009] Kalmykov, S., Yi, S., Khudik, V., and Shvets, G. (2009). Electron self-injection and trapping into an evolving plasma bubble. *Physical Review Letters*, 103(13):135004.
- [Katsouleas and Su, 1987] Katsouleas, S. W. T. and Su, J. D. J. (1987). Beam loading efficiency in plasma accelerators. *Particle Accelerators*, 22:81–99.
- [Keldysh et al., 1965] Keldysh, L. et al. (1965). Ionization in the field of a strong electromagnetic wave. *Soviet Physics - Journal of Experimental and Theoretical Physics*, 20(5):1307–1314.
- [Kenney and Keeping, 1965] Kenney, J. F. and Keeping, E. S. (1965). *Mathematics of statistics*. JSTOR.
- [Khan et al., 2006] Khan, S., Holldack, K., Kachel, T., Mitzner, R., and Quast, T. (2006). Femtosecond undulator radiation from sliced electron bunches. *Physical Review Letters*, 97(7):074801.
- [Kiselev et al., 2004] Kiselev, S., Pukhov, A., and Kostyukov, I. (2004). X-ray generation in strongly nonlinear plasma waves. *Physical Review Letters*, 93:135004.
- [Kneip et al., 2012] Kneip, S., McGuffey, C., Martins, J., Bloom, M., Chvykov, V., Dollar, F., Fonseca, R., Jolly, S., Kalintchenko, G., Krushelnick, K., et al. (2012). Characterization of transverse beam emittance of electrons from a laser-plasma wake-field accelerator in the bubble regime using betatron x-ray radiation. *Physical Review Special Topics-Accelerators and Beams*, 15(2):021302.
- [Kneip et al., 2008] Kneip, S., Nagel, S., Bellei, C., Bourgeois, N., Dangor, A., Gopal, A., Heathcote, R., Mangles, S., Marques, J., Maksimchuk, A., et al. (2008). Observation of synchrotron radiation from electrons accelerated in a petawatt-laser-generated plasma cavity. *Physical Review Letters*, 100(10):105006.

- [Kostyukov et al., 2009] Kostyukov, I., Nerush, E., Pukhov, A., and Sereedov, V. (2009). Electron self-injection in multidimensional relativistic-plasma wake fields. *Physical Review Letters*, 103(17):175003.
- [Kostyukov et al., 2004] Kostyukov, I., Pukhov, A., and Kiselev, S. (2004). Phenomenological theory of laser-plasma interaction in “bubble” regime. *Physics of Plasmas*, 11(11):5256–5264.
- [Kotaki et al., 2004] Kotaki, H., Masuda, S., Kando, M., Koga, J., and Nakajima, K. (2004). Head-on injection of a high quality electron beam by the interaction of two laser pulses. *Physics of Plasmas*, 11(6):3296–3302.
- [Krause et al., 1992] Krause, J. L., Schafer, K. J., and Kulander, K. C. (1992). High-order harmonic generation from atoms and ions in the high intensity regime. *Physical Review Letters*, 68(24):3535.
- [Kruer, 1988] Kruer, W. L. (1988). *The physics of laser plasma interactions*. Addison-Wesley Pub. Co. Inc., Reading, MA.
- [Landau and Lifshitz, 1951] Landau, L. and Lifshitz, E. (1951). *The Classical Theory of Fields*. Addison-Wesley physics. Addison-Wesley Press.
- [Lawson et al., 1979] Lawson, J. et al. (1979). Lasers and accelerators. *IEEE Transactions on Nuclear Science*, 26(3):4217–4219.
- [Lee et al., 2003] Lee, K., Cha, Y., Shin, M., Kim, B., and Kim, D. (2003). Relativistic nonlinear Thomson scattering as attosecond x-ray source. *Physical Review E*, 67(2):026502.
- [Leemans et al., 2014] Leemans, W., Gonsalves, A., Mao, H.-S., Nakamura, K., Benedetti, C., Schroeder, C., Tóth, C., Daniels, J., Mittelberger, D., Bulanov, S., et al. (2014). Multi-GeV electron beams from capillary-discharge-guided subpetawatt laser pulses in the self-trapping regime. *Physical Review Letters*, 113(24):245002.
- [Leemans et al., 2006] Leemans, W. P., Nagler, B., Gonsalves, A. J., Tóth, C., Nakamura, K., Geddes, C. G., Esarey, E., Schroeder, C., and Hooker, S. (2006). GeV electron beams from a centimetre-scale accelerator. *Nature Physics*, 2(10):696.
- [Lehe, 2014] Lehe, R. (2014). *Improvement of laser-wakefield accelerators: towards a compact free electron laser*. Theses, Ecole Polytechnique.

- [Lehe et al., 2013] Lehe, R., Lifschitz, A., Davoine, X., Thaury, C., and Malka, V. (2013). Optical transverse injection in laser-plasma acceleration. *Physical Review Letters*, 111(8):085005.
- [Levitin, 2004] Levitin, V. (2004). *Atom Vibrations in Solids: Amplitudes and Frequencies*. Cambridge Scientific Publishers.
- [Li et al., 2013] Li, F., Sheng, Z.-M., Liu, Y., Meyer-ter Vehn, J., Mori, W., Lu, W., and Zhang, J. (2013). Dense attosecond electron sheets from laser wakefields using an up-ramp density transition. *Physical Review Letters*, 110(13):135002.
- [Li et al., 2016] Li, X., Yu, Q., Gu, Y., Qu, J., Ma, Y., Kong, Q., and Kawata, S. (2016). Calculating the radiation characteristics of accelerated electrons in laser-plasma interactions. *Physics of Plasmas*, 23(3):033113.
- [Lu et al., 2006] Lu, W., Huang, C., Zhou, M., Tzoufras, M., Tsung, F., Mori, W., and Katsouleas, T. (2006). A nonlinear theory for multidimensional relativistic plasma wave wakefields. *Physics of Plasmas*, 13(5):056709.
- [Lu et al., 2007] Lu, W., Tzoufras, M., Joshi, C., Tsung, F., Mori, W., Vieira, J., Fonseca, R., and Silva, L. (2007). Generating multi-GeV electron bunches using single stage laser wakefield acceleration in a 3D nonlinear regime. *Physical Review Special Topics-Accelerators and Beams*, 10(6):061301.
- [Lundh et al., 2011] Lundh, O., Lim, J., Rechatin, C., Ammoura, L., Ben-Ismaïl, A., Davoine, X., Gallot, G., Goddet, J.-P., Lefebvre, E., Malka, V., et al. (2011). Few femtosecond, few kiloampere electron bunch produced by a laser-plasma accelerator. *Nature Physics*, 7(3):219.
- [Macchi, 2013] Macchi, A. (2013). *A Superintense Laser-Plasma Interaction Theory Primer*. Springer Science & Business Media.
- [Maine et al., 1988] Maine, P., Strickland, D., Bado, P., Pessot, M., and Mourou, G. (1988). Generation of ultrahigh peak power pulses by chirped pulse amplification. *IEEE Journal of Quantum Electronics*, 24(2):398–403.
- [Mangles et al., 2009] Mangles, S., Genoud, G., Kneip, S., Burza, M., Cassou, K., Cros, B., Dover, N., Kamperidis, C., von Uboot, E., Najmudin, Z., Persson, A., et al. (2009). Controlling the spectrum of X-rays generated in a laser-plasma accelerator by tailoring the laser wavefront. *Applied Physics Letters*, 95(18):181106.

- [Mangles et al., 2012] Mangles, S. P., Genoud, G., Bloom, M. S., Burza, M., Najmudin, Z., Persson, A., Svensson, K., Thomas, A. G. R., and Wahlström, C.-G. (2012). Self-injection threshold in self-guided laser wakefield accelerators. *Physical Review Special Topics-Accelerators and Beams*, 15(1):011302.
- [Mangles et al., 2004] Mangles, S. P., Murphy, C., Najmudin, Z., Thomas, A. G. R., Collier, J., Dangor, A. E., Divall, E., Foster, P., Gallacher, J., Hooker, C., et al. (2004). Monoenergetic beams of relativistic electrons from intense laser–plasma interactions. *Nature*, 431(7008):535.
- [Massimo et al., 2018] Massimo, F., Lifschitz, A., Thaury, C., and Malka, V. (2018). Numerical study of laser energy effects on density transition injection in laser wakefield acceleration. *Plasma Physics and Controlled Fusion*, 60(3):034005.
- [McGuffey et al., 2010] McGuffey, C., Thomas, A., Schumaker, W., Matsuoka, T., Chvykov, V., Dollar, F., Kalintchenko, G., Yanovsky, V., Maksimchuk, A., Krushelnick, K., et al. (2010). Ionization induced trapping in a laser wakefield accelerator. *Physical Review Letters*, 104(2):025004.
- [Mendonca, 1983] Mendonca, J. (1983). Threshold for electron heating by two electromagnetic waves. *Physical Review A*, 28(6):3592.
- [Mewe, 1999] Mewe, R. (1999). Atomic physics of hot plasmas. In *X-ray Spectroscopy in Astrophysics*, pages 109–187. Springer.
- [Milburn, 1963] Milburn, R. H. (1963). Electron scattering by an intense polarized photon field. *Physical Review Letters*, 10(3):75.
- [Miller, 2014] Miller, R. D. (2014). Femtosecond crystallography with ultrabright electrons and X-rays: capturing chemistry in action. *Science*, 343(6175):1108–1116.
- [Mourou, 1997] Mourou, G. (1997). The ultrahigh-peak-power laser: present and future. *Applied Physics B: Lasers and Optics*, 65(2):205–211.
- [Mourou et al., 2006] Mourou, G. A., Tajima, T., and Bulanov, S. V. (2006). Optics in the relativistic regime. *Reviews of Modern Physics*, 78(2):309.
- [Mulser and Bauer, 2010] Mulser, P. and Bauer, D. (2010). *High power laser-matter interaction*, volume 238. Springer Science & Business Media.
- [Nakamura et al., 2004] Nakamura, K., Fubiani, G., Geddes, C., Michel, P., van Tilborg, J., Tóth, C., Esarey, E., Schroeder, C., and Leemans, W. (2004). Laser triggered

- injection of electrons in a laser wakefield accelerator with the colliding pulse method. In *AIP Conference Proceedings*, volume 737(1), pages 901–906. AIP.
- [NIST, 2018] NIST (2018). National institute of Standards and Technology. Atomic Spectra Database Ionization Energies Form. Accessed on 13th March 2018, <https://physics.nist.gov/PhysRefData/ASD/ionEnergy.html>.
- [Oz et al., 2007] Oz, E., Deng, S., Katsouleas, T., Muggli, P., Barnes, C., Blumenfeld, I., Decker, F., Emma, P., Hogan, M., Ischebeck, R., et al. (2007). Ionization-induced electron trapping in ultrarelativistic plasma wakes. *Physical Review Letters*, 98(8):084801.
- [Pak et al., 2010] Pak, A., Marsh, K., Martins, S., Lu, W., Mori, W., and Joshi, C. (2010). Injection and trapping of tunnel-ionized electrons into laser-produced wakes. *Physical Review Letters*, 104(2):025003.
- [Patin et al., 2005] Patin, D., Bourdier, A., and Lefebvre, E. (2005). Stochastic heating in ultra high intensity laser-plasma interaction. *Laser and Particle Beams*, 23(3):297–302.
- [Paul et al., 2001] Paul, P., Toma, E., Breger, P., Mullot, G., Augé, F., Balcou, P., Muller, H., and Agostini, P. (2001). Observation of a train of attosecond pulses from high harmonic generation. *Science*, 292(5522):1689–1692.
- [Petrillo et al., 2008] Petrillo, V., Serafini, L., and Tomassini, P. (2008). Ultrahigh brightness electron beams by plasma-based injectors for driving all-optical free-electron lasers. *Physical Review Special Topics-Accelerators and Beams*, 11(7):070703.
- [Plateau et al., 2012] Plateau, G., Geddes, C., Thorn, D., Chen, M., Benedetti, C., Esarey, E., Gonsalves, A., Matlis, N., Nakamura, K., Schroeder, C., et al. (2012). Low-emittance electron bunches from a laser-plasma accelerator measured using single-shot x-ray spectroscopy. *Physical Review Letters*, 109(6):064802.
- [Pukhov and Meyer-ter Vehn, 2002] Pukhov, A. and Meyer-ter Vehn, J. (2002). Laser wake field acceleration: the highly non-linear broken-wave regime. *Applied Physics B*, 74(4-5):355–361.
- [Raizer, 1977] Raizer, Y. P. (1977). *Laser-induced discharge phenomena*. Consultants Bureau/Plenum Publishing.
- [Rechatin et al., 2009a] Rechatin, C., Davoine, X., Lifschitz, A., Ismail, A. B., Lim, J., Lefebvre, E., Faure, J., and Malka, V. (2009a). Observation of beam loading in a laser-plasma accelerator. *Physical Review Letters*, 103(19):194804.

- [Rechatin et al., 2009b] Rechatin, C., Faure, J., Ben-Ismaïl, A., Lim, J., Fitour, R., Specka, A., Videau, H., Tafzi, A., Burgy, F., and Malka, V. (2009b). Controlling the phase-space volume of injected electrons in a laser-plasma accelerator. *Physical Review Letters*, 102(16):164801.
- [Rechatin et al., 2009c] Rechatin, C., Faure, J., Lifschitz, A., Davoine, X., Lefebvre, E., and Malka, V. (2009c). Quasi-monoenergetic electron beams produced by colliding cross-polarized laser pulses in underdense plasmas. *New Journal of Physics*, 11(1):013011.
- [Ross et al., 1997] Ross, I., Matousek, P., Towrie, M., Langley, A., and Collier, J. (1997). The prospects for ultrashort pulse duration and ultrahigh intensity using optical parametric chirped pulse amplifiers. *Optics Communications*, 144(1-3):125–133.
- [Rousse et al., 2001] Rousse, A., Rischel, C., and Gauthier, J.-C. (2001). Femtosecond X-ray crystallography. *Reviews of Modern Physics*, 73(1):17.
- [Rousse et al., 2004] Rousse, A., Ta Phuoc, K., Shah, R., Pukhov, A., Lefebvre, E., Malka, V., Kiselev, S., Burgy, F., Rousseau, J.-P., Umstadter, D., et al. (2004). Production of a keV X-ray beam from synchrotron radiation in relativistic laser-plasma interaction. *Physical Review Letters*, 93(13):135005.
- [Sarri et al., 2014] Sarri, G., Corvan, D., Schumaker, W., Cole, J., Di Piazza, A., Ahmed, H., Harvey, C., Keitel, C. H., Krushelnick, K., Mangles, S., et al. (2014). Ultrahigh brilliance multi-MeV γ -ray beams from nonlinear relativistic Thomson scattering. *Physical Review Letters*, 113(22):224801.
- [Schick et al., 2016] Schick, D., Le Guyader, L., Pontius, N., Radu, I., Kachel, T., Mitzner, R., Zeschke, T., Schüßler-Langeheine, C., Föhlich, A., and Holldack, K. (2016). Analysis of the halo background in femtosecond slicing experiments. *Journal of Synchrotron Radiation*, 23(3).
- [Schmid et al., 2010] Schmid, K., Buck, A., Sears, C. M., Mikhailova, J. M., Tautz, R., Herrmann, D., Geissler, M., Krausz, F., and Veisz, L. (2010). Density-transition based electron injector for laser driven wakefield accelerators. *Physical Review Special Topics-Accelerators and Beams*, 13(9):091301.
- [Schoenlein et al., 2000] Schoenlein, R., Chattopadhyay, S., Chong, H., Glover, T., Heimann, P., Shank, C., Zholents, A., and Zolotarev, M. (2000). Generation of femtosecond pulses of synchrotron radiation. *Science*, 287(5461):2237–2240.

- [Schultz and Vrakking, 2013] Schultz, T. and Vrakking, M. (2013). *Attosecond and XUV Spectroscopy: Ultrafast Dynamics and Spectroscopy*. John Wiley & Sons.
- [Semendyayev and Mühlig, 1997] Semendyayev, I. B. K. and Mühlig, G. M. H. (1997). *Handbook of Mathematics*. Springer.
- [Shaw et al., 2016] Shaw, J., Lemos, N., Marsh, K., Tsung, F., Mori, W., and Joshi, C. (2016). Estimation of direct laser acceleration in laser wakefield accelerators using particle-in-cell simulations. *Plasma Physics and Controlled Fusion*, 58(3):034008.
- [Sheng et al., 2002] Sheng, Z.-M., Mima, K., Sentoku, Y., Jovanović, M., Taguchi, T., Zhang, J., and Meyer-ter Vehn, J. (2002). Stochastic heating and acceleration of electrons in colliding laser fields in plasma. *Physical Review Letters*, 88(5):055004.
- [Siegman, 1986] Siegman, A. E. (1986). Lasers university science books. *Mill Valley, CA*, 37:462–466.
- [Smith, 2007] Smith, J. O. (2007). *Mathematics of the discrete Fourier transform (DFT): with audio applicaitons*. W3K Publishing.
- [Sprangle et al., 1988] Sprangle, P., Joyce, G., Esarey, E., and Ting, A. (1988). Laser wakefield acceleration and relativistic optical guiding. In *AIP Conference Proceedings*, volume 175(1), pages 231–239. AIP.
- [Steiniger et al., 2016] Steiniger, K., Debus, A., Irman, A., Jochmann, A., Pausch, R., Schramm, U., and Bussmann, M. (2016). Brilliant and efficient optical free-electron lasers with traveling-wave Thomson-Scattering. In *AIP Conference Proceedings*, volume 1777(1), page 080016. AIP Publishing.
- [Suk et al., 2001] Suk, H., Barov, N., Rosenzweig, J. B., and Esarey, E. (2001). Plasma electron trapping and acceleration in a plasma wake field using a density transition. *Physical Review Letters*, 86:1011–1014.
- [Sun et al., 1987] Sun, G.-Z., Ott, E., Lee, Y., and Guzdar, P. (1987). Self-focusing of short intense pulses in plasmas. *Physics of Fluids*, 30(2):526–532.
- [Swanson et al., 2017] Swanson, K., Tsai, H.-E., Barber, S., Lehe, R., Mao, H.-S., Steinke, S., van Tilborg, J., Nakamura, K., Geddes, C., Schroeder, C., et al. (2017). Control of tunable, monoenergetic laser-plasma-accelerated electron beams using a shock-induced density downramp injector. *Physical Review Accelerators and Beams*, 20(5):051301.

- [Ta Phuoc et al., 2005] Ta Phuoc, K., Burgy, F., Rousseau, J.-P., and Rousse, A. (2005). Nonlinear Thomson scattering from relativistic laser plasma interaction. *The European Physical Journal D – Atomic, Molecular, Optical and Plasma Physics*, 33(2):301–306.
- [Ta Phuoc et al., 2006] Ta Phuoc, K., Corde, S., Shah, R., Albert, F., Fitour, R., Rousseau, J.-P., Burgy, F., Mercier, B., and Rousse, A. (2006). Imaging electron trajectories in a laser-wakefield cavity using betatron X-ray radiation. *Physical Review Letters*, 97(22):225002.
- [Ta Phuoc et al., 2012] Ta Phuoc, K., Corde, S., Thaury, C., Malka, V., Tafzi, A., Goddet, J., Shah, R., Sebban, S., and Rousse, A. (2012). All-optical Compton gamma-ray source. *Nature Photonics*, 6(5):308–311.
- [Tajima and Dawson, 1979] Tajima, T. and Dawson, J. (1979). Laser electron accelerator. *Physical Review Letters*, 43(4):267.
- [Thomas, 2010a] Thomas, A. (2010a). Algorithm for calculating spectral intensity due to charged particles in arbitrary motion. *Physical Review Special Topics-Accelerators and Beams*, 13(2):020702.
- [Thomas et al., 2008] Thomas, A., Murphy, C., Mangles, S., Dangor, A., Foster, P., Gallacher, J., Jaroszynski, D., Kamperidis, C., Lancaster, K., Norreys, P., et al. (2008). Monoenergetic electronic beam production using dual collinear laser pulses. *Physical Review Letters*, 100(25):255002.
- [Thomas, 2010b] Thomas, A. G. R. (2010b). Scalings for radiation from plasma bubbles. *Physics of Plasmas*, 17(5):056708.
- [Thomas, 2011] Thomas, A. G. R. (2011). Response to “Comment on ‘Scalings for radiation from plasma bubbles’”[Phys. Plasmas 18, 034701 (2011)]. *Physics of Plasmas*, 18(3):034702.
- [Tooley et al., 2017] Tooley, M., Ersfeld, B., Yoffe, S., Noble, A., Brunetti, E., Sheng, Z., Islam, M., and Jaroszynski, D. (2017). Towards attosecond high-energy electron bunches: Controlling self-injection in laser-wakefield accelerators through plasma-density modulation. *Physical Review Letters*, 119(4):044801.
- [Tschemtscher and Feidenhans'l, 2017] Tschemtscher, T. and Feidenhans'l, R. (2017). Starting User Operation at the European XFEL. *Synchrotron Radiation News*, 30(6):21–28.

- [Umstadter, 2003] Umstadter, D. (2003). Relativistic laser–plasma interactions. *Journal of Physics D: Applied Physics*, 36(8):R151.
- [Umstadter et al., 1994] Umstadter, D., Esarey, E., and Kim, J. (1994). Nonlinear plasma waves resonantly driven by optimized laser pulse trains. *Physical Review Letters*, 72(8):1224.
- [Umstadter et al., 1996] Umstadter, D., Kim, J., and Dodd, E. (1996). Laser injection of ultrashort electron pulses into wakefield plasma waves. *Physical Review Letters*, 76(12):2073.
- [Wang and Sheng, 2008] Wang, W.-M. and Sheng, Z.-M. (2008). Effect of laser parameters on electron injection into laser wakefields in plasma with a counterpropagating additional laser pulse. *Physics of Plasmas*, 15(1):013101.
- [Wang et al., 2008] Wang, W.-M., Sheng, Z.-M., and Zhang, J. (2008). Controlled electron injection into laser wakefields with a perpendicular injection laser pulse. *Applied Physics Letters*, 93(20):201502.
- [Wang et al., 2015] Wang, X., Du, D., Yi, S., Kalmykov, S., D’avignon, E., Fazel, N., Zagdzaj, R., Reed, S., Dong, P., Henderson, W., et al. (2015). Multi-GeV Electron Generation Using Texas Petawatt Laser. *AIP Conference Proceedings*.
- [Wang et al., 1997] Wang, Z., Zhang, Z., Xu, Z., and Lin, Q. (1997). Space-time profiles of an ultrashort pulsed Gaussian beam. *IEEE Journal of Quantum Electronics*, 33(4):566–573.
- [Wenz et al., 2015] Wenz, J., Schleede, S., Khrennikov, K., Bech, M., Thibault, P., Heigoldt, M., Pfeiffer, F., and Karsch, S. (2015). Quantitative x-ray phase-contrast microtomography from a compact laser-driven betatron source. *Nature Communications*, 6:7568.
- [Whittum et al., 1990] Whittum, D. H., Sessler, A. M., and Dawson, J. M. (1990). Ion-channel laser. *Physical Review Letters*, 64(21):2511.
- [Witte and Eikema, 2012] Witte, S. and Eikema, K. S. (2012). Ultrafast optical parametric chirped-pulse amplification. *IEEE Journal of Selected Topics in Quantum Electronics*, 18(1):296–307.
- [Xu et al., 2014] Xu, X., Wu, Y., Zhang, C., Li, F., Wan, Y., Hua, J., Pai, C.-H., Lu, W., Yu, P., Joshi, C., et al. (2014). Low emittance electron beam generation from a

- laser wakefield accelerator using two laser pulses with different wavelengths. *Physical Review Special Topics-Accelerators and Beams*, 17(6):061301.
- [Yamanouchi et al., 2015] Yamanouchi, K., Cundiff, S., de Vivie-Riedle, R., Kuwata-Gonokami, M., and Di Mauro, L. (2015). *Ultrafast Phenomena XIX: Proceedings of the 19th International Conference, Okinawa Convention Center, Okinawa, Japan, July 7-11, 2014*, volume 162. Springer.
- [Yu et al., 2014] Yu, L.-L., Esarey, E., Schroeder, C., Vay, J.-L., Benedetti, C., Geddes, C., Chen, M., and Leemans, W. (2014). Two-color laser-ionization injection. *Physical Review Letters*, 112(12):125001.
- [Zewail, 2000] Zewail, A. H. (2000). Femtochemistry: Atomic-scale dynamics of the chemical bond using ultrafast lasers (Nobel Lecture). *Angewandte Chemie International Edition*, 39(15):2586–2631.
- [Zhang et al., 2003a] Zhang, P., Saleh, N., Chen, S., Sheng, Z., and Umstadter, D. (2003a). Laser-energy transfer and enhancement of plasma waves and electron beams by interfering high-intensity laser pulses. *Physical Review Letters*, 91(22):225001.
- [Zhang et al., 2003b] Zhang, P., Saleh, N., Chen, S., Sheng, Z., and Umstadter, D. (2003b). An optical trap for relativistic plasma. *Physics of Plasmas*, 10(5):2093–2099.

List of author's publications

Publications in impacted journals and author's contribution

1. **Vojtěch Horný**, Dominika Mašlárová, Václav Petržílka, Ondřej Klimo, Michaela Kozlová, and Miroslav Krůs. Optical injection dynamics in two laser wakefield acceleration configurations. *Plasma Physics and Controlled Fusion*, 60.6 (2018): 064009.
 - author's contribution: particle-in-cell simulations, processing and interpretation of results.
2. **Vojtěch Horný**, Václav Petržílka, Ondřej Klimo, and Miroslav Krůs. Short electron bunches generated by perpendicularly crossing laser pulses. *Physics of Plasmas*, 24(10):103125, 2017.
 - author's contribution: partially design of the concept, particle-in-cell and single particle simulations, processing and interpretation of results.
3. **Vojtěch Horný**, Jaroslav Nejd, Michaela Kozlová, Miroslav Krůs, Karel Boháček, Václav Petržílka, and Ondřej Klimo. Temporal profile of betatron radiation from laser-driven electron accelerators. *Physics of Plasmas*, 24(6):063107, 2017.
 - author's contribution: design, mathematical justification, implementation and demonstration of method, particle-in-cell simulations, processing and interpretation of results.
4. **Vojtěch Horný** and Ondřej Klimo. Hot electron refluxing in the short intense laser pulse interactions with solid targets and its influence on K- α radiation. *Nukleonika*, 60(2):233–237, 2015.
 - author's contribution: particle-in-cell simulations, processing of results.

5. **Vojtěch Horný**, Ondřej Klimo, and Miroslav Krůs. High charge plasma electron bunches from two collinear laser pulses. Submitted to *Applied Physics Letters*, 2018.
 - author's contribution: partially design of the concept, particle-in-cell simulations, processing and interpretation of results.
6. Karel Boháček, Michaela Kozlová, Jaroslav Nejd, Uddhab Chaulagain, **Vojtěch Horný**, Miroslav Krůs, and Kim Ta Phuoc. Stable electron beams from laser wakefield acceleration with few-terawatt driver using a supersonic air jet. *Nuclear Instruments and Methods in Physics Research Section A: Accelerators, Spectrometers, Detectors and Associated Equipment*, 883:24–28, 2018.
 - author's contribution: particle-in-cell simulations.

Publications in conference proceedings

1. **Vojtěch Horný** and Miroslav Krůs. Optical injection into the laser wakefield accelerator by co-propagating weaker pulse. In *Proceedings of the 44th EPS Conference on Plasma Physics*, 2017.
2. **Vojtěch Horný**, Václav Petržílka, Ondřej Klimo, and Miroslav Krůs. Short energetic electron bunches from laser wakefield accelerator with orthogonally polarized perpendicularly crossed laser pulses. In *Laser Acceleration of Electrons, Protons, and Ions IV*, volume 10240, page 1024011. International Society for Optics and Photonics, 2017.
3. **Vojtěch Horný**, Václav Petržílka, Miroslav Krůs, and Ondřej Klimo. Electron acceleration in perpendicularly crossed laser beams with following injection in the laser wakefield accelerator. In *EPS 2016: 43rd European Physical Society Conference on Plasma Physics*, volume 40, page 078, 2016.
4. Uddhab Chaulagain, Karel Boháček, Michaela Kozlová, Jaroslav Nejd, Miroslav Krůs, **Vojtěch Horný**, Benoit Mahieu, and Kim Ta Phuoc. X-ray phase contrast imaging of biological samples using a betatron X-ray source generated in a laser wakefield accelerator. In *Laser Acceleration of Electrons, Protons, and Ions IV*, volume 10240, page 1024014. International Society for Optics and Photonics, 2017.
5. Karel Boháček, Michaela Kozlová, Jaroslav Nejd, Uddhab Chaulagain, **Vojtěch Horný**, Miroslav Krůs, and Martin Albrecht. Generation of laser-driven femtosecond

